University of Turin
Department of Molecular Biotechnology and Health Sciences

Ph.D. Program in Biomedical Sciences and Oncology

XXXVI Cycle

Exploiting metabolic and molecular alterations as therapeutic targets for skeletal muscle atrophy in inflammatory diseases.

Tutor:

Prof. Paolo Porporato

Candidate:

Erica Mina

Coordinator:

Prof. Emilio Hirsch

Academic Years: 2020-2024

05/BIOS-10

'Tain't What You Do
It's the Way That You Do It
That's What Gets Results

Ella Fitzgerald

Index

Abstract

Skeletal muscle atrophy is one of the main features of cachexia, a complex multi-organ disease associated with cancer, sepsis, and other chronic conditions marked by systemic inflammation. Despite its high prevalence and significant impact on patients' quality of life and therapeutic outcomes, cachexia remains an unmet medical need, as its underlying mechanisms are not fully understood.

This study focuses on uncovering novel mechanisms driving skeletal muscle atrophy to identify novel potential therapeutic targets.

Starting during the SARS-CoV-2 pandemic, our research initially centered on patients in Intensive Care Units (ICUs) undergoing invasive mechanical ventilation (IMV). These patients, especially those suffering from systemic inflammation due to COVID-19, sepsis, or pneumonia, were found to be at high risk for severe skeletal muscle atrophy. We found that their plasma induced skeletal muscle wasting, oxidative stress, and mitochondrial dysfunction *in vitro*, highlighting the central role of inflammatory cytokines in muscle catabolism. Notably, extracellular vesicles (EVs) reversed muscle atrophy and mitigate oxidative stress, suggesting their potential as therapeutic agents for sepsis-induced muscle wasting.

We then investigated the mechanisms behind mitochondrial dysfunction in cancer-induced skeletal muscle atrophy. Our findings revealed that alterations in systemic iron metabolism led to abnormal iron compartmentalization within atrophic muscle fibers, further exacerbating mitochondrial dysfunction. Iron supplementation not only preserved muscle function and prolonged survival in cachectic mice, but also restored muscle strength in anemic cancer patients. These results emphasize the critical role of iron homeostasis in maintaining muscle mass and function, suggesting that targeting iron metabolism could offer a therapeutic strategy for cancer cachexia.

Subsequently, intrigued by the upregulation of the iron-regulating hormone erythroferrone (ERFE) in cachexia, known to inhibit BMP signaling in the liver, we identified and characterized two novel BMP inhibitors involved in skeletal muscle atrophy: the BMP scavenger ERFE and the intracellular inhibitor FKBP12.

To overcome the BMP resistance mediated by these inhibitors, we administered low-dose tacrolimus (FK506) to target FKBP12. FK506 effectively restored BMP signaling, preventing skeletal muscle wasting *in vitro* and *in vivo* while also protecting against neuromuscular junction disruption and force loss. We therefore proposed that low-dose FK506 may represent a promising therapeutic approach for restoring BMP signaling in atrophic skeletal muscles, thereby offering a potential treatment for cancer cachexia.

Introduction

1. The homeostasis and plasticity of the skeletal muscle

Skeletal muscle accounts for the 40-50% of the total mass in healthy individuals and it represents the protein storage of our body. Due to the high plasticity of this tissue, skeletal muscle not only is responsible for locomotion and posture, but it is fundamental for breathing, eating and energy expenditure. Skeletal muscle is indeed relevant for maintaining systemic metabolism, being a regulator of glucose, aminoacids and lipid homeostasis.

Certain pathological conditions might alter skeletal muscle metabolism and signaling, resulting in wasting and impairment of muscle function, with a relevant reduction of patients' life quality. Since skeletal muscle fibers have a dense cytoplasm filled with contractile proteins and organelles, alterations in their turnover impact extensively fibers size and function.

Skeletal muscle mass is influenced by various stimuli, such as hypertrophy induced by physical exercise and anabolic hormones, or atrophy induced by fasting, cancer or sepsis. The size of skeletal muscle fibers is defined by the balance between protein synthesis and protein degradation and several interactors and molecular pathway influence the signaling and the metabolism of these cells, influencing their trophism.

1.1 Metabolic adaptations and skeletal muscle mass regulation

Being far more than just a compartment for movement and posture, skeletal muscle plays a pivotal role in regulating our body metabolism, serving as an essential site for glucose uptake and storage in the form of glycogen. This function is essential for maintaining glucose homeostasis and providing energy to the body. (1) Additionally, skeletal muscle is a substantial reservoir of amino acids that can be used for energy production when other sources are scarce. (2)

In physiological condition and at rest, the skeletal muscle and cardiac muscle account for about 30% of the body's energy consumption; while during exercise, this percentage can rise to 100%. (3)
Different skeletal muscles are composed by different types of fibers that are categorized based on their metabolic characteristics: slow-twitch fibers (type I), are oxidative and primarily rely on aerobic metabolism; fast-twitch fibers (type II) are glycolytic and anaerobic. The former allow prolonged physical activity and resistance to fatigue; while the latter enable rapid ATP production and contractions, consuming quicky the energy reserve, due to the lower efficiency of glycolysis compared to oxidative phosphorylation. (4)

Being an essential regulator of metabolism and considering the it accounts for 40-50% of whole-body weight, skeletal muscle physiology and mass can be altered by systemic metabolic diseases and itself, can act as a *disease modifier*.
In systemic metabolic diseases, such as metabolic syndrome and type II diabetes, when the nutrient absorption is impaired, the skeletal muscle plays a pivotal role to balance the energy needs of other organs and to provide amino acids for energy production. (5) Its glycogen stores are crucial for rapid energy production during muscle contractions, but during starvation or extreme energy deficits, the skeletal muscle breaks down its proteins into amino acids providing substrates for gluconeogenesis, as it accounts for the 75% of the body's total protein (2).

An example of how systemic metabolic alterations can affect muscles is given by insulin resistance, where an increase in fast-twitch fibers and muscle atrophy is observed (6). The metabolic capacity of fast-twitch fibers and muscle mass are enhanced with resistance training. (7) Conversely, resistance training improves insulin sensitivity in diabetic patients, indicating that changes within the skeletal muscle can impact on systemic metabolism and *vice versa*. (8)

Several factors, including nutrients, hormones, mechanical stretch, and calcium levels, induce one of the major metabolic regulators in the skeletal muscle: the myocyte enhancer factor 2 (MEF2). MEF2 stimulates the transcriptional activity of

peroxisome proliferator-activated receptor (PPAR) and peroxisome proliferator-activated receptor gamma coactivator 1-alpha (PGC1α), two critical regulators of muscle metabolism, thus inducting mitochondrial biogenesis and enhanced fatty acid oxidation (8).

For instance, PPARα activation promotes fatty acid utilization in human muscle cells (9); however, its overexpression in transgenic mice leads to insulin resistance in both skeletal muscle and the heart (10). On the same line, PPARβ/δ enhance oxidative muscle fibers formation through PGC1α activation, mimicking the effects of exercise training and promoting a lean phenotype (11). Conversely, mice with skeletal muscle-specific deletion of PPARγ develop insulin resistance and increased adiposity, further illustrating the importance of these metabolic regulators. (12)

Another master regulator of muscle metabolism that is specifically involved in mitochondrial function is PGC1α, having a splicing variant known as PGC1α4, which promotes muscle hypertrophy. While PGC1α transgenic mice do not exhibit muscle growth or enhanced protein synthesis, the PGC1α4 isoform has been found to significantly promote muscle hypertrophy, highlighting the complex regulation of muscle mass by different PGC1α isoforms. (13)

Skeletal muscles have a mitochondrial density of around 52%, and being involved in several mechanisms as ATP production, ROS formation, and apoptosis, an optimal mitochondrial function is essential for skeletal muscle health. Dysfunctional mitochondria activate catabolism in the skeletal muscle and are characteristics features of atrophy induced by cachexia, aging, disuse, or glucocorticoids. (14)

In summary, skeletal muscle is not just essential for movement but also plays a critical role in the regulation of whole-body metabolism, impacting overall health and disease states.

1.2 The signaling pathways that tune skeletal muscle mass alterations

Skeletal muscle mass physiology is determined by the flux of newly synthetized peptides, the degradation and recycling of organelles and proteasomal degradation of proteins and the major hub of these processes is the Akt-mTOR axis. (15)

Akt pathway is activated by ligands binding to G-protein-coupled receptors (GPCRs), tyrosine kinases receptors (RTKs), and insulin receptor substrate (IRS), which leads to the phosphorylation and activation of phosphoinositide 3-kinase (PI3K). The phosphorylation of membrane phosphoinositides by PI3K recruits Akt, which is fully activated following two phosphorylations from PDK1 and mTORC2 at Tyr308 and Ser473 respectively. (16) Activated Akt promotes protein synthesis through various downstream targets: it inhibits glycogen synthase kinase 3β (GSK-3β) and activates p70 and 4E-BP1 through mTOR, promoting protein translation initiation. (16) Coherently, muscle-specific constitutively active Akt induces skeletal muscle hypertrophy *in vivo* (17).

In the skeletal muscle, the Akt-mTOR hub is linked and regulated by a variety of other signaling pathways, such as the insulin/IGF1, β2-adrenergic, metallothioneins and TGFβ superfamily axes (Fig.1).

Molecules like insulin, insulin-like growth factor 1 (IGF-1), RTK ligands as some FGFs, are potent anabolic factors that by activating Akt-mTOR axis sustains organism and skeletal muscle growth. Accordingly, muscle-specific IGF1 overexpression induces muscle hypertrophy and promotes its regeneration (18).

Another pathway connected to these signaling molecules is the one of β-adrenergic receptors, that mediate skeletal muscle sympathetic activity. β2 agonists have anti-catabolic effects on the skeletal muscle, inhibiting protein degradation (19) and activating insulin/IGF1 signaling (20), as well as Akt-mTOR activation (21).

The main signaling pathway explored in this Ph.D. project, is the one of the TGFβ superfamily, a group of tens of ligands with different selectivity and specificity for different receptors. The TGFβ superfamily is involved in a wide variety of musculoskeletal processes, from embryonic development, tissue regeneration upon injury, and trophism regulation.

The signaling cascade is composed by the TGFβ-Smad2/3 branch and the BMP-Smad1/5/8 axis. The former is activated by ligands as TGFβ, activins or myostatin, that by binding type II TGFβ receptors (TGFβRII), and activin type IIB and IIA receptors (ActRIIB/ActRIIA), recruit type I serine-threonine kinase receptors ALK-4, -7, and -5, inducing Smad2/3 phosphorylation. The co-smad Smad4 is then associated to pSmad2/3 heterodimers promoting their nuclear tanslocation and transcription of atrophy-associated genes such as ubiquitin ligases. (22) Indeed, the blockade or absence of myostatin is associated to skeletal muscle hypertrophy, and this is recapitulated by Smad2/3 inhibition. (23) On the opposite axes, BMP and some GDF ligands preferentially bind Type II BMP receptors (BMPRII), ActRIIA, ActRIIB, recruiting another set of type I receptors: ALK-2, -3, -6. This receptor heterotetramerization induces Smad1/5/8 phosphorylation and Smad4 recruitment for the transcription of target genes associated to anabolism. (22) Various BMP inhibitors as Noggin, Follistatin and in this work, erythroferrone, has been shown to counteract the hypertrophic effect of BMP-signaling. (24)

The crosstalk between TGFβ superfamily and the Akt-mTOR axis has been clarified by several findings. The anabolic effects of BMP-Smad1/5/8 activation are explained by a parallel activation of the protein synthesis pathway mediated by mTOR. Moreover, mTOR knockdown or pharmacological blockade by rapamycin, reverts the hypertrophy of myostatin-KO models, explaining the convergence of this superfamily on the protein synthesis/degradation processes. (23) However, the exact interactors or molecular mechanism that mediate this crosstalk remain unknown.

As previously mentioned, skeletal muscle mass regulation is defined by the homeostasis between protein synthesis, mainly driven by Akt-mTOR axis, and protein degradation through several processes.

The most studied process is the degradation of proteins through the proteasome, facilitated by their ubiquitination by E3 ubiquitin ligases. The ones found to be upregulated in atrophic skeletal muscles were named *atrogenes*. The signaling cascades required for atrogenes expression are the activins/myostatin-TGFβ-Smad2/3, FoxOs, NF-kB, and the IL-6-JAK-Stat3 pathways.

The Forkhead box O proteins (FoxO1, FoxO3 , FoxO4, FoxO6) are transcription factors finely tuned by several post-translational modifications (activating and inhibitory phosphorylations and acetylations) and are involved in a large variety of biological processes. In the skeletal muscle, activated FoxO1 and FoxO3 transcriptionally regulate the expression of the atrogenes Atrogin-1, MuRF-1, MUSA1 (26), and this occurs in glucocorticoid-induced skeletal muscle atrophy. (27) Conversely, Akt can transfer an inhibitory phosphate on FoxOs to block ubiquitin ligase production promoting hypertrophy. (28)

Skeletal muscle mass homeostasis is often lost in diseases characterized and caused by systemic inflammation. This occurs because inflammatory pathways as TNFα-NF-kB, and IL-6-JAK-Stat3 are enhanced and causative of atrogenes overexpression.

Briefly, in response to inflammatory cytokines as TNFα, the NF-kB inhibitor IkB is degraded, thus promoting NF-kB nuclear translocation and transcription of the atrogene MuRF1. (29). TNFα, together with IL-6 and IL-1, can also activate the JAK-Stat3 pathway, that is characteristic of models of muscle atrophy induced by cancer or sepsis. Interestingly, Stat3 overexpression in the skeletal muscle induces atrophy and Atrogin-1 expression, while its inhibition prevents muscle wasting in tumor-bearing mice (30).

Overall, the intricate interconnection of numerous signaling pathways highlights the complexity of understanding skeletal muscle regulation and the challenge of developing effective pharmacological treatments for atrophy.

1.3 The cellular processes behind skeletal muscle atrophy

As mentioned previously, adult skeletal muscle mass regulation depends on organelles and protein turnover, and therefore on the balance between their

synthesis and degradation. Skeletal muscle atrophy occurs when fibers shrink due to protein, organelles and cytoplasm loss. Several diseases or conditions induce skeletal muscle atrophy, such as cachexia, sepsis, chronic kidney disease, but also disuse, denervation or aging. (31)

The major cellular catabolic mechanisms increased in atrophic muscles are the ubiquitin-proteasome system (UPS), and the autophagy-lysosome pathway (Fig.1). (32)

Proteins that are targeted for degradation by the proteasome are post-translationally modified with chains of ubiquitin by E3 ubiquitin ligases. As previously mentioned, atrophic skeletal muscles overexpress genes defined atrogenes, that degrade specific muscular proteins.

MuRF-1 and Atrogin-1 were the first ones to be discovered and while the former was shown to degrade structural proteins as myosins, actin and mitochondrial proteins (33 19506036, 22673621), the latter was found to ubiquitinate muscular signaling proteins as MyoD and the initiator of translation eIF3-f (34).

Several other ubiquitin ligases have been found to be upregulated in different types of skeletal muscle atrophy, such as Nedd4-1, during denervation and disuse (35), or TRAF6 in cancer- and starvation- induced atrophy (36).

As mentioned in Chapter 1.2, FoxO proteins have been demonstrated to induce the upregulation of various atrogenes such as MUSA1 (37), and SMART (38), but they are also involved in the cellular mechanism of autophagy. (39)

Autophagy is a homeostatic cellular mechanism essential for the degradation and recycling of organelles, cytoplasm and proteins through the lysosomal machinery (40). The activation of autophagy in the skeletal muscle occurs in several contexts, such as in cancer (41), aging (42), fasting (39), sepsis (43), denervation (44) and exercise (45). Briefly, autophagy is a process where the ULK1 complex enables cell membrane elongation to sequester cellular components in double-layered vesicles, and to deliver them to the lysosome. After their degradation, aminoacids, lipids and glucose are released. Since ULK1 is inhibited by mTORC1 (46), in atrophy, where the Akt-mTOR axis is downregulated, the increased protein degradation is also due to enhanced autophagy.

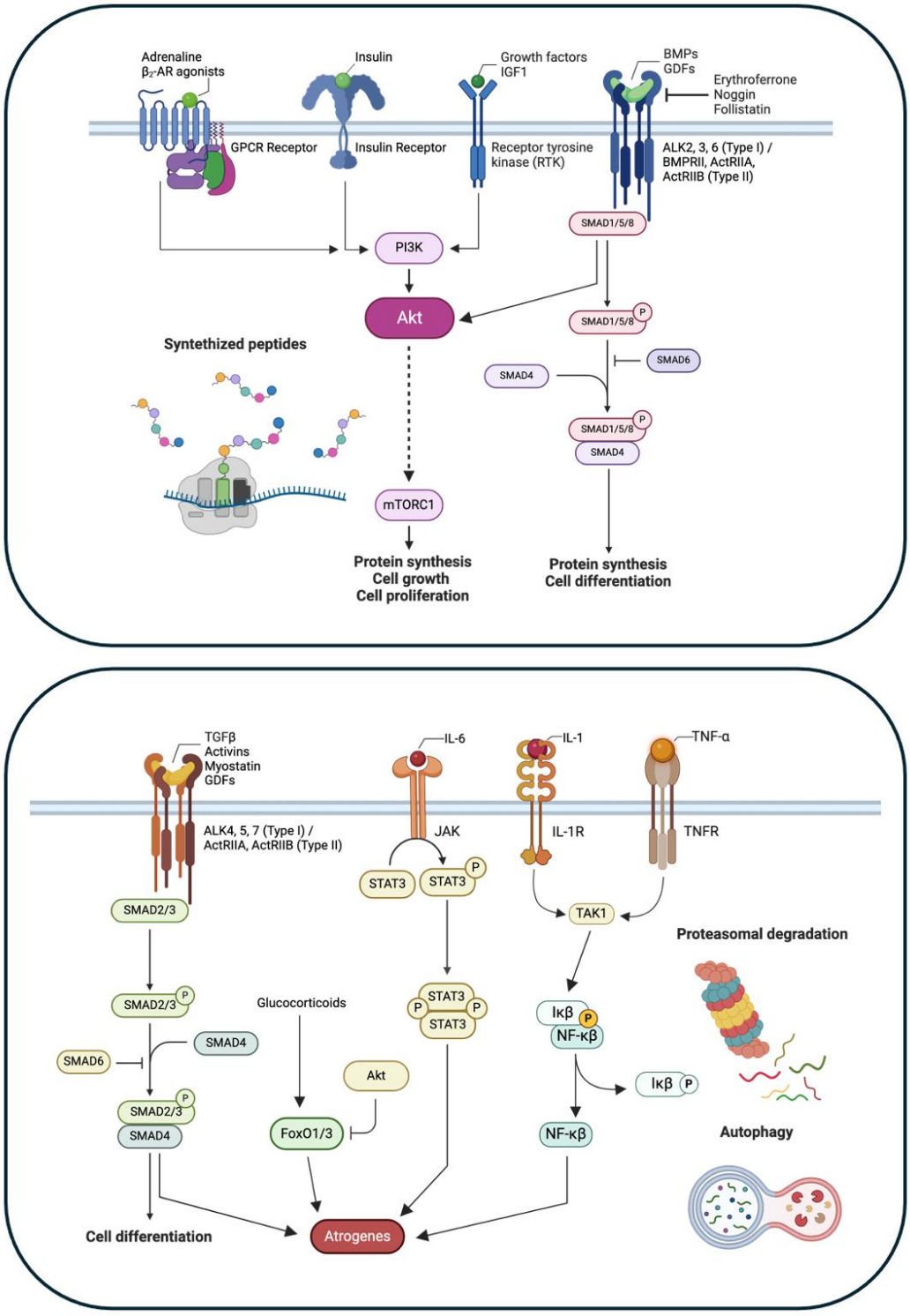

Figure 1. The signaling pathways and cellular processes that regulate skeletal muscle mass.

2. Skeletal muscle atrophy in inflammatory chronic diseases

Systemic inflammation is a pathophysiological condition that affects millions of patients worldwide and it is associated to a large variety of acute and chronic diseases, such as rheumatoid arthritis (RA), chronic obstructive pulmonary disease (COPD), sepsis, chronic kidney disease (CKD), AIDS, COVID-19 and cancer.

Systemic inflammation is the driver of *cachexia,* from the Greek "*kakos hexis*" which means "bad condition", and cachexia is defined as "a multifactorial syndrome characterized by an ongoing loss of skeletal muscle mass (with or without loss of fat mass) that cannot be fully reversed by conventional nutritional support and leads to progressive functional impairment''. (47)

Besides the most characterized cachexia is the one associated to cancer, many of its features can be applied to the non-neoplastic types of cachexia previously mentioned. In general, cachectic patients suffer from involuntary weight loss, more specifically from the skeletal muscle and fat tissue, in a context of anorexia, fatigue, malabsorption and gut dysbiosis. This loss eventually can also be expanded to tissues as bones and heart, further diminishing patients' life quality and therapies responses. (48)

Given that cachexia is a complex condition associated with various diseases, defining the clinical parameters to identify it and stage it is essential for its recognition in clinical settings.

Cachexia is defined by involuntary body weight loss of more than 5% over the past six months, or a body mass index (BMI) less than 20 kg/m^2 with any degree of weight loss greater than 2%. This weight loss is accompanied by a significant reduction in skeletal muscle mass, which is often assessed through imaging techniques such as CT or MRI scans to accurately quantify muscle volume. Additionally, cachexia is marked by elevated levels of systemic inflammation, indicated by increased concentrations of inflammatory markers such as C-reactive protein (CRP), IL-6 and TNF-α.

Pre-cachexia, on the other hand, is identified by milder symptoms with a loss of total body weight less than 5%. Early symptoms include the presence of anorexia

or reduced food intake, often coupled with mild metabolic changes. Additionally, there are mildly elevated inflammatory markers, signaling the beginning of systemic inflammation and its influence on metabolic function and muscle mass. (47) Despite the increased attention cachexia has received in recent years, the lack of its complete understanding makes it still an unmet medical need.

2.1 Cancer-induced cachexia

Patients with certain types of cancer, such as lung, colon, and pancreatic, have a high risk of developing cachexia, reaching a prevalence of 80% of all cancer types, and being the cause of death of at least 20% of cancer cases due to respiratory or cardiac failure (49).

This syndrome causes a progressive decline in functional abilities, severely impacting the quality of life by impairing movement, breathing, and swallowing food. Moreover, muscle wasting reduces the efficacy of chemotherapy, leading to lower survival rates (50).

The tumor, and the inflammation associated to it, can induce cachexia, contributing to the raise of circulating cytokines and inflammatory mediators that directly drive the wasting phenotype. These molecules upregulate many of the myokines and pathways described in Chapter 1.2, such as the TNFα-NF-kB and the IL-6-JAK-Stat3, also leading to the catabolism of other tissues. For instance, muscle-derived aminoacids boost the liver to produce acute-phase proteins such as CRP, fibrinogen, haptoglobin, ceruloplasmin, and complement components, primarily through IL-6 signaling, further contributing to inflammation (51).

The other main component undergoing wasting in cachexia is the fat tissue. White adipose tissue (WAT) undergoes lipolysis and fatty acid mobilization promoted by cytokines like IL-6, IL-1, and TNFα, leading to its wasting, with a concurrent decrease in lipogenesis and lipoprotein uptake.

Inflammatory cytokines also strongly impact the brain, causing anorexia, depression, and altered taste and smell, while the gut experiences dysbiosis,

impaired nutrient absorption, and increased ghrelin levels. Cardiac muscle atrophy is common in cancer cachexia, often leading to heart failure, correlated with increased resting energy expenditure, mitochondrial dysfunction, decreased heart weight, and impaired cardiac innervation(51).

Despite its severity, cancer cachexia remains an unmet medical need. Current treatments focus on palliative care to reduce systemic inflammation and increase food intake, or they mainly target the muscle catabolic hub of Activin receptor signaling, with questionable efficacy.

2.2 *In vivo* experimental models of cancer cachexia

Our understanding of the molecular mechanisms leading to cachexia primarily comes from experimental data obtained in rodents. However, the complexity of cachexia means that *in vivo* models often simplify the human pathophysiology. In rodents, models for cancer cachexia are generally categorized into tumor allografts and genetically engineered animals.

Tumor allograft models involve the inoculation of cancer cells or tumor tissue, usually subcutaneously, in immunocompetent mice, such as BALB/c or C57BL/6, or rats. Notable models include the Lewis lung carcinoma (LLC), the Colon-26 adenocarcinoma (C26) in mice, and the Walker-256 breast cancer model and the Yoshida liver cancer model (AH59 130) in rats.

The LLC cachexia model develops rapidly growing tumors, displaying a high variability and an anorexia nervosa only in the late stages. LLC cells frequently metastasize, aligning them more closely with human cancer development, but making the understanding of treatment responses more complex (52).
The most frequently used allograft model is the C26 tumor-bearing mice, also widely used in this study. C26 tumor-bearing mice are characterized by severe and rapid cachexia that develops within 12 days, leading to a 20% loss of lean body mass and the death of the animals (53). A slower-kinetic model lasting up to 30 days is achievable when C26 tumors are surgically implanted subcutaneously

rather than inoculating a C26 cell suspension (24). Despite differing from human kinetics, the C26 cachexia model has been extensively used to characterize numerous molecular and cellular mechanisms of cachexia.

In rats, the Walker-256 and Yoshida AH-130 models are prevalent for studying cancer cachexia in contexts of breast and liver tumors. The Walker-256 model exhibits several cachexia features, but the excessive tumor burden, which can reach 50% of body weight, presents ethical concerns (54). The Yoshida AH-130 model, created by intraperitoneal injection of Yoshida ascites from hepatocellular carcinoma AH-130 cells into male Wistar rats, induces severe anorexia and wasting within two weeks, similarly to the C26 model (55).

Genetically engineered mouse models (GEMMs) offer a potentially slower kinetic closer to human cachexia. These models are based on mutations leading to the loss of function in tumor-suppressor genes such as APC, p53, Pten or gain of function in proto-oncogenes such as KRAS. GEMMs for cachexia include APCMin/+, KPC, and KPP mice.

The APCMin/+ mouse, carrying a mutation in the Apc tumor suppressor gene, is predisposed to intestinal and colon tumors and experiences gradual body weight loss between approximately 14 and 20 weeks of age. This model exhibits several features mimicking human cancer, including a gradual increase in tumor burden, chronic inflammation, and anemia (56).

The KPC (KrasG12D/+; Trp53R172H/+; Pdx-1-Cre) mouse model develops pancreatic ductal adenocarcinoma, carrying the activating KrasG12D and the inactivating Trp53R172H of p53. KPC cells can also be used for subcutaneous or orthotopic injection in allograft models of cachexia (57). Conversely, the KPP model carries the Kras G12D mutation along with a floxed Pten, which is excised by a Cre recombinase under the control of the Ptfla promoter, active only in the adult pancreas. This induces tumors only when mice are fully adult, presenting clinical signs that more accurately reflect human cachexia compared to traditional models (58).

2.3 Skeletal muscle atrophy in acute and chronic infections

Sepsis has been defined as "*a life-threatening organ dysfunction caused by a dysregulated host response to infection*" (59). Besides advancements in medical treatments and preventive measures for bacterial and viral infections, sepsis still poses a significant threat, particularly in intensive care units (ICUs), where it remains a leading cause of mortality with a rate of 20-30%, rising to 40-50% in cases of complications such as respiratory and circulatory failure. (60)

Viral infections also play a crucial role in the development of severe systemic conditions, including sepsis. Viruses such as HIV, and more recently, SARS-CoV-2 (the virus responsible for COVID-19), can lead to sepsis in severe cases. These viral infections often worsen systemic inflammation and contribute to the high incidence of sepsis-related complications and mortality. The prolonged state of systemic inflammation caused by sepsis can have devastating effects on the skeletal muscle. Sepsis-associated muscle wasting (SAMW) is a significant complication characterized by decreased muscle mass, reduced muscle fiber size, and loss of strength. This condition is observed in approximately 40-70% of patients with sepsis and leads to prolonged physical impairment, increased morbidity, and higher mortality rates. (61)

ICUs play a critical role in managing patients with severe sepsis. However, ICUs itself can also contribute to muscle atrophy with prolonged immobilization, mechanical ventilation, and the use of sedatives and opioids.
Mechanical ventilation, essential for many sepsis patients, can lead to ventilator-induced diaphragm damage (VIDD), a form of muscle wasting specific to the diaphragm that occurs approximately in 50% of patients (62). However, both decreased and increased diaphragm thickness due to mechanical ventilation is associated to prolonged ventilation and worse clinical outcomes. Furthermore, a prolonged ICU stay is often associated with extended periods of bed rest, contributing to systemic muscle wasting and long-term physical disability. (63)

The inflammatory response in sepsis involves a complex interplay of cytokines and signaling pathways that contribute to skeletal muscle atrophy. Key cytokines implicated in this process include TNF-α, IL-6, interleukin-1 beta (IL-1β), and interferon-gamma (IFN-γ) (64). As broadly mentioned before, these cytokines activate several pathways that promote muscle protein breakdown and inhibit protein synthesis, also inducing mitochondrial dysfunction.

An example that helps to understand the prevalence and importance of sepsis is given by the global pandemic started at the end of 2019. COVID-19 is the disease caused by the coronavirus SARS-CoV-2, which affected more than 700 millions of people worldwide at the time of this work. The disease primarily affects the respiratory system, then developing significant systemic effects, including dysfunctions in the cardiovascular, neurological, and musculoskeletal systems.
The detrimental effects of COVID-19 are mostly associated to the strong inflammatory response, referred as a *cytokine storm*, which can cause extensive tissue damage beyond the lungs. Patients with severe COVID-19 often experience significant muscle wasting and weakness, a condition exacerbated by prolonged bed rest and immobilization during hospitalization. Studies have shown that within the first seven days of hospitalization, COVID-19 patients can experience a median decrease of 18.5% in the area of the rectus femoris muscle. This rapid muscle loss is attributed to the combined effects of systemic inflammation, reduced physical activity, and the catabolic state induced by the infection. (65)

Long COVID is a condition characterized by persistent symptoms that last for weeks or months after the acute phase of the infection. This syndrome affects multiple organ systems, including the musculoskeletal system, leading to chronic fatigue, muscle weakness, and reduced physical performance, affecting more than 60% of individuals with long COVID and impacting their quality of life (66).

References

1. Meyer C, Dostou JM, Welle SL, Gerich JE. Role of human liver, kidney, and skeletal muscle in postprandial glucose homeostasis. Am J Physiol Endocrinol Metab. 2002;282(2):E419-27.
2. Wolfe RR. The underappreciated role of muscle in health and disease. Am J Clin Nutr. 2006;84(3):475-82.
3. Gallagher D, Belmonte D, Deurenberg P, Wang Z, Krasnow N, Pi-Sunyer FX, et al. Organ-tissue mass measurement allows modeling of REE and metabolically active tissue mass. Am J Physiol. 1998;275(2):E249-58.
4. Schiaffino S, Reggiani C. Fiber types in mammalian skeletal muscles. Physiol Rev. 2011;91(4):1447-531.
5. Argiles JM, Campos N, Lopez-Pedrosa JM, Rueda R, Rodriguez-Manas L. Skeletal Muscle Regulates Metabolism via Interorgan Crosstalk: Roles in Health and Disease. J Am Med Dir Assoc. 2016;17(9):789-96.
6. Simoneau JA, Colberg SR, Thaete FL, Kelley DE. Skeletal muscle glycolytic and oxidative enzyme capacities are determinants of insulin sensitivity and muscle composition in obese women. FASEB J. 1995;9(2):273-8.
7. LeBrasseur NK, Walsh K, Arany Z. Metabolic benefits of resistance training and fast glycolytic skeletal muscle. Am J Physiol Endocrinol Metab. 2011;300(1):E3-10.
8. Zanuso S, Jimenez A, Pugliese G, Corigliano G, Balducci S. Exercise for the management of type 2 diabetes: a review of the evidence. Acta Diabetol. 2010;47(1):15-22.
9. Muoio DM, Way JM, Tanner CJ, Winegar DA, Kliewer SA, Houmard JA, et al. Peroxisome proliferator-activated receptor-alpha regulates fatty acid utilization in primary human skeletal muscle cells. Diabetes. 2002;51(4):901-9.
10. Finck BN, Lehman JJ, Leone TC, Welch MJ, Bennett MJ, Kovacs A, et al. The cardiac phenotype induced by PPARalpha overexpression mimics that caused by diabetes mellitus. J Clin Invest. 2002;109(1):121-30.
11. Schuler M, Ali F, Chambon C, Duteil D, Bornert JM, Tardivel A, et al. PGC1alpha expression is controlled in skeletal muscles by PPARbeta, whose ablation results in fiber-type switching, obesity, and type 2 diabetes. Cell Metab. 2006;4(5):407-14.
12. Norris AW, Chen L, Fisher SJ, Szanto I, Ristow M, Jozsi AC, et al. Muscle-specific PPARgamma-deficient mice develop increased adiposity and insulin resistance but respond to thiazolidinediones. J Clin Invest. 2003;112(4):608-18.
13. Ruas JL, White JP, Rao RR, Kleiner S, Brannan KT, Harrison BC, et al. A PGC-1alpha isoform induced by resistance training regulates skeletal muscle hypertrophy. Cell. 2012;151(6):1319-31.

14. Kubat GB, Bouhamida E, Ulger O, Turkel I, Pedriali G, Ramaccini D, et al. Mitochondrial dysfunction and skeletal muscle atrophy: Causes, mechanisms, and treatment strategies. Mitochondrion. 2023;72:33-58.
15. Jaiswal N, Gavin M, Loro E, Sostre-Colon J, Roberson PA, Uehara K, et al. AKT controls protein synthesis and oxidative metabolism via combined mTORC1 and FOXO1 signalling to govern muscle physiology. J Cachexia Sarcopenia Muscle. 2022;13(1):495-514.
16. Manning BD, Toker A. AKT/PKB Signaling: Navigating the Network. Cell. 2017;169(3):381-405.
17. Blaauw B, Canato M, Agatea L, Toniolo L, Mammucari C, Masiero E, et al. Inducible activation of Akt increases skeletal muscle mass and force without satellite cell activation. FASEB J. 2009;23(11):3896-905.
18. Musaro A, McCullagh K, Paul A, Houghton L, Dobrowolny G, Molinaro M, et al. Localized Igf-1 transgene expression sustains hypertrophy and regeneration in senescent skeletal muscle. Nat Genet. 2001;27(2):195-200.
19. Navegantes LC, Resano NM, Migliorini RH, Kettelhut IC. Role of adrenoceptors and cAMP on the catecholamine-induced inhibition of proteolysis in rat skeletal muscle. Am J Physiol Endocrinol Metab. 2000;279(3):E663-8.
20. Goncalves DA, Silveira WA, Manfredi LH, Graca FA, Armani A, Bertaggia E, et al. Insulin/IGF1 signalling mediates the effects of beta(2) -adrenergic agonist on muscle proteostasis and growth. J Cachexia Sarcopenia Muscle. 2019;10(2):455-75.
21. Joassard OR, Amirouche A, Gallot YS, Desgeorges MM, Castells J, Durieux AC, et al. Regulation of Akt-mTOR, ubiquitin-proteasome and autophagy-lysosome pathways in response to formoterol administration in rat skeletal muscle. Int J Biochem Cell Biol. 2013;45(11):2444-55.
22. Mina E, Wyart E, Sartori R, Angelino E, Zaggia I, Rausch V, et al. FK506 bypasses the effect of erythroferrone in cancer cachexia skeletal muscle atrophy. Cell Rep Med. 2023;4(12):101306.
23. Sartori R, Milan G, Patron M, Mammucari C, Blaauw B, Abraham R, et al. Smad2 and 3 transcription factors control muscle mass in adulthood. Am J Physiol Cell Physiol. 2009;296(6):C1248-57.
24. Sartori R, Hagg A, Zampieri S, Armani A, Winbanks CE, Viana LR, et al. Perturbed BMP signaling and denervation promote muscle wasting in cancer cachexia. Sci Transl Med. 2021;13(605).
25. Tando T, Hirayama A, Furukawa M, Sato Y, Kobayashi T, Funayama A, et al. Smad2/3 Proteins Are Required for Immobilization-induced Skeletal Muscle Atrophy. J Biol Chem. 2016;291(23):12184-94.
26. Sandri M, Sandri C, Gilbert A, Skurk C, Calabria E, Picard A, et al. Foxo transcription factors induce the atrophy-related ubiquitin ligase atrogin-1 and cause skeletal muscle atrophy. Cell. 2004;117(3):399-412.

27. Shimizu N, Yoshikawa N, Ito N, Maruyama T, Suzuki Y, Takeda S, et al. Crosstalk between glucocorticoid receptor and nutritional sensor mTOR in skeletal muscle. Cell Metab. 2011;13(2):170-82.
28. Stitt TN, Drujan D, Clarke BA, Panaro F, Timofeyva Y, Kline WO, et al. The IGF-1/PI3K/Akt pathway prevents expression of muscle atrophy-induced ubiquitin ligases by inhibiting FOXO transcription factors. Mol Cell. 2004;14(3):395-403.
29. Cai D, Frantz JD, Tawa NE, Jr., Melendez PA, Oh BC, Lidov HG, et al. IKKbeta/NF-kappaB activation causes severe muscle wasting in mice. Cell. 2004;119(2):285-98.
30. Bonetto A, Aydogdu T, Jin X, Zhang Z, Zhan R, Puzis L, et al. JAK/STAT3 pathway inhibition blocks skeletal muscle wasting downstream of IL-6 and in experimental cancer cachexia. Am J Physiol Endocrinol Metab. 2012;303(3):E410-21.
31. Jun L, Robinson M, Geetha T, Broderick TL, Babu JR. Prevalence and Mechanisms of Skeletal Muscle Atrophy in Metabolic Conditions. Int J Mol Sci. 2023;24(3).
32. Sandri M. Protein breakdown in muscle wasting: role of autophagy-lysosome and ubiquitin-proteasome. Int J Biochem Cell Biol. 2013;45(10):2121-9.
33. Clarke BA, Drujan D, Willis MS, Murphy LO, Corpina RA, Burova E, et al. The E3 Ligase MuRF1 degrades myosin heavy chain protein in dexamethasone-treated skeletal muscle. Cell Metab. 2007;6(5):376-85.
34. Tintignac LA, Lagirand J, Batonnet S, Sirri V, Leibovitch MP, Leibovitch SA. Degradation of MyoD mediated by the SCF (MAFbx) ubiquitin ligase. J Biol Chem. 2005;280(4):2847-56.
35. Nagpal P, Plant PJ, Correa J, Bain A, Takeda M, Kawabe H, et al. The ubiquitin ligase Nedd4-1 participates in denervation-induced skeletal muscle atrophy in mice. PLoS One. 2012;7(10):e46427.
36. Kumar A, Bhatnagar S, Paul PK. TWEAK and TRAF6 regulate skeletal muscle atrophy. Curr Opin Clin Nutr Metab Care. 2012;15(3):233-9.
37. Sartori R, Schirwis E, Blaauw B, Bortolanza S, Zhao J, Enzo E, et al. BMP signaling controls muscle mass. Nat Genet. 2013;45(11):1309-18.
38. Milan G, Romanello V, Pescatore F, Armani A, Paik JH, Frasson L, et al. Regulation of autophagy and the ubiquitin-proteasome system by the FoxO transcriptional network during muscle atrophy. Nat Commun. 2015;6:6670.
39. Mammucari C, Milan G, Romanello V, Masiero E, Rudolf R, Del Piccolo P, et al. FoxO3 controls autophagy in skeletal muscle in vivo. Cell Metab. 2007;6(6):458-71.
40. Mizushima N, Komatsu M. Autophagy: renovation of cells and tissues. Cell. 2011;147(4):728-41.

41. Penna F, Costamagna D, Pin F, Camperi A, Fanzani A, Chiarpotto EM, et al. Autophagic degradation contributes to muscle wasting in cancer cachexia. Am J Pathol. 2013;182(4):1367-78.
42. Wohlgemuth SE, Seo AY, Marzetti E, Lees HA, Leeuwenburgh C. Skeletal muscle autophagy and apoptosis during aging: effects of calorie restriction and life-long exercise. Exp Gerontol. 2010;45(2):138-48.
43. Mofarrahi M, Sigala I, Guo Y, Godin R, Davis EC, Petrof B, et al. Autophagy and skeletal muscles in sepsis. PLoS One. 2012;7(10):e47265.
44. O'Leary MF, Vainshtein A, Carter HN, Zhang Y, Hood DA. Denervation-induced mitochondrial dysfunction and autophagy in skeletal muscle of apoptosis-deficient animals. Am J Physiol Cell Physiol. 2012;303(4):C447-54.
45. Grumati P, Coletto L, Schiavinato A, Castagnaro S, Bertaggia E, Sandri M, et al. Physical exercise stimulates autophagy in normal skeletal muscles but is detrimental for collagen VI-deficient muscles. Autophagy. 2011;7(12):1415-23.
46. Castets P, Lin S, Rion N, Di Fulvio S, Romanino K, Guridi M, et al. Sustained activation of mTORC1 in skeletal muscle inhibits constitutive and starvation-induced autophagy and causes a severe, late-onset myopathy. Cell Metab. 2013;17(5):731-44.
47. Fearon K, Strasser F, Anker SD, Bosaeus I, Bruera E, Fainsinger RL, et al. Definition and classification of cancer cachexia: an international consensus. Lancet Oncol. 2011;12(5):489-95.
48. Ferrer M, Anthony TG, Ayres JS, Biffi G, Brown JC, Caan BJ, et al. Cachexia: A systemic consequence of progressive, unresolved disease. Cell. 2023;186(9):1824-45.
49. Argiles JM, Stemmler B, Lopez-Soriano FJ, Busquets S. Inter-tissue communication in cancer cachexia. Nat Rev Endocrinol. 2018;15(1):9-20.
50. Wyart E, Bindels LB, Mina E, Menga A, Stanga S, Porporato PE. Cachexia, a Systemic Disease beyond Muscle Atrophy. Int J Mol Sci. 2020;21(22).
51. Argiles JM, Busquets S, Stemmler B, Lopez-Soriano FJ. Cancer cachexia: understanding the molecular basis. Nat Rev Cancer. 2014;14(11):754-62.
52. Zhang G, Liu Z, Ding H, Miao H, Garcia JM, Li YP. Toll-like receptor 4 mediates Lewis lung carcinoma-induced muscle wasting via coordinate activation of protein degradation pathways. Sci Rep. 2017;7(1):2273.
53. Bonetto A, Rupert JE, Barreto R, Zimmers TA. The Colon-26 Carcinoma Tumor-bearing Mouse as a Model for the Study of Cancer Cachexia. J Vis Exp. 2016(117).
54. Guarnier FA, Cecchini AL, Suzukawa AA, Maragno AL, Simao AN, Gomes MD, et al. Time course of skeletal muscle loss and oxidative stress in rats with Walker 256 solid tumor. Muscle Nerve. 2010;42(6):950-8.

55. Llovera M, Garcia-Martinez C, Agell N, Lopez-Soriano FJ, Argiles JM. Muscle wasting associated with cancer cachexia is linked to an important activation of the ATP-dependent ubiquitin-mediated proteolysis. Int J Cancer. 1995;61(1):138-41.
56. Baltgalvis KA, Berger FG, Pena MM, Davis JM, Muga SJ, Carson JA. Interleukin-6 and cachexia in ApcMin/+ mice. Am J Physiol Regul Integr Comp Physiol. 2008;294(2):R393-401.
57. Michaelis KA, Zhu X, Burfeind KG, Krasnow SM, Levasseur PR, Morgan TK, et al. Establishment and characterization of a novel murine model of pancreatic cancer cachexia. J Cachexia Sarcopenia Muscle. 2017;8(5):824-38.
58. Talbert EE, Cuitino MC, Ladner KJ, Rajasekerea PV, Siebert M, Shakya R, et al. Modeling Human Cancer-induced Cachexia. Cell Rep. 2019;28(6):1612-22 e4.
59. Guarino M, Perna B, Cesaro AE, Maritati M, Spampinato MD, Contini C, et al. 2023 Update on Sepsis and Septic Shock in Adult Patients: Management in the Emergency Department. J Clin Med. 2023;12(9).
60. Cohen J. The immunopathogenesis of sepsis. Nature. 2002;420(6917):885-91.
61. Winkelman C. The role of inflammation in ICU-acquired weakness. Crit Care. 2010;14(4):186.
62. Shanely RA, Zergeroglu MA, Lennon SL, Sugiura T, Yimlamai T, Enns D, et al. Mechanical ventilation-induced diaphragmatic atrophy is associated with oxidative injury and increased proteolytic activity. Am J Respir Crit Care Med. 2002;166(10):1369-74.
63. Goligher EC, Dres M, Fan E, Rubenfeld GD, Scales DC, Herridge MS, et al. Mechanical Ventilation-induced Diaphragm Atrophy Strongly Impacts Clinical Outcomes. Am J Respir Crit Care Med. 2018;197(2):204-13.
64. Doganyigit Z, Eroglu E, Akyuz E. Inflammatory mediators of cytokines and chemokines in sepsis: From bench to bedside. Hum Exp Toxicol. 2022;41:9603271221078871.
65. Seixas M, Mitre LP, Shams S, Lanzuolo GB, Bartolomeo CS, Silva EA, et al. Unraveling Muscle Impairment Associated With COVID-19 and the Role of 3D Culture in Its Investigation. Front Nutr. 2022;9:825629.
66. Montes-Ibarra M, Oliveira CLP, Orsso CE, Landi F, Marzetti E, Prado CM. The Impact of Long COVID-19 on Muscle Health. Clin Geriatr Med. 2022;38(3):545-57.

Aims of the work

Chapter 1

My Ph.D. journey began during the SARS-CoV-2 pandemic, a time when millions of people worldwide were affected by COVID-19. The knowledge about this novel virus was very limited, and we all wondered about its potential long-term effects on our health. It quickly became evident that many individuals experienced a severe cytokine storm following infection, leading to intense respiratory symptoms and, in the worst cases, organ dysfunction and the need for mechanical ventilation. This resulted in the rapid saturation of Intensive Care Units (ICUs) in Italy and around the world.

Our lab focuses on the pathophysiology of the skeletal muscle, with a particular interest in the metabolic and molecular alterations that characterize skeletal muscle atrophy.

Chapter 1 aimed to determine whether patients under invasive mechanical ventilation (IMV) with inflammatory diseases (i.e., COVID-19, sepsis, pneumonia) were more prone to developing skeletal muscle atrophy compared to ICU patients without systemic inflammation. *In vitro,* we investigated whether certain inflammatory mediators present in the plasma of these patients could induce atrophy and mitochondrial dysfunction. Moreover, we also evaluated the effects of extracellular vesicles (EVs) derived from adipose-derived stromal stem cells (ASC) to assess their potential as a therapy for infection- and ICU-induced muscle atrophy.

Chapter 2

Systemic inflammation is known to cause mitochondrial dysfunction and skeletal muscle atrophy. Besides viral and bacterial infections explored in Chapter 1, cancer is another disease that causes dysfunction in several organs due to systemic inflammation.

Cancer cachexia is a poorly understood wasting condition associated with certain types of cancer: it decreases the response to anticancer therapies, and it is responsible for at least 30% of deaths in advanced cancer cases.

Growing evidence suggests that mitochondrial dysfunction plays a central role in promoting skeletal muscle atrophy in cancer cachexia, however, the panel of molecular mechanisms driving wasting remain poorly investigated.

Systemic iron metabolism is often disrupted in cancer patients, as evidenced by the high prevalence of anemia among them. Interestingly, the types of tumors that lead to anemia are also those that make patients more prone to developing cachexia. Of note, iron is an essential element for mitochondrial function and proper energy production, being a crucial component of heme and iron-sulfur clusters.

In the study in Chapter 2 we aimed at determining whether systemic iron alterations occurring in cancer could negatively impact mitochondrial function, directly contributing to the development of muscle atrophy. Additionally, we evaluated whether iron supplementation, a widely used treatment for anemic patients, could be beneficial for limiting wasting and muscle force loss.

Chapter 3

Chapter 3 of this thesis represents the core of my Ph.D. project. During our study on the alterations of iron metabolism in cancer cachexia-induced skeletal muscle atrophy described in Chapter 2, we identified erythroferrone (ERFE) as a significantly upregulated iron-related gene in cachexia. ERFE is a hormone that increases systemic iron availability, and it is secreted by erythroblasts acting as an inhibitor of BMP-Smad1/5/8 signaling.

The aims of Chapter 3 were to determine the role of ERFE and the mechanism behind its upregulation in cancer-induced skeletal muscle atrophy. Once we found its impact on the downregulation of BMP-Smad1/5/8 signaling, we explored a pharmacological intervention using the drug FK506 (tacrolimus) to counteract ERFE effects, thereby preventing skeletal muscle atrophy.

Additionally, we aimed to characterize FKBP12, the target of FK506, as we were the first to demonstrate its involvement in the regulation of skeletal muscle mass. This study was published in Cell Reports Medicine in December 2023, and the complete text is included in Chapter 3. Furthermore, a patent has been filed on the novel use of FK506 and on the targeting FKBP12 for treating skeletal muscle atrophy.

Chapter 1

The aim of this study was the evaluation of the effects of invasive mechanical ventilation (IMV) in combination with an inflammatory disease on skeletal muscle atrophy. Particularly, the evaluation over time of the development of diaphragmatic dysfunction and quadriceps atrophy, and the effects of patients' plasma on *in vitro* models of skeletal muscle.

This study was conducted in collaboration with physicians from the Dept. of Anesthesia and Intensive Care from the Città della Salute e della Scienza of Turin. In particular, Prof. Vito Fanelli, MD and the medical doctors Simone Scrivanti, MD and Mattia Monfroglio, MD provided us plasma from patients and healthy donors, extracellular vesicles (EVs) and performed the ultrasound (US) imaging on patients. Prof. Chiara Riganti performed the biochemical measurement of oxidative stress parameters.

Material and Methods

Enrolment in the study

The study included patients admitted to the University of Turin Intensive Care Unit (CAR), at the Città della Salute e della Scienza, according to the following criteria.

Patients were included if undergoing invasive or non-invasive mechanical ventilation within the first 36 hours from intubation or the start of non-invasive ventilation, with a predicted duration exceeding 24 hours, who had been diagnosed with acute respiratory distress syndrome (ARDS), sepsis, septic shock or pneumonia. These patients have been defined as "cases" for the US imaging. Control patients underwent invasive or non-invasive mechanical ventilation within the first 36 hours from intubation or the start of non-invasive ventilation, with a predicted duration exceeding 24 hours, without the aforementioned diagnosis. Patients were excluded if younger than 18 years-old, in case of pregnancy, with a diagnosis of neuromuscular disease or with chronic obstructive pulmonary disease (COPD) on home oxygen therapy.

For what concerns Covid-19 patients, they were in ICU with a diagnosis of ARDS, with ExtraCorporeal Membrane Oxygenation (ECMO) to allow blood oxygenation independently from the lungs, with invasive mechanical ventilation. Due to the emergency of the situation, US analysis for skeletal muscle atrophy had not been performed.

Evaluation of skeletal muscle atrophy in patients

Diaphragm dysfunction and quadriceps atrophy was determined with US imaging and quantified with the Horos software. Severe diaphragmatic dysfunction was defined in case of hypertrophy or atrophy over the 20% of the basal value according to Santana et al[1].

US imaging and blood collection occurred multiple times from the admission to ICU. Specifically, within 36 hours of admission (T1), 3 days (T3), 7 days (T7), and 14 days after enrollment (T14).

Plasma collection in patients

At each follow-up time, two tubes of arterial blood were collected and centrifuged at 1500 rpm at 4°C for 10 minutes on the same day. Following the separation of the liquid and cellular parts, the plasma was extracted under a hood, placed in 1.5 ml cryotubes, and stored in a freezer at -80°C with appropriate labeling.

In vitro analyses with myotubes

C2C12 myoblasts (ATCC CRL-1772) were cultured in DMEM/10% FBS. When 80-90% confluence was reached, they were differentiated into myotubes in DMEM/2% HS medium for 4 days. Subsequently, the myotubes were treated with plasma taken from patients and healthy donors diluted to 15% in DMEM/2% HS. When indicated, equal parts of three Covid-19 patients were pooled and used for *in vitro* analyses at a final concentration of 15% in differentiation medium. Subsequently, 520.000.000/cm^2 of extracellular vesicles (EVs) derived from human adipose-derived stromal stem cells (ASC) were added to the myotubes 6 hours post-plasma treatment. The ASC derived from lipoaspirates from three donors, and the isolation of ASC-derived EVs was performed as previously described[2].

Myotubes were analyzed 48 hours post-plasma treatment, capturing images with bright field microscopy (Zeiss) at 20X magnification and quantified with the software FIJI.

At the same timepoint, biochemical analyses of oxidative stress parameters were performed on snap-frozen pelleted myotubes as previously described[3].

Results

In order to understand whether IMV caused muscle atrophy in patients, the measurement of diaphragm thickness and quadriceps cross-sectional area was performed. No significant differences were observed in the timeframe from T1 to T7 (data not shown) in cases patients compared to controls. However, a significant decrease of diaphragmatic thickness was observed in cases after two weeks of IMV, if compared to T1, as a clear sign of diaphragm dysfunction (Fig. 1A).

In coherence with these results, quadriceps cross-sectional area measured by US imaging was significantly reduced in cases patients both at T7 and T14 (Fig. 1B), indicating the development of a significant skeletal muscle atrophy in different compartments.

Interestingly, control patients did not show quadriceps or diaphragm atrophy, indicating that IMV only when in combination with systemic inflammation is more responsible for muscle atrophy, rather than bed rest and IMV alone.

To verify whether the inflammatory mediators present in the plasma of patients might be directly responsible for skeletal muscle atrophy, we treated C2C12 myotubes with plasma derived from various patients in ICU for Covid-19-induced ARDS, and with plasma from healthy donors.

Interestingly, all patients' plasma induced a significant myotube atrophy of around 15-20% (Fig. 1C) and the same result was obtained when myotubes were treated with a mixture of pooled patients' plasma (Fig. 1D). We next aimed at rescuing plasma-induced atrophy by treating C2C12 myotubes with adipose-derived stromal stem cell (ASC)-derived extracellular vesicles (EVs), known for their anti-inflammatory properties[4]. The treatment with EVs significantly rescued the atrophy

induced by Covid-19 patients' plasma, representing a potential therapeutic opportunity for this model (Fig.1C, D).

Since it is known that inflammatory mediators cause skeletal muscle atrophy by inducing mitochondrial dysfunction, we then assessed whether there were signs of oxidative stress, and the eventual effects of EVs supplementation.

Interestingly, total ROS and mitochondrial ROS were significantly abundant in plasma-treated myotubes, and the levels were completely rescued upon EVs treatment (Fig. 1E, F). As biological readouts of ROS levels, we measured peroxidized lipids and carbonylated proteins. The former are the result of hydrocarbon unsaturated bonds oxidation, while the latter of the oxidation of proteins' aminoacidic side chains. Coherently, both parameters resulted to be increased in atrophic myotubes and rescued by EVs (Fig. 1G, H).

On the other hand, we estimated the levels of glutathione, the main antioxidant tripeptide, that exists in the reduced (GSH) and oxidized (GSSG) form. We observed an increased ratio GSSG/GSH in atrophic myotubes as an indication of a relevant oxidative stress. However, when supplemented with EVs, the myotubes reached a GSSG/GSH ratio similar to untreated cells (Fig. 1I-J).

Figures

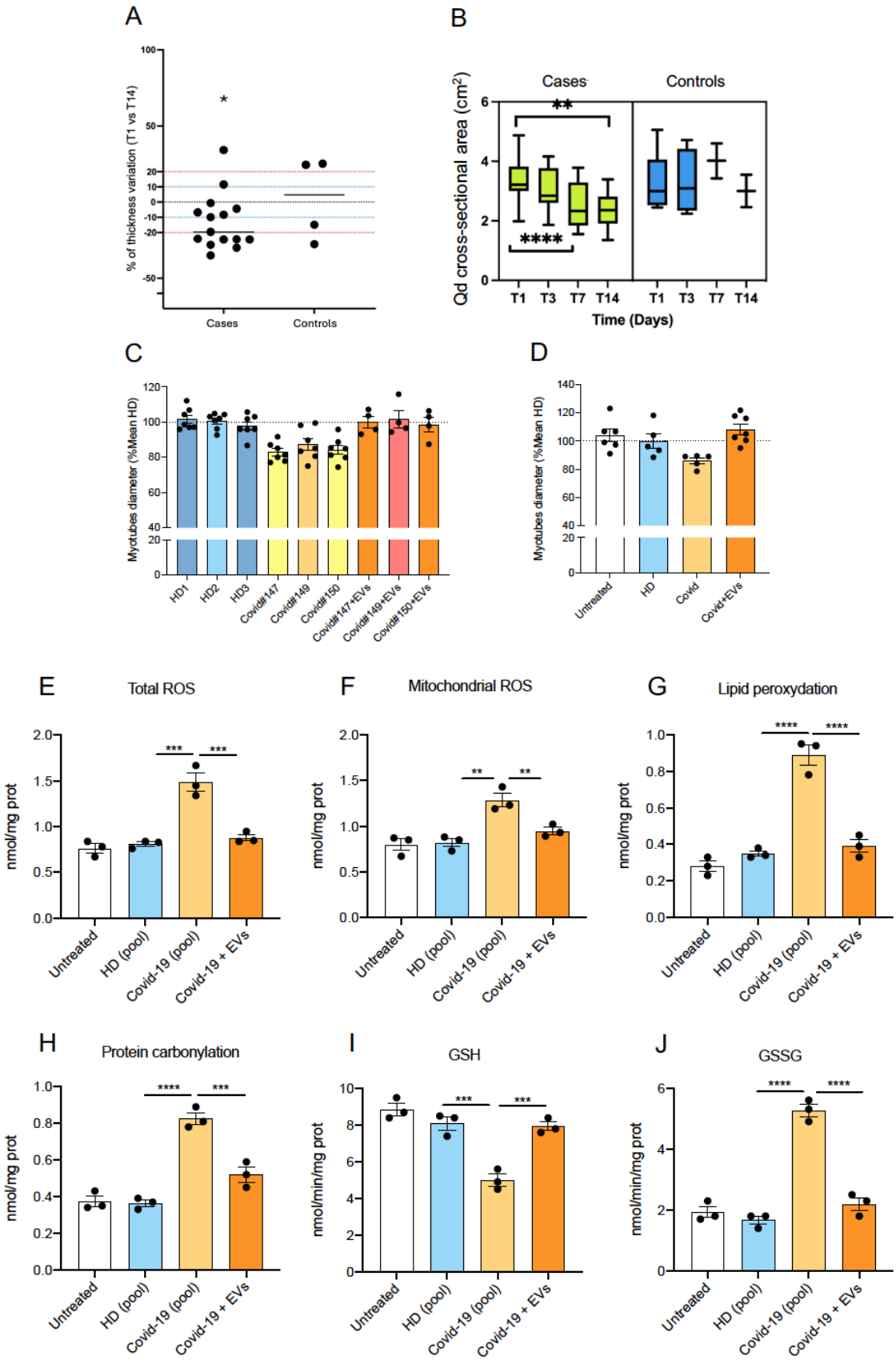
A
% of thickness variation (T1 vs T14)
Cases
Controls
B
Cases
Controls
Qd cross-sectional area (cm²)
T1 T3 T7 T14 T1 T3 T7 T14
Time (Days)
C
Myotubes diameter (%Mean HD)
HD1
HD2
HD3
Covid#147
Covid#149
Covid#150
Covid#147+EVs
Covid#149+EVs
Covid#150+EVs
D
Myotubes diameter (%Mean HD)
Untreated
HD
Covid
Covid+EVs
E
Total ROS
nmol/mg prot
F
Mitochondrial ROS
nmol/mg prot
G
Lipid peroxydation
nmol/mg prot
Untreated
HD (pool)
Covid-19 (pool)
Covid-19 + EVs
H
Protein carbonylation
nmol/mg prot
I
GSH
nmol/min/mg prot
J
GSSG
nmol/min/mg prot

Figure 1. Characterization of skeletal muscle atrophy induced by inflammation in patients and in vitro.

A) Percentage variation of median diaphragm thickness at T14 compared to T1. The range is defined as: 10% increase – *hypertrophy;* 20% increase – *severe hypertrophy;* 10% decrease – *atrophy;* 20% decrease – *severe atrophy*. (cases=15, controls=4) **B)** Variation of the quadriceps cross-sectional area in cases vs control at various timepoints, measured with US imaging (cases=21, controls=5). **C-D)** C2C12 myotubes diameters, expressed as % of the mean of HD, or pooled (**D**), 48h post plasma treatment, with or without EVs. (HD = healthy donor; Covid#n = covid patient n#; EVs= extracellular vesicles) (N=3/4). **E-J)** Metabolic measurement performed in C2C12 myotubes 48h post plasma treatment, with or without EVs: expressed as nmol of total ROS (**E**), mitochondrial ROS (**F**), lipid peroxides (**G**), carbonylated proteins (**H**), reduced (**I**) and oxidized (**J**) glutathione, per mg of proteins extracted. (N=3)

Data information: For all data, N represents the number of biological replicates. Statistical significance was calculated by unpaired, two-tailed Student's t-test (A), or one-way Anova with Bonferroni's correction (C-J). Data are mean SEM. *P<0.05, **P < 0.01, ***P < 0.001, ****P<0.0001.

Conclusion

Acute and persistent infections might lead to complications and necessitate intensive care. Invasive mechanical ventilation (IMV), by completely substituting for patients' voluntary breathing, combined with bedrest, could induce diaphragm and limb muscle atrophy.

Overall, our data suggest that IMV, only when combined with a high inflammatory state, induces significant skeletal muscle atrophy within 7-14 days of ICU stay. This indicates that inflammatory cytokines are directly responsible for the increased muscle wasting due to the enhanced oxidative stress observed in patients' plasma-treated myotubes.Interestingly, if supplemented with ASC-derived EVs, the atrophy of myotubes is reversed, as are the GSH levels, consistent with the reduction of oxidized proteins and lipids.

References

1. Santana PV, Cardenas LZ, Albuquerque ALP, Carvalho CRR, Caruso P. Diaphragmatic ultrasound: a review of its methodological aspects and clinical uses. J Bras Pneumol. 2020 Nov 20;46(6):e20200064. doi: 10.36416/1806-3756/e20200064. PMID: 33237154; PMCID: PMC7909996.
2. Skovronova R, Scaccia E, Calcat-I-Cervera S, Bussolati B, O'Brien T, Bieback K. Adipose stromal cells bioproducts as cell-free therapies: manufacturing and therapeutic dose determine in vitro functionality. J Transl Med. 2023 Oct 16;21(1):723. doi: 10.1186/s12967-023-04602-9. PMID: 37840135; PMCID: PMC10577984.
3. Salaroglio IC, Belisario DC, Akman M, La Vecchia S, Godel M, Anobile DP, Ortone G, Digiovanni S, Fontana S, Costamagna C, Rubinstein M, Kopecka J, Riganti C. Mitochondrial ROS drive resistance to chemotherapy and immune-killing in hypoxic non-small cell lung cancer. J Exp Clin Cancer Res. 2022 Aug 11;41(1):243. doi: 10.1186/s13046-022-02447-6. PMID: 35953814; PMCID: PMC9373288.
4. Lindoso RS, Lopes JA, Binato R, Abdelhay E, Takiya CM, Miranda KR, Lara LS, Viola A, Bussolati B, Vieyra A, Collino F. Adipose Mesenchymal Cells-Derived EVs Alleviate DOCA-Salt-Induced Hypertension by Promoting Cardio-Renal Protection. Mol Ther Methods Clin Dev. 2019 Nov 15;16:63-77. doi: 10.1016/j.omtm.2019.11.002. PMID: 31871958; PMCID: PMC6909095.

Chapter 2

This chapter summarizes the paper titled *"Iron supplementation is sufficient to rescue skeletal muscle mass and function in cancer cachexia."* Only the most relevant data have been selected. Some phrases are directly taken from the manuscript, while others have been adapted to ensure the flow of the text.

Article

SOURCE DATA | TRANSPARENT PROCESS | OPEN ACCESS

EMBO reports

Iron supplementation is sufficient to rescue skeletal muscle mass and function in cancer cachexia

Elisabeth Wyart[1,†], Myriam Y Hsu[1,†], Roberta Sartori[2], Erica Mina[1], Valentina Rausch[1], Elisa S Pierobon[3], Mariarosa Mezzanotte[4], Camilla Pezzini[2], Laure B Bindels[5], Andrea Lauria[6], Fabio Penna[4], Emilio Hirsch[1], Miriam Martini[1], Massimiliano Mazzone[1,7,8], Antonella Roetto[4], Simonetta Geninatti Crich[1], Hans Prenen[9,10], Marco Sandri[2], Alessio Menga[1,‡] & Paolo E Porporato[1,*,‡]

1 Department of Molecular Biotechnology and Health Sciences, Molecular Biotechnology Center, University of Torino, Turin, Italy
2 Department of Biomedical Sciences, University of Padova, Padova, Italy
3 Department of Surgical, Oncological and Gastroenterological Sciences, Padova University Hospital, Padova, Italy
4 Department of Clinical and Biological Sciences, University of Torino, Turin, Italy
5 Metabolism and Nutrition Research Group, Louvain Drug Research Institute, Université catholique de Louvain (UCLouvain), Brussels, Belgium
6 Department of Life Sciences and System Biology, University of Torino, Turin, Italy
7 Laboratory of Tumor Inflammation and Angiogenesis, Center for Cancer Biology (CCB), Vlaams Instituut voor Biotechnologie (VIB), Leuven, Belgium
8 Laboratory of Tumor Inflammation and Angiogenesis, Department of Oncology, Katholieke Universiteit Leuven (KUL), Leuven, Belgium
9 Department of Medical Oncology, University Hospital Antwerp, Edegem, Belgium
10 Center for Oncological Research (CORE), Integrated Personalized and Precision Oncology Network (IPPON), University of Antwerp, Antwerp, Belgium
*Corresponding author. Tel: +39 0116706422; E-mail: paolo.porporato@unito.it
†These authors contributed equally to this work as first authors
‡These authors contributed equally to this work as senior authors

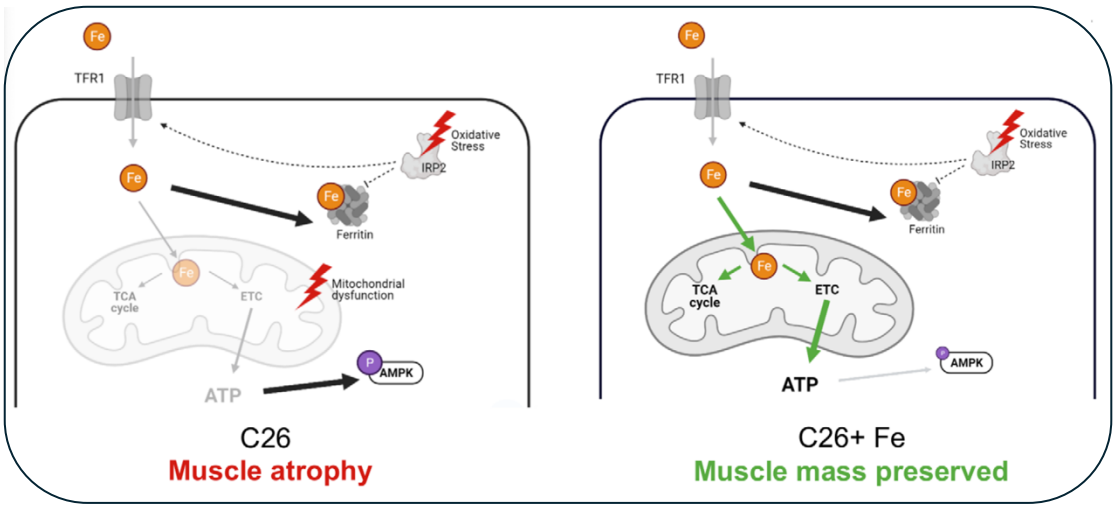

Abstract

Cachexia is a wasting syndrome characterized by devastating skeletal muscle atrophy that dramatically increases mortality in various diseases, most notably in cancer patients with a penetrance of up to 80%. Knowledge regarding the mechanism of cancer-induced cachexia remains very scarce, making cachexia an unmet medical need. In this study, we discovered strong alterations of iron metabolism in the skeletal muscle of both cancer patients and tumor-bearing mice, characterized by decreased iron availability in mitochondria. We found that modulation of iron levels directly influences myotube size in vitro and muscle mass in otherwise healthy mice. Furthermore, iron supplementation was sufficient to preserve both muscle function and mass, prolong survival in tumor-bearing mice, and even rescues strength in human subjects within an unexpectedly short time frame. Importantly, iron supplementation refuels mitochondrial oxidative metabolism and energy production. Overall, our findings provide new mechanistic insights in cancer-induced skeletal muscle wasting, and support targeting iron metabolism as a potential therapeutic option for muscle wasting diseases.

Introduction

As mentioned previously, systemic inflammation induces skeletal muscle atrophy, and in cancer contexts it can lead to cachexia. It is well known how chronic inflammation hampers iron absorption from the diet and causes iron retention in reticuloendothelial cells, which results in insufficient iron availability to meet the body's needs. Iron deficiency is diagnosed in more than half of patients afflicted with colorectal, lung, and pancreatic cancers, which are also associated with high prevalence of cachexia (Ludwig *et al*, 2013).

Iron is indeed a versatile cofactor essential to a multitude of vital metabolic processes including oxygen supply, DNA synthesis, redox homeostasis, or energy metabolism. Iron is indispensable for the activity of several mitochondrial enzymes involved in the TCA cycle and the electron transport chain, where iron is found under the form of heme or iron–sulfur cluster (ISC).

Notably, both iron accumulation and iron deficiency are detrimental to mitochondrial function. Cellular iron homeostasis is thus a tightly regulated process involving a broad variety of proteins responsible for its transport (transferrin), uptake (transferrin receptor/TFR1), storage (ferritin/FT), and export (ferroportin/FPN1). The fine tuning of intracellular iron metabolism is made possible by the Iron Responsive Element/Iron Responsive Protein (IRE/IRP) system exerting a major control on the translation of several key iron-related proteins.

In the skeletal muscle, iron is particularly needed to support the high metabolic activity required for ATP generation, a requisite for contraction and movement. While mitochondrial dysfunction (in particular, decreased oxidative capacity, inefficient energy production, and altered mitochondrial dynamics) has been proven to promote skeletal muscle wasting in cachexia (Boengler *et al*, 2017; Abrigo *et al*, 2019), little is known about the consequence of altered iron levels on skeletal muscle function and mass. Importantly, iron deficiency is present in most cancer patients, and it has been associated to advanced stage and poor prognosis (Ludwig *et al*, 2013). Hence, we decided to investigate the role of iron metabolism in cancer cachexia-related muscle wasting.

Results

Altered iron metabolism is a feature of cancer-induced cachexia.

To confirm the link between cancer cachexia and iron metabolism in the skeletal muscle, we recreated cancer cachexia in mice using the C26-colon cancer model in Balb/C mice, which led to significant hematocrit reduction, total body weight loss, and muscle mass reduction (Fig. 1A-D). These cachectic mice showed a drastic reduction of TFR1 in the skeletal muscle (Fig. 1E, F) despite no change in liver TFR1 or hepatic iron content (data not shown), suggesting that the regulation of iron metabolism is organ specific. In addition, we observed an overexpression of FT (Fig. 1G), which is apparently not coherent with the reduced levels of TFR1. This can be explained by the levels of carbonylated proteins in cachectic muscles (Fig. 1H), that being signs of oxidative stress, can be causative of an ineffective IRE-IRP system (Cairo *et al*, 1996). Besides the alterations in the iron metabolism genes, no differences were observed in the amount of total muscular iron (Fig. 1I), as an indication of an eventual effect on different cellular compartments.

Cachectic muscles are characterized by mitochondrial iron deficiency and impaired oxidative metabolism.

In most cells, a major amount of iron is taken up by mitochondria to produce ISCs and heme. In the skeletal muscle of C26 tumor-bearing mice, we found a significant reduction of mitochondrial iron and total heme content (Fig. 2A and B), as well as upregulated levels of mitochondrial iron importer mitoferrin 2 (MFRN2) and of the rate-limiting enzyme of heme synthesis aminolevulinic acid synthase 2 (ALAS2) (Fig. 2C, D) (Barman-Aksozen et al, 2019). Given that iron is essential for several enzymes involved in the TCA cycle and mitochondrial oxidative metabolism (OXPHOS) (Xu et al, 2013), we assessed the enzymatic activity of two iron–sulfur proteins, aconitase (ACO) and succinate dehydrogenase (SDH), and found a 50% reduction in the activity of both enzymes in cachectic muscles (Fig. 2E, F). Along with these alterations, we observed a drop in mitochondrial ATP (Fig. 2G) and increased AMPK phosphorylation, denoting mitochondrial dysfunction in cachectic muscles (Zhao et al, 2016) (Fig. 2H). In summary, tumor-bearing mice display remarkable

alterations in muscle iron metabolism coupled with mitochondrial dysfunction, which has been linked to muscle atrophy.

Iron supplementation prevents mitochondrial dysfunction and atrophy *in vitro*.

To verify the hypothesis that cancer-associated iron shortage could cause mitochondrial dysfunction, a known feature of muscle atrophy (Liu *et al*, 2016), we supplemented atrophic C2C12-myotubes with iron. Iron supplementation fully rescued the C26 CM-induced reduction of the oxygen consumption rate (OCR) (Fig. 3A-D). Moreover, microscopic analysis confirmed that iron supplementation prevents C26-induced diameter decrease in myotubes *in vitro* (Fig. 3E).

Iron supplementation rescues skeletal muscle mass and mitochondrial function.

To assess if iron supplementation could prevent cancer-induced muscle atrophy *in vivo*, C26 tumor-bearing mice were *i.v.* treated with ferric carboxymaltose (FeCM) every 5 days post C26 injection. Iron improved notably the grip strength of the C26-tumor bearing mice (Fig. 4A) and prevented the loss of body weight and muscle mass occurring at day 12 after C26 injection (Fig. 4B, C). The protection from atrophy was further confirmed by the cross-sectional area (CSA) distribution and the average CSA, showing a shift toward bigger areas in FeCM-treated mice compared to the C26 tumor-bearing ones (Fig. 4D). These findings were further reinforced by a significant drop of the atrogenes FBXO32 (ATRO1), TRIM63 (MURF1), and DDIT4 (REDD1) mRNA levels (not shown and Fig. 4E).

Moreover, iron supplementation replenished skeletal muscle mitochondria of iron (Fig. 5A) and induced the recovery of aconitase and succinate dehydrogenase enzymatic activity (Fig. 5B, C). In agreement with these findings in mice showing restored mitochondrial metabolism upon iron treatment, we also found a significant increase in mitochondrial ATP content (Fig. 5D) and a drop in AMPK phosphorylation (Fig. 5E, F).

Iron supplementation improves muscle strength in cancer patients

Based on the results obtained in the pre-clinical model of cancer-associated muscle wasting, we measured the handgrip force in cancer patients with severe anemia, who reported muscle weakness, before and after FeCM injection. Improved strength was observed in the dominant hand of all patients, while more than half showed also increased force in the non-dominant hand (Fig. 5G) as short as 4 days after the injection. Together with our data reporting TFR1 downregulation in the skeletal muscle of cachectic patients (data not shown) these findings indicate that altered iron metabolism may contribute to muscle weakness in cachectic patients. Consequently, these results highlight the contribution of iron on both muscle mass and functionality and suggest a new promising therapeutic strategy to counteract cancer-induced skeletal muscle wasting. Altogether, our findings show that iron supplementation prevents cancer-induced cachexia through a recovery of mitochondrial function.

Figures

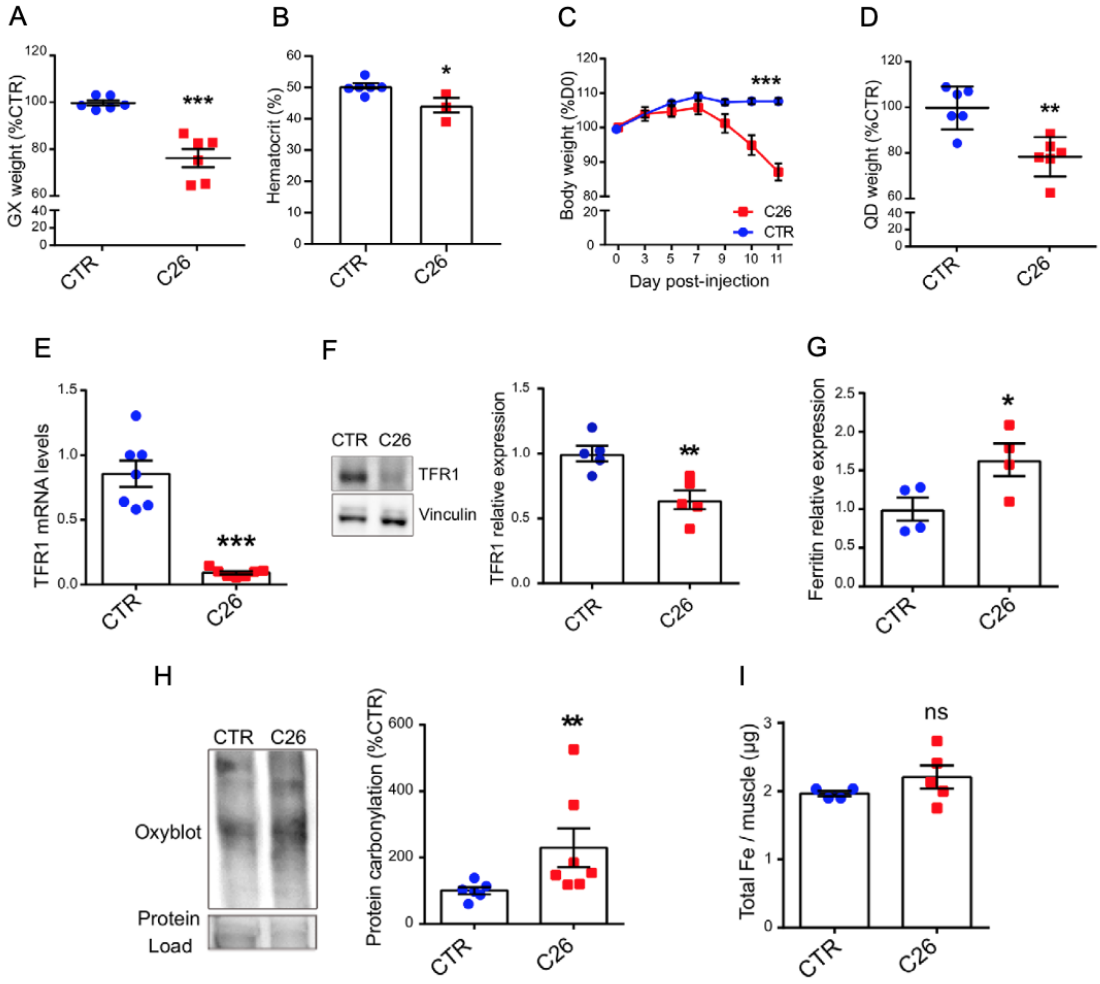

Figure 1. Altered iron metabolism in the skeletal muscle is a feature of cancer-induced cachexia.

A) Gastrocnemius weight normalized to tibial length in C26 tumor-bearing mice on day 12 post C26-injection (n = 6–7). **B)** Hematocrit levels of C26 tumor-bearing mice at day 12 post C26 injection (n = 3–6). **C)** Body weight evolution of mice after C26 injection (n = 6). **D)** Quadriceps weight of C26 tumor-bearing mice normalized to tibial lenght (n = 6). **E)** TFR1 mRNA levels normalized to 18s (n = 6–7). **F)** TFR1 protein expression and densitometric quantification from WB in mouse gastrocnemius (n = 5). **G)** Ferritin protein levels (densitometric quantification from WB) in mouse gastrocnemius (n = 4). **H)** Representative protein carbonylation blot and densitometric quantification in mouse quadriceps (n = 6–7). **I)** ICP-MS quantification of total iron in mouse quadriceps (n = 4–5).

Data information: For all data, n represents the number of biological replicates. Statistical significance was calculated by unpaired, two-tailed Student's t-test. Data are mean SEM. *P < 0.05, **P < 0.01, ***P < 0.001.

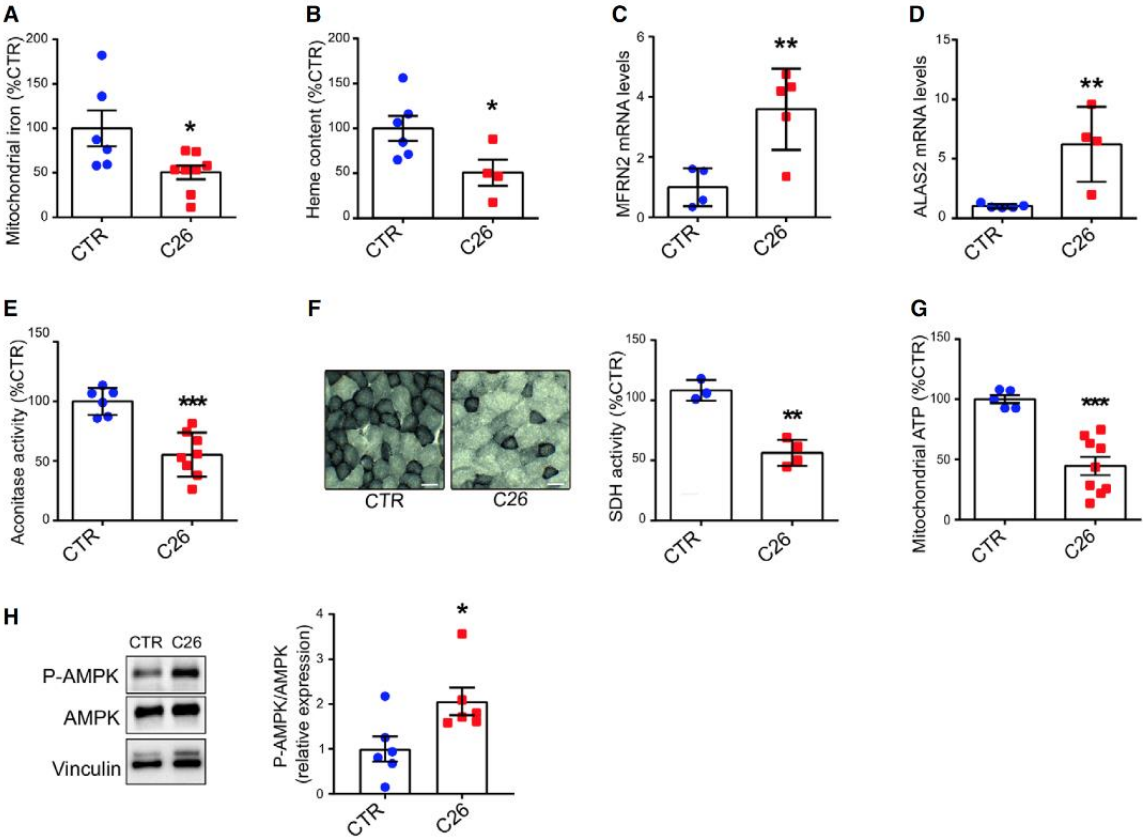

Figure 2. Cachectic muscles are characterized by mitochondrial iron deficiency and impaired oxidative metabolism.

A) ICP-MS quantification of mitochondrial iron in mouse quadriceps (n = 6–8).**B**) Gastrocnemius heme content quantified by fluorescent heme assay (n = 4–6). **C, D**) mRNA levels of mitochondrial iron importer MFRN2 (C) and the rate limiting enzyme of heme synthesis ALAS2 (D) normalized to 18s in mouse gastrocnemius (n = 4–5). **E)** Aconitase activity in mouse quadriceps lysates normalized to protein content (n = 6–8). **F**) Succinate Dehydrogenase activity staining in transversal sections of mouse gastrocnemius and corresponding intensity quantification (n = 3–4). Scale bar = 50 µm. **G)** Mitochondrial ATP content in mouse quadriceps (n = 5–9). **H**) Representative Western blot and densitometric quantification of phospho-AMPK and total AMPK in mouse gastrocnemius (n = 6).

Data information: For all data, n represents the number of biological replicates. Statistical significance was calculated by unpaired, two-tailed Student's t-test. Data aremean SEM. *P < 0.05, **P < 0.01, ***P < 0.001.

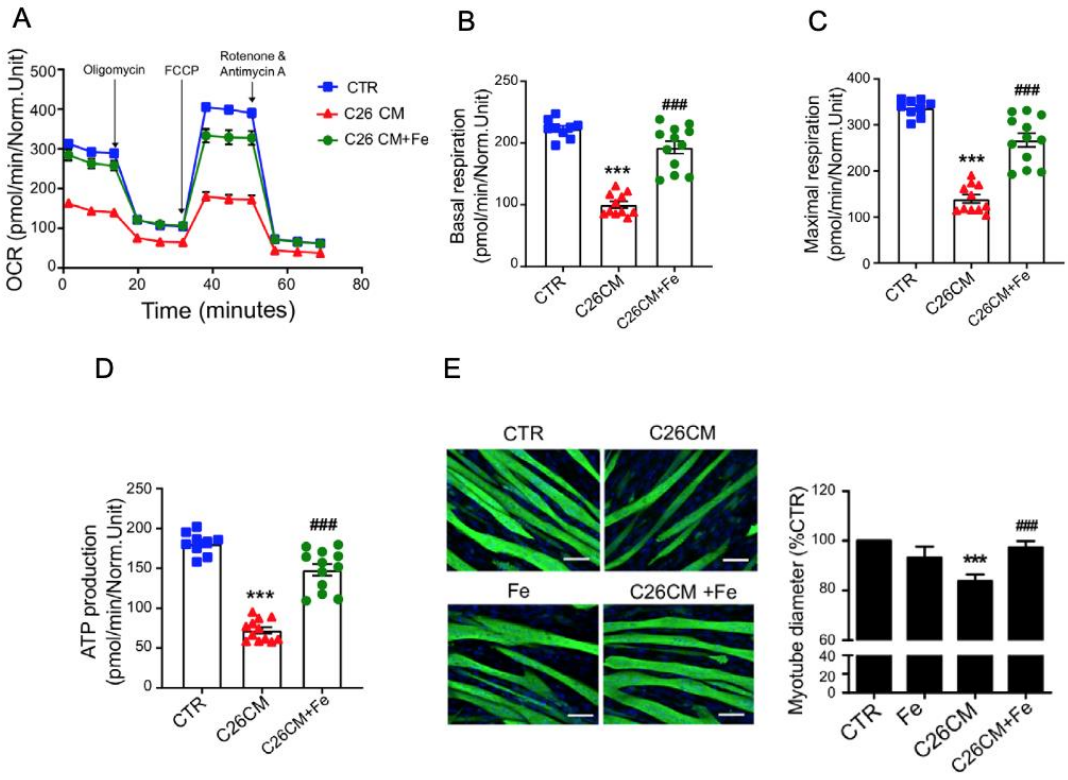

Figure 3. Iron enhances mitochondrial function and prevents cancer-induced myotube atrophy.

A-D) Profile of oxygen consumption rate OCR (A), basal OCR (B), maximal OCR (C), and OCR used for mitochondrial ATP production (D) in C2C12 myotubes after 48 h treatment with C26 CM and ferric citrate supplementation. Data normalized to protein content (n = 9–12). **E)** Representative microscopic pictures and diameter of C2C12 myotubes stained for myosin heavy chain after 48 h treatment with C26 CM and ferric citrate (n = 3 per condition).

Data information: For all data, n represents the number of biological replicates. Statistical significance was calculated by unpaired, two-tailed Student's t-test (A-D), or one-way Anova with Bonferroni's correction (E). Data are mean SEM. **P < 0.01, ***P < 0.001 compared to control and ##P < 0.01, ###P < 0.001 compared to C26 CM-treated group.

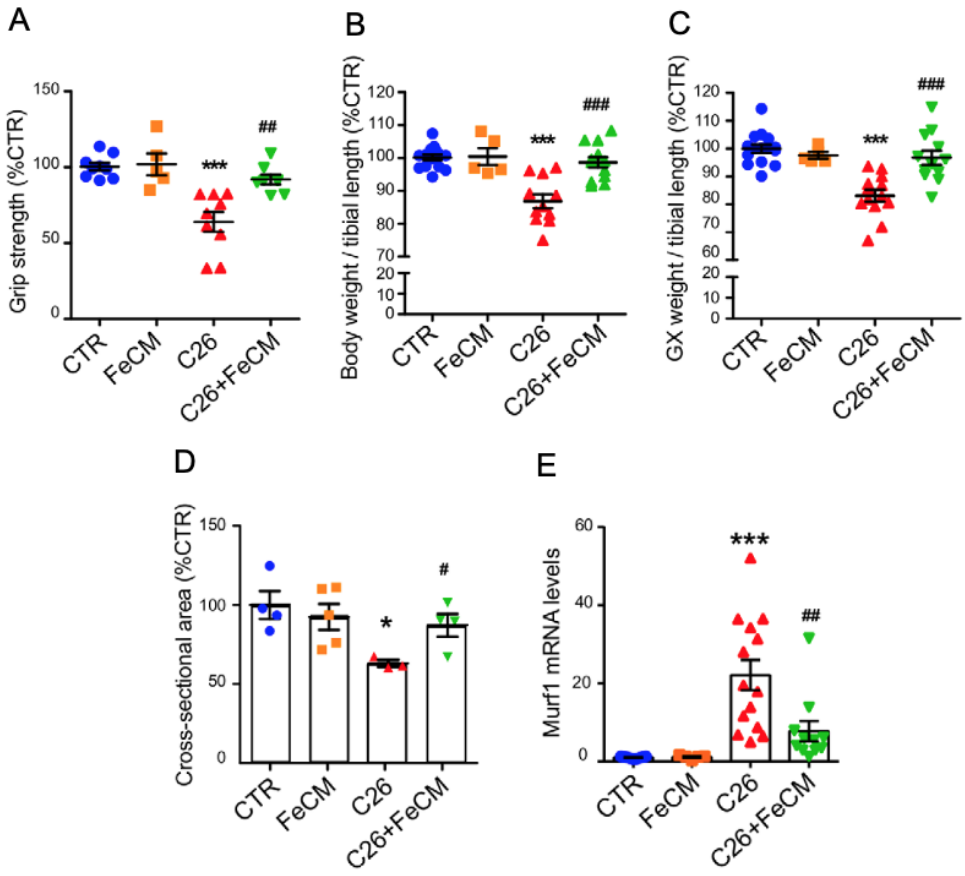

Figure 4. Iron supplementation prevents cancer-induced cachexia.

A) Grip strength of mice measured at day 12 post C26 injection, normalized to average strength of the control group (n = 5–9). **B)** Final body weight of C26 tumor-bearing mice after iron supplementation at day 12 post C26 injection (n = 5–12). **C)** Gastrocnemius weight normalized to tibial length of C26 tumor-bearing mice after iron supplementation at day 12 post C26 injection (n = 5–12). **D)** Average cross-sectional areas of transversal sections of gastrocnemius (midbelly) (n = 3–5). **E)** mRNA levels of Murf 1 normalized to GAPDH in gastrocnemius (n = 5–14).

Data information: For all data, n represents the number of biological replicates. Statistical significance was calculated by one-way Anova with Bonferroni's correction. Data are mean SEM. *P < 0.05 and ***P < 0.001 compared to control and #P < 0.05, ##P < 0.01, ###P < 0.001 compared to C26-untreated group.

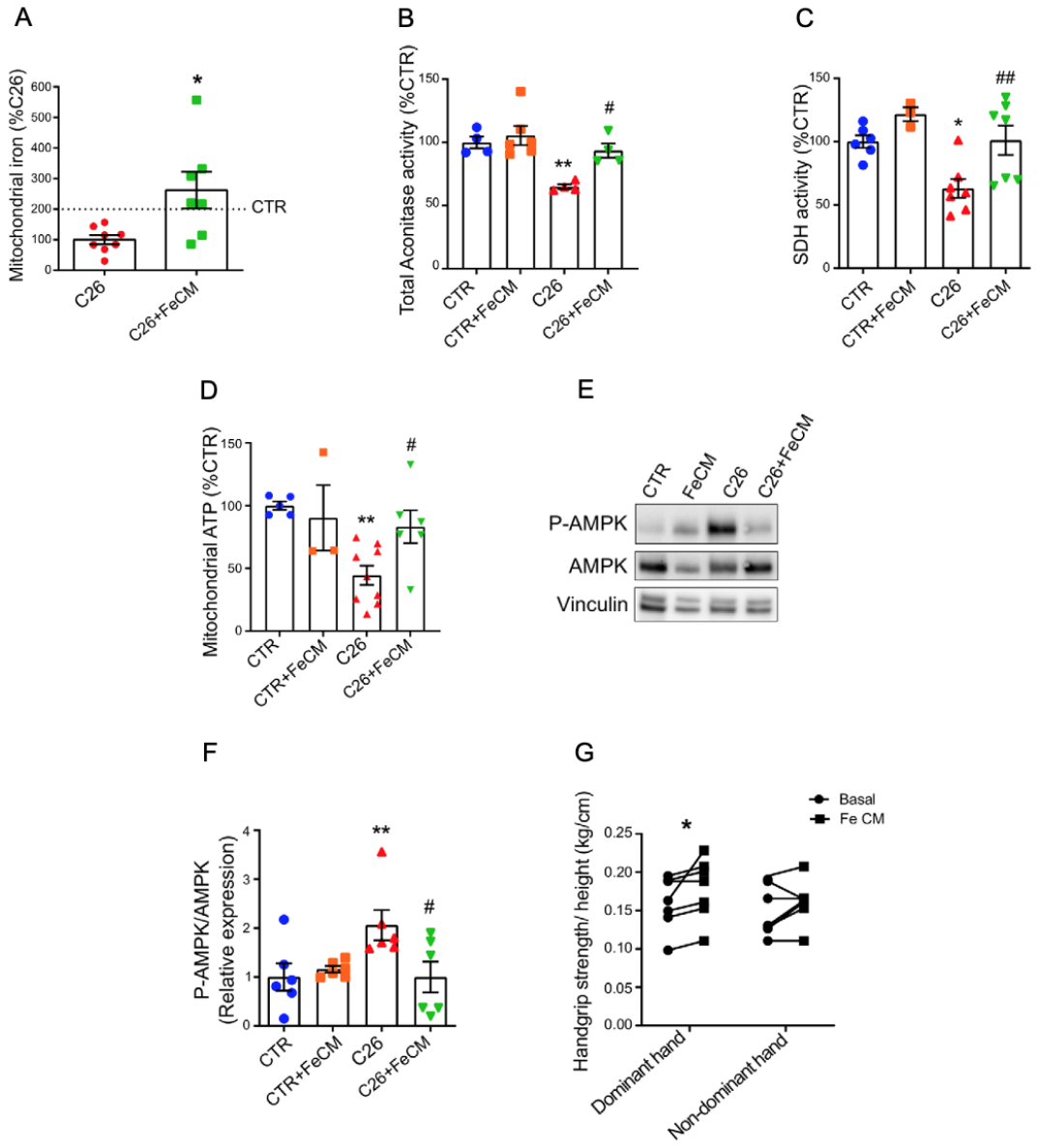

Figure 5. Iron supplementation rescues mitochondrial function.

A) Mitochondrial iron quantified by ICP-MS in quadriceps of C26 tumor-bearing mice after FeCM supplementation (n = 7–8). **B**) Aconitase activity of quadriceps lysates normalized to protein content (n = 3–7). **C**) Succinate Dehydrogenase activity staining of gastrocnemius transversal sections and resulting intensity quantification (n = 3–7). **D**) Mitochondrial ATP content determined by luminescence assay in quadriceps (n = 3–9). **E-F**) Representative Western blot and densitometric quantification (**F**) of phospho-AMPK and total AMPK (stripped and re-blotted) in the gastrocnemius of C26 tumorbearing mice after iron carboxymaltose supplementation (n = 6). **G)** Grip force of dominant or non-dominant arm in iron-deficient cancer patients, expressed as absolute values normalized to height before/after single dose of iron carboxymaltose (15 mg/kg, 7 subjects).

Data information: For all data, n represents the number of biological replicates. Statistical significance was calculated by unpaired, two-tailed Student's t-test. Data are mean SEM. *P < 0.05, **P < 0.01, ***P < 0.001 compared to control and #P < 0.05, ##P < 0.01, ###P < 0.001 compared to C26-untreated group.

Conclusion

Iron deficiency and anemia often occur in cancer patients, and they are linked with symptoms of cachexia such as weakness and fatigue. We propose a novel therapeutic approach, targeting iron metabolism to ameliorate muscle wasting. Indeed, our study uncovers alterations in iron metabolism in the atrophic skeletal muscle of cachectic tumor-bearing mice, notably characterized by reduced iron availability in the mitochondria. This iron dysregulation directly affects muscle mass and function, as evidenced by our findings that iron supplementation can preserve muscle function and mass, extend survival in tumor-bearing mice, and rapidly restore strength in human subjects.

The restoration of muscle mass through iron supplementation not only addresses cancer-induced cachexia but also holds potential for treating muscle atrophy in other conditions associated with iron deficiency, such as COPD and chronic cardiac failure, opening potential new therapeutic strategies aimed at preserving skeletal muscle health by ensuring proper iron homeostasis.

References

Abrigo J, Simon F, Cabrera D, Vilos C, Cabello-Verrugio C (2019) Mitochondrial dysfunction in skeletal muscle pathologies. Curr Protein Pept Sci 20:536 – 546

Barman-Aksozen J, Halloy F, Iyer PS, Schumperli D, Minder AE, Hall J, Minder EI, Schneider-Yin X (2019) Delta-aminolevulinic acid synthase 2 expression combination with iron as modifiers of disease severity in erythropoietic protoporphyria. Mol Genet Metab 128: 304 – 308

Boengler K, Kosiol M, Mayr M, Schulz R, Rohrbach S (2017) Mitochondria and ageing: role in heart, skeletal muscle and adipose tissue. J Cachexia Sarcopenia Muscle 8: 349 – 369

Cairo G, Tacchini L, Recalcati S, Azzimonti B, Minotti G, Bernelli-Zazzera A (1998) Effect of reactive oxygen species on iron regulatory protein activity. Ann N Y Acad Sci 851: 179 – 186

Liu J, Peng Y, Wang X, Fan Y, Qin C, Shi LE, Tang Y, Cao KE, Li H, Long J et al (2016) Mitochondrial dysfunction launches dexamethasone-induced muscle atrophy via AMPK/FOXO3 signaling. Mol Pharm 13: – 84

Ludwig H, Muldur E, Endler G, Hubl W (2013) Prevalence of iron deficiency across different tumors and its association with poor performance status, disease status and anemia. Ann Oncol 24: 1886 – 1892

Xu W, Barrientos T, Andrews NC (2013) Iron and copper in mitochondrial diseases. Cell Metab 17: 319 – 328

Zhao B, Qiang L, Joseph J, Kalyanaraman B, Viollet B, He YY (2016) Mitochondrial dysfunction activates the AMPK signaling and autophagy to cell survival. Genes Dis 3: 82 – 87

Chapter 3

Cell Reports
Medicine

Article

FK506 bypasses the effect of erythroferrone in cancer cachexia skeletal muscle atrophy

Graphical abstract

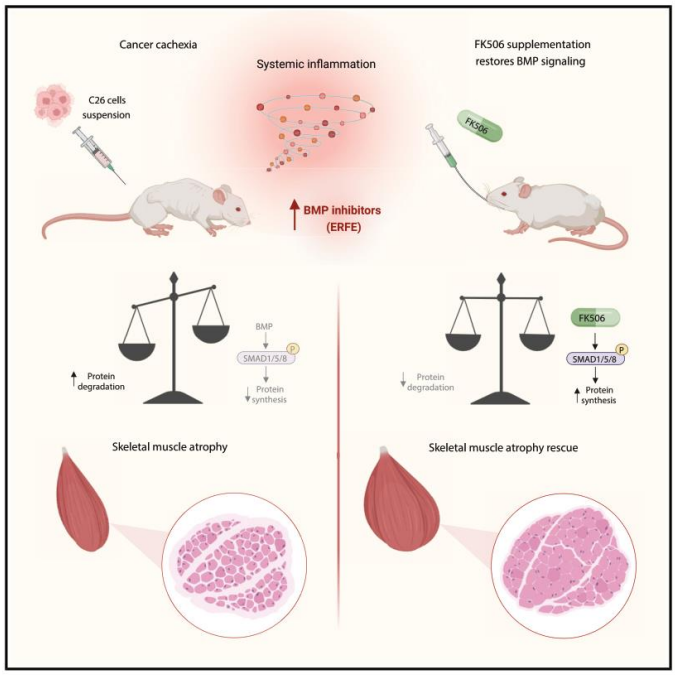

Authors

Erica Mina, Elisabeth Wyart, Roberta Sartori, ..., Léon Kautz, Laura Silvestri, Paolo E. Porporato

Correspondence

paolo.porporato@unito.it

In brief

Mina et al. explore the effects of FK506 treatment in skeletal muscle atrophy during cancer cachexia. This condition is characterized by reduced BMP signaling, leading to increased protein degradation and, therefore, muscle atrophy. FK506 re-activates this pathway rescuing protein synthesis, muscle force, and neuromuscular junction perturbations in cachexia.

Highlights

- The BMP-scavenger erythroferrone is upregulated in cachectic skeletal muscles
- The BMP signaling inhibitors erythroferrone and FKBP12 promote muscle atrophy
- FK506 activates BMP signaling by targeting FKBP12
- FK506 prevents muscle wasting and increases protein synthesis in cancer cachexia

Mina et al., 2023, Cell Reports Medicine *4*, 101306
December 19, 2023
https://doi.org/10.1016/j.xcrm.2023.101306

CellPress

FK506 bypasses the effect of erythroferrone in cancer cachexia skeletal muscle atrophy

Erica Mina[1], Elisabeth Wyart[1], Roberta Sartori[2,3], Elia Angelino[1,4], Ivan Zaggia[1], Valentina Rausch[1], Mara Maldotti[5,6], Alessia Pagani[7], Myriam Y. Hsu[1,8], Alberto Friziero[9,10], Cosimo Sperti[11], Alessio Menga[1], Andrea Graziani[1,4], Emilio Hirsch[1], Salvatore Oliviero[5,6], Marco Sandri[2,3], Laura Conti[1], Léon Kautz[12], Laura Silvestri[7,13], Paolo E. Porporato[1,14] *

[1] Department of Molecular Biotechnology and Health Sciences, Molecular Biotechnology Center "Guido Tarone", University of Torino, 10126 Torino, Italy.
[2] Department of Biomedical Sciences, University of Padova, Padova, Italy.
[3] VIMM: Veneto Institute of Molecular Medicine, Padova, Italy
[4] Department of Translational Medicine, University of Piemonte Orientale, 28100, Novara, Italy.
[5] Department of Life Sciences and Systems Biology, Molecular Biotechnology Center "Guido Tarone", University of Torino, 10126 Torino, Italy.
[6] Italian Institute for Genomic Medicine (IIGM), Sp142 Km 3.95, 10060, Candiolo, Torino, Italy.
[7] Division of Genetics and Cell Biology, IRCCS Ospedale San Raffaele, Milan, Italy.
[8] Division of Cell Fate Dynamics and Therapeutics, Department of Biosystems Science, Institute for Life and Medical Sciences (LiMe), Kyoto University, Kyoto, Japan.
[9] Department of Surgery, Oncology and Gastroenterology, University of Padova, Padova, Italy.
[10] General Surgery 1, Padova University Hospital, Padova, Italy
[11] General Surgery 2, Hepato-Pancreato-Biliary Surgery and Liver Transplantation Unit, Padova University Hospital, Padova, Italy.
[12] IRSD, Université de Toulouse, INSERM, INRAE, ENVT, Univ Toulouse III - Paul Sabatier (UPS), Toulouse, France.
[13] Vita Salute San Raffaele University, Milan, Italy.
[14] Lead Contact
* Correspondence: paolo.porporato@unito.it (P.E.P)

Summary

Skeletal muscle atrophy is a hallmark of cachexia, a wasting condition typical of chronic pathologies, that still represents an unmet medical need.

BMP-Smad1/5/8 signaling alterations are emerging drivers of muscle catabolism, hence, characterizing these perturbations is pivotal to develop therapeutical approaches.

We identified two promoters of *BMP-resistance* in cancer cachexia, specifically the BMP-scavenger erythroferrone (ERFE) and the intracellular inhibitor FKBP12. ERFE is upregulated in cachectic cancer patients' muscle biopsies, and in murine cachexia models, where its expression is driven by STAT3. Moreover, the knock-down of *Erfe* or *Fkbp12* reduces muscle wasting in cachectic mice. To bypass the BMP-resistance mediated by ERFE and release the brake on the signaling, we targeted FKBP12 with low-dose FK506. FK506 restores BMP-Smad1/5/8 signaling rescuing myotube atrophy by inducing protein synthesis. In cachectic tumor-bearing mice, FK506 prevents muscle and body weight loss and protects from neuromuscular junction alteration, suggesting therapeutical potential for targeting the ERFE-FKBP12 axis.

Keywords

cachexia, cancer cachexia, skeletal muscle atrophy, wasting, cancer, erythroferrone, FKBP12

Introduction

Cachexia is a progressive debilitating syndrome that can be associated to several systemic pathologies such as cancer and sepsis, and it is characterized by severe wasting of skeletal muscle and adipose tissue [1]. Cancer cachexia is correlated with worse prognosis and therapy responses, accounting for at least 30% of deaths in advanced cancer patients. Despite the high prevalence of this disease, the poor molecular understanding of the pathology makes cachexia still an unmet medical need [2]. The relevance of targeting skeletal muscle atrophy is supported by the fact that not only it is a predictor of poor clinical outcomes [3] and reduction of quality of life [4], but its prevention prolongs survival in cachectic tumor-bearing mice, independently from tumor growth, fat loss and inflammation [5].

Skeletal muscle atrophy is the result of unbalanced protein and organelles catabolism, coupled with reduced anabolic processes and metabolic rewiring. Indeed, mitochondrial dysfunction, zinc overload and iron deficiency have been associated with body weight loss in cachexia [6-8], with mitochondrial alterations preceding the onset of weight loss [9,10].

From a molecular standpoint, muscle mass maintenance is regulated by different signaling pathways that tune protein synthesis and degradation, notably TGFβ receptor superfamily [11-15], ubiquitin-proteasome axis [16-18], calcium-dependent proteolysis [19], and autophagy cascades [20].

Ligands as activins, myostatin or TGFβ, preferentially bind Activin receptors (ActRIIB, ActRIIA, TGFβRII and ALK- 4, -7, -5,) triggering Smad2/3 phosphorylation and inducing muscle atrophy and cachexia [21-25].

On the other hand, bone morphogenetic proteins (BMPs) are positive regulators of muscle mass, that by binding BMP receptors (BMPRII, ActRIIB, ActRIIA, and ALK1, ALK2, ALK3 and ALK6), activate biosynthetic pathways through Smad1/5/8 phosphorylation [12,13] and inhibit proteolysis by downregulating the expression of atrophy-associated E3 ubiquitin ligases (“atrogenes”) [11-13].

Moreover, BMP-Smad1/5/8 axis has also been shown to regulate neuromuscular junction (NMJ) formation and remodeling in models of Drosophila [26,27], and Noggin-mediated BMP inhibition induces skeletal muscle fibers denervation in cancer

cachexia [14].

The BMP signaling is a complex network that can be regulated at different levels. Since we previously reported that iron metabolism is dysregulated in cachexia [7], we explored the impact on skeletal muscle of different BMP inhibitors involved in the iron field. For instance, erythroferrone (ERFE) is an erythroid regulator of iron metabolism secreted in the circulation mainly by erythroid precursors [28], that scavenges BMP6 homodimers [29] and BMP6-BMP2 heterodimers [30] downregulating Smad1/5/8 phosphorylation in the liver [30,31]. Interestingly, ERFE was found to be also expressed in the skeletal muscle (named as myonectin [32]), but besides its extensively studied effects on the liver, its role on BMP signaling in the skeletal muscle has not been elucidated.

A further layer of BMP-Smad pathway regulation in the liver is represented by FKBP12 (FK506 binding protein 12) [33] [34], an immunophilin that limits and prevents the uncontrolled activation of BMP signaling [35], by binding the cytoplasmic domain of type I BMP receptors (BMPR-I) [36].

Given that BMP-Smad1/5/8 axis counteracts the catabolic TGFβ-Smad2/3 pathway in the skeletal muscle, we evaluated therefore the role of ERFE and FKBP12 in regulating muscle mass in wasting conditions.

In our study, we demonstrated that the main inflammatory pathway associated to cachexia (IL-6-STAT3 axis) upregulates the BMP signaling inhibitor *Erfe* in atrophic skeletal muscles, leading to a condition of "BMP-resistance" that can contribute to the catabolic effects of the hyper-active Activin/TGFβ-Smad2/3 signaling.

Furthermore, we propose a therapeutical approach to bypass ERFE-mediated BMP resistance by displacing the inhibitor FKBP12 from the BMP receptor with FK506 (tacrolimus), in models of cancer cachexia *in vitro* and *in vivo*.

Results

The BMP-scavenger erythroferrone (ERFE) is upregulated in cachexia through STAT3 activation.

BMP inhibitors such as Noggin [14] and myostatin [21] are upregulated both in mouse and human cancer cachexia [14,21]. The BMP-Smad1/5/8 axis in the liver is downregulated by scavengers like erythroferrone (ERFE), an erythroid regulator of iron metabolism [28] that, once secreted in the circulation, chelates BMP ligands [30,31]. However, whether this regulator plays a role not only in the liver [14] but also in muscle wasting and cancer cachexia is not known.

Mice carrying colon-26 (C26) adenocarcinoma developed severe cancer cachexia within 11 days and in their atrophic muscles phosphorylated Smad1/5/8 were downregulated as previously described [14] (Fig. 1a-c and Fig. S1a). Intriguingly, we found that C26 tumor-bearing mice upregulated the BMP-scavenger *Erfe* as mRNA levels (Fig. 1d) in their atrophic skeletal muscles, and as protein levels in the serum (Fig. 1e). While the reduction of the BMP-Smad1/5/8 axis is in line with increased levels of *Erfe*, we do not observe a decreased expression of BMP ligands, such as BMP2, BMP4 and BMP6 in the skeletal muscle of C26 tumor-bearing mice (Fig. S1b). We then analyzed the expression levels of *ERFE* in human samples from oncological patients. We found that *ERFE* expression is significantly higher in skeletal muscle biopsies from pre-cachectic (body-weight loss in 6 months, or <2% in patients with low muscle mass, or BMI<20) and cachectic (body-weight loss in 6 months, or >2% in patients with low muscle mass, or BMI<20) patients with colorectal or pancreatic cancer, than in cancer-free controls (Fig. 1f and Fig. S1c, d). In agreement, atrophic myotubes obtained by treating C2C12 with C26 conditioned medium (C26 CM), displayed significant higher transcripts levels of the BMP inhibitor *Erfe* (Fig. 1g and Fig. S1e).

To explore potential targets for BMP-signaling restoration, we analyzed in our models the expression levels of the immunophilin FKBP12 (FK506-binding protein 12) as it docks type I BMP receptors (BMPR-I) to limit their downstream signaling in the absence of ligands [35,36]. The mRNA levels of the intracellular inhibitor *Fkbp12*

were significantly upregulated in atrophic skeletal muscles of C26 tumor-bearing mice (Fig. S1f), accompanied by a trend in increased protein levels (Fig. S1g) and transcript in C2C12-derived atrophic myotubes (Fig. S1h).

Subsequently, we explored which molecular mechanism could trigger the transcriptional up-regulation of the BMP inhibitors *Erfe* and *Fkbp12* in cachexia by performing chromatin immunoprecipitation (ChIP-qPCR) assay on atrophic C2C12 myotubes treated with C26 CM and on cachectic skeletal muscles of C26 tumor-bearing mice (Fig. 1h). JASPAR TEFBS enrichment analysis [37] of *Erfe* and *Fkbp12* promoter sequences (+/-1000 bp from the transcription start site (TSS)), showed putative top-ranked predicted binding sites of STAT3 downstream *Erfe* TSS (+629/+639 bp) and upstream *Fkbp12* TSS (-491/-481) (Fig 1i and Fig. S1i). Indeed, the IL-6-STAT3 axis is a well-known trigger of muscle wasting in tumor-bearing mice [38-41]. In agreement, in C2C12 myotubes C26 CM, as well as IL-6, strongly induced phosphorylation of STAT3 at Tyr705 (pSTAT3) (Fig. S1j, k).

We therefore evaluated whether pSTAT3 could be involved in *Erfe* upregulation and *Fkbp12* expression in cachexia. We found that pSTAT3 significantly bound *Erfe* promoter in atrophic C2C12 myotubes treated with C26 CM (Fig. 1J and Fig. S1l). Furthermore, this promoter region was proven to be transcriptionally active because it carried the histone modification-H3K27ac, a known marker for chromatin accessibility [42] (Fig. S2a). In a similar way, pSTAT3 strongly bound *Erfe* promoter in atrophic muscles (Fig. 1k, Fig. S1m and Fig. S2b) indicating that activated STAT3 can be responsible for the upregulation of the BMP scavenger *Erfe* in cachexia.

Our ChIP-qPCR demonstrated that pSTAT3 can also bind the active *Fkbp12* promoter in atrophic myotubes (Fig. S2c, d) and in cachectic C26 muscles (Fig. S2e, f), suggesting that activated STAT3 is potentially involved in the regulation of BMP-signaling inhibitors.

Since ChIP-qPCR assay only provides information on the binding of transcription factors to specific sequences, we evaluated whether STAT3 is required for *Erfe* upregulation. By treating atrophic C2C12 myotubes with Stattic, an inhibitor of STAT3 phosphorylation and nuclear translocation [43], we blunted the upregulation of *Erfe* mediated by C26 CM (Fig. 1l and Fig. S2g). Moreover, to evaluate transcriptional

activation of the target gene, we generated a luciferase reporter under the control of the murine *Erfe* promoter.

As expected, the treatment with C26 CM or IL-6, that strongly induce pSTAT3, significantly triggers luciferase signal in transfected cells (Fig. S2h). Consistently, the increase of luciferase signal induced by C26 CM is blunted when cells are knocked down for STAT3 (Fig. 1m and Fig. S2i), further proving the crucial role of STAT3 in driving *Erfe* upregulation.

These results indicate that pSTAT3 not only binds *Erfe* promoter in cachexia, but its activation is required for *Erfe* upregulation.

Figure 1

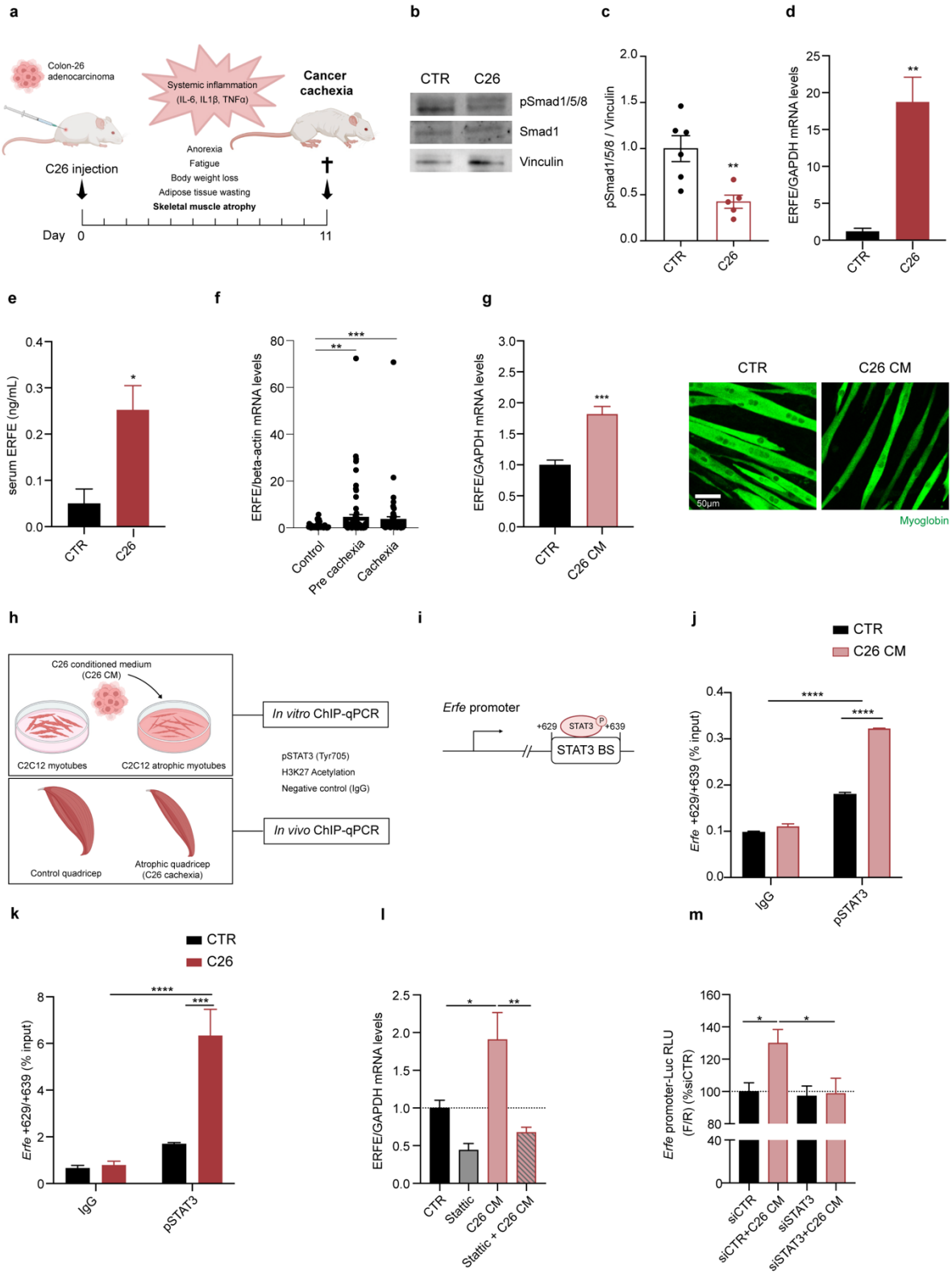
a
Colon-26 adenocarcinoma
Systemic inflammation (IL-6, IL1β, TNFα)
Cancer cachexia
C26 injection
Anorexia
Fatigue
Body weight loss
Adipose tissue wasting
Skeletal muscle atrophy
Day 0
11
b
CTR
C26
pSmad1/5/8
Smad1
Vinculin
c
pSmad1/5/8 / Vinculin
CTR
C26
d
ERFE/GAPDH mRNA levels
CTR
C26
e
serum ERFE (ng/mL)
CTR
C26
f
ERFE/beta-actin mRNA levels
Control
Pre cachexia
Cachexia
g
ERFE/GAPDH mRNA levels
CTR
C26 CM
CTR
C26 CM
50μm
Myoglobin
h
C26 conditioned medium (C26 CM)
C2C12 myotubes
C2C12 atrophic myotubes
In vitro ChIP-qPCR
pSTAT3 (Tyr705)
H3K27 Acetylation
Negative control (IgG)
Control quadricep
Atrophic quadricep (C26 cachexia)
In vivo ChIP-qPCR
i
Erfe promoter
+629
STAT3
+639
STAT3 BS
j
CTR
C26 CM
Erfe +629/+639 (% input)
IgG
pSTAT3
k
CTR
C26
Erfe +629/+639 (% input)
IgG
pSTAT3
l
ERFE/GAPDH mRNA levels
CTR
Stattic
C26 CM
Stattic + C26 CM
m
Erfe promoter-Luc RLU (F/R) (%siCTR)
siCTR
siCTR+C26 CM
siSTAT3
siSTAT3+C26 CM

Figure 1. The BMP-scavenger erythroferrone (ERFE) is upregulated in cachexia through STAT3 activation.

a) Schematic representation of the Colon-26 (C26) cancer cachexia model where mice injected with C26 cells develop severe cachexia within 11 days. **b)** Immunoblot of phosphorylated Smad1/5/8 (pSmad1/5/8) and vinculin in the quadriceps of control and C26 tumor-bearing mice. (n=5/6) **c)** Densiometric quantification of the immunoblot of pSmad1/5/8 and Smad1 in the quadriceps of control and C26 tumor-bearing mice. (n=5/6) **d)** mRNA levels of ERFE relative to GAPDH in the gastrocnemii of C26 tumor-bearing mice and relative control mice 11 days post cancer cells inoculation. (n=4/5) GAPDH, glyceraldehyde-3-phosphate dehydrogenase. **e)** ERFE protein concentration detected by ELISA in the serum of C26 and control mice. (n=4) **f)** Expression levels of ERFE relative to beta-actin in human skeletal muscle biopsies from pre-cachectic and cachectic colorectal and pancreatic cancer patients compared to control individuals (Control, n=41; pre-cachectic, n=77; cachectic, n=63). Values are reported as fold change over control group (Control vs pre-cachexia q value=0.0021; control vs cachexia q value=0.0007) **g)** Expression levels of *Erfe* in C2C12 myotubes treated for 48h with 20% C26 conditioned medium (C26 CM) (n=6) and representative immunofluorescence of atrophic C2C12 myotubes treated with C26 CM and stained for myoglobin. **h)** Experimental design of the chromatin immunoprecipitation-qPCR assay performed on C2C12 myotubes treated with C26 CM or atrophic skeletal muscles of C26 tumor-bearing mice at day 11. **i)** STAT3 predicted binding sites on *Erfe* promoter. **j)** ChIP-qPCR of pSTAT3 binding *Erfe* promoter on TSS (+629/+639 bp) in C2C12 myotubes treated with C26 CM compared to control cells. (n=2) **k)** *In vivo* ChIP-qPCR of pSTAT3 binding *Erfe* promoter on TSS (+629/+639 bp). ChIP-qPCR assay was performed by pooling 4 quadriceps per condition for control or C26 tumor-bearing mice. (n=2). **l)** Expression levels of *Erfe* on C2C12 myotubes treated with Stattic 5uM and/or 50% C26 CM for 6h (n=3). **m)** Luminescence (firefly/renilla) of NIH/3T3 transfected with *Erfe* promoter-Luc reporter vector and knocked-down for STAT3 (siSTAT3). Cells were treated overnight with 50% C26 CM prior to performing the assay. (n=2). See also Fig. S1 and S2.

Data information: Statistical significance was tested with unpaired two-tailed student's t-test in graphs c-e, g; with non-parametric Krustal-Wallis test followed by Benjamini, Krieger and Yekutieli multiple comparison test in graph f and with two ay ANOVA followed by Sidak's multiple comparison test in graphs j,k and with one-way ANOVA followed by Sidak's multiple comparison test in graphs l, m.

Supplementary Figure 1

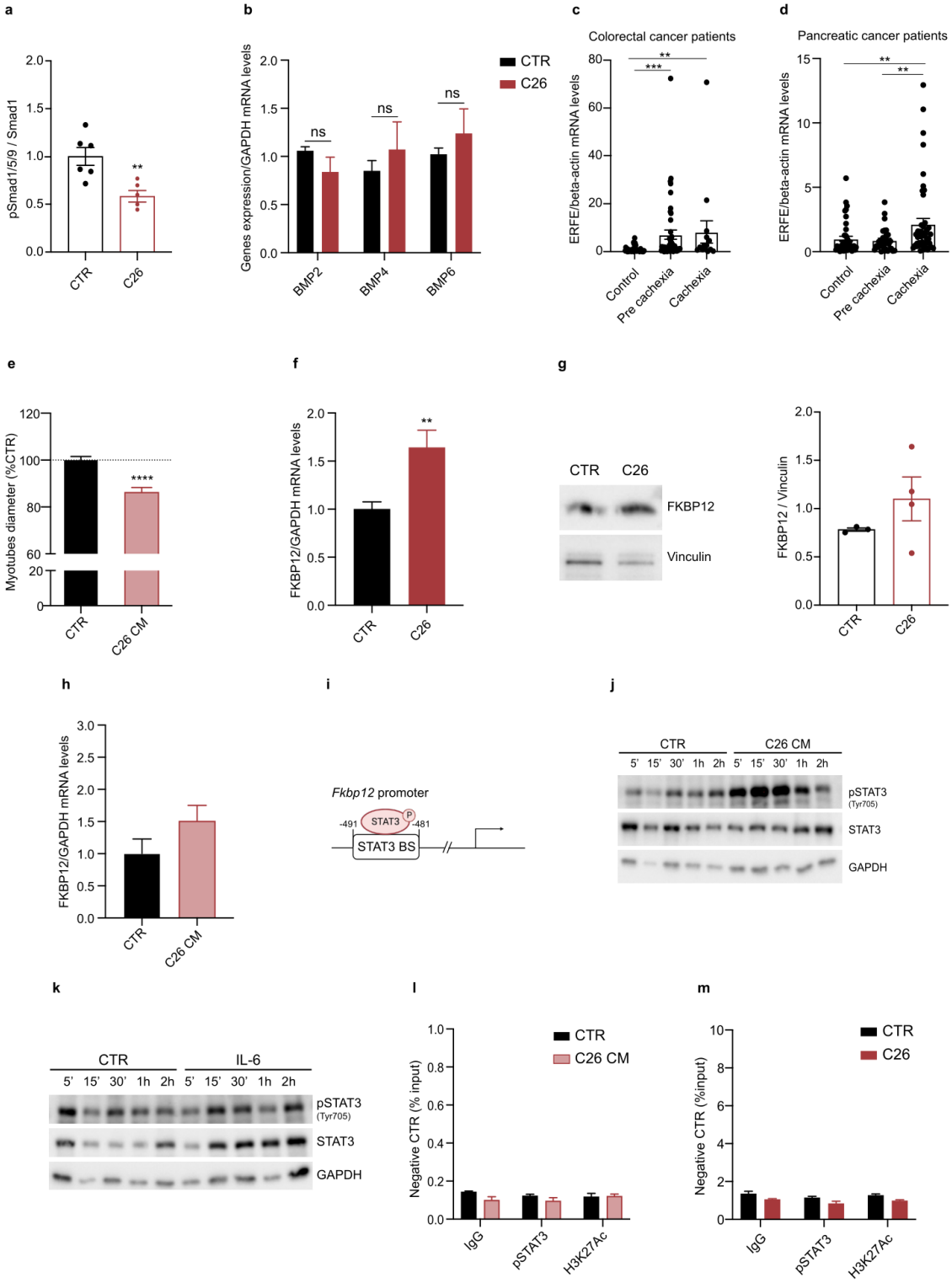

Figure S1: The BMP-scavenger erythroferrone (ERFE) is upregulated in cachexia through STAT3 activation. Related to Fig. 1.

a) Densiometric quantification of the immunoblot of pSmad1/5/8 and Smad1 in the quadriceps of control and C26 tumor-bearing mice. (n=5/6) **b)** Expression levels of BMP2 (n=4/5), BMP4 (n=4) and BMP6 (n=9), in the gastrocnemii of control and C26 tumor-bearing mice. **c)** Expression levels of *ERFE* relative to beta actin in human skeletal muscle biopsies from pre-cachectic and cachectic colorectal cancer patients compared to control individuals (Ctr, n=41; pre-cachectic, n=45; cachectic, n=15; control vs pre-cachexia q value=0.0001; control vs cachexia q value=0.0016). Values are reported as fold change over control group. **d)** Expression levels of *ERFE* relative to beta actin in human skeletal muscle biopsies from pre-cachectic and cachectic pancreatic cancer patients compared to control individuals (Ctr, n=41; pre-cachectic, n=32; cachectic, n=48; control vs cachexia q value=0.0022; pre-cachexia vs cachexia q value=0.0091;). Values are reported as fold change over control group**. e)** C2C12 myotubes diameter treated with 20% C26 CM for 24h. (n=5) **f)** mRNA levels of FKBP12 relative to GAPDH in the gastrocnemii of C26 tumor-bearing mice and relative control mice 11 days post cancer cells inoculation. (n=8) **g)** Immunoblot and densiometric quantification of FKBP12 in the quadriceps of control and C26 tumor-bearing mice. (n=3/4) **h)** Expression levels of FKBP12 in C2C12 myotubes treated for 48h with 20% C26 CM (n=6). **i)** Putative STAT3 binding site on *Fkbp12* promoter. **j-k)** Time course and immunoblot of phosphorylated STAT3 (Tyr705 – pSTAT3) and total STAT3 in C2C12 myotubes serum-starved for 2h and treated with pure C26 CM **(j)** (n=2) or IL-6 (100ng/mL) **(k)** or serum-free DMEM (CTR) at different timepoints. (n=2) **l-m)** ChIP-qPCR on a negative control region characterized by the absence of pSTAT3 and H3K27Ac in C2C12 myotubes treated with C26 CM (**l**) and *in vivo* skeletal muscles (**m**) compared to the control (each condition represents the pooling of 4 quadriceps). (n=2)

Data information: Statistical significance was tested with unpaired two-tailed student's t-test in graphs a, b, e-h; with Kruskal-Wallis test followed by Benjamini, Krieger and Yekutieli multiple comparison test in graphs c, d; with two-way ANOVA followed by Sidak's multiple comparison test in graphs l-m.

Supplementary Figure 2

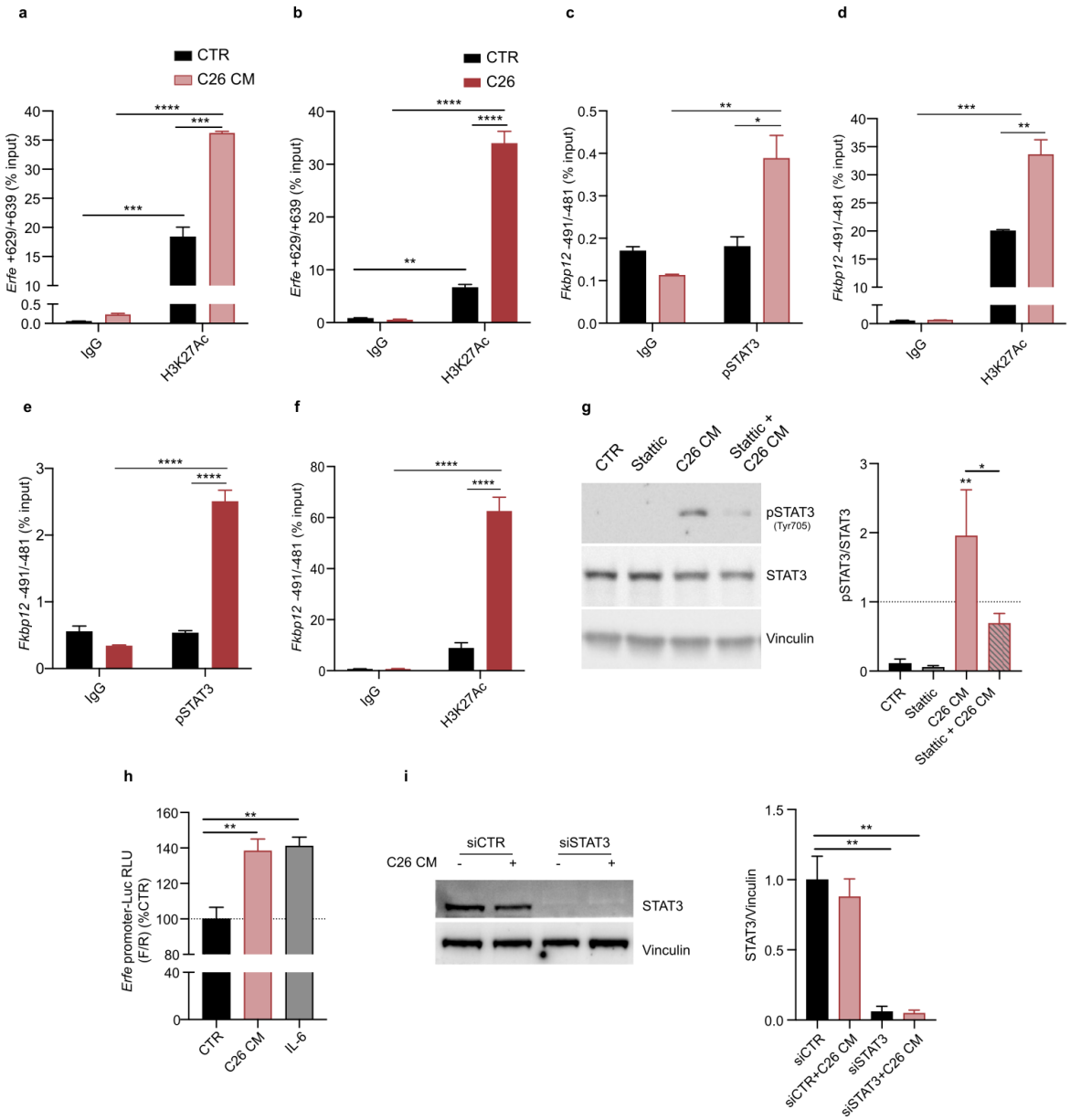

Figure S2: The BMP-scavenger erythroferrone (ERFE) is upregulated in cachexia through STAT3 activation. Related to Fig. 1.

a) ChIP-qPCR of acetylated H3K27 of *Erfe* promoter on TSS (+629/+639 bp) in C2C12 myotubes treated with C26 CM compared to control cells. (n=2) **b)** *In vivo* ChIP-qPCR of acetylated H3K27 of *Erfe* promoter on TSS (+629/+639 bp). ChIP-qPCR assay was performed by pooling 4 quadriceps per condition for control or C26 tumor-bearing mice. (n=2). **c-d)** *In vitro* ChIP-qPCR of pSTAT3 binding *Fkbp12* promoter on TSS (-491/-481) (**c**). The binding sites also carried an enrichment of the histone modification-H3K27ac as indication of open chromatin (**d**). ChIP-qPCR assay was performed on C2C12 myotubes serum-starved for 2h and treated for 30' with pure C26 CM. (n=2) **e-f)** *In vivo* ChIP-qPCR of pSTAT3 binding *Fkbp12* promoter on TSS (-491/-481) (**e**). The pSTAT3 binding sites also carried the histone modification-H3K27ac (**f**). ChIP-qPCR assay was performed by pooling 4 quadriceps per condition for control or C26 tumor-bearing mice. (n=2) **g)** Representative immunoblot of pSTAT3 (Tyr705) and relative densitometric quantification of C2C12 myotubes treated with Stattic 5uM and/or pure C26 CM for 30', previously serum-starved for 2h. (n=3) **h)** Luminescence signal (firefly/renilla) of NIH/3T3 cells transfected with *Erfe* promoter-Luc reporter vector and treated with 50% C26 CM or IL-6 (100ng/mL) overnight (n=4/6). **i)** Representative STAT3 immunoblot and relative densitometric quantification of NIH/3T3 cells transfected as in Fig. 1m (n=2).

Data information: Statistical significance was tested with unpaired two-tailed student's t-test in graph h; with two-way ANOVA followed by Sidak's multiple comparison test in graphs a-f, and with one-way ANOVA followed by Sidak's multiple comparison test in graph g, i.

Muscle-specific knockdown of BMP inhibitors curbs muscle wasting in C26 tumor-bearing mice.

To understand the biological role of the BMP-signaling inhibitors ERFE and FKBP12 in cachexia (Fig. 2a), we treated C2C12-derived myotubes with recombinant ERFE, using the truncated-inactive form (gERFE) as a negative control. ERFE was sufficient to induce atrophy *in vitro* (Fig. 2b and Fig. S3a), while gERFE did not, thus suggesting that the functional N-terminal domain, known to downregulate the BMP-SMAD signaling in the liver [44], is biologically active in the skeletal muscle.

While the supplementation of the extracellular inhibitor ERFE induced myotube atrophy, the downregulation of the intracellular inhibitor *Fkbp12* by siRNA was sufficient to rescue C26 CM-induced myotube atrophy (Fig. 2c, d and Fig. S3b).

We next explored *in vivo* whether ERFE or FKBP12 downregulation was sufficient to protect from muscle wasting in cachectic C26 tumor-bearing mice. We delivered adeno-associated viral particles with muscle tropism (AAV9) carrying short-hairpin RNA targeting either *Erfe* (AAV9-sh*Erfe*) or *Fkbp12* (AAV9-sh*Fkbp12*) in one hindlimb of BALB/c mice and control viral particles (AAV9-shScramble carrying a scrambled sequence) in the contralateral limb. After inducing cachexia by injecting C26 cancer cells (Fig. 2e), we found that *Erfe* knockdown (Fig. 2f) in the quadricep was sufficient to reduce the weight loss detected in their contralateral muscle (Fig. 2g) and this was accompanied by decreased Atrogin1 expression, a marker of the atrophic process (Fig. 2h). These muscles also presented increased cross-sectional areas (Fig. 2i), indicating that ERFE downregulation in the muscle is sufficient to curb the wasting process.

Following the same approach, we evaluated whether muscle-specific FKBP12 knockdown had a similar effect of AAV9-sh*Erfe* on muscle atrophy in C26-tumor bearing mice. *Fkbp12* downregulation (Fig. 2j) potently increased quadriceps weight and significantly mitigated Atrogin1 levels in C26 tumor-bearing mice (Fig. 2k, l), as well as displayed higher number of bigger fibers (Fig. 2m) with respect to their contralateral limbs. Therefore, these results encouraged us to test whether FKBP12 can represent a valuable therapeutic target, restoring BMP-signaling and counteracting cachexia.

Figure 2

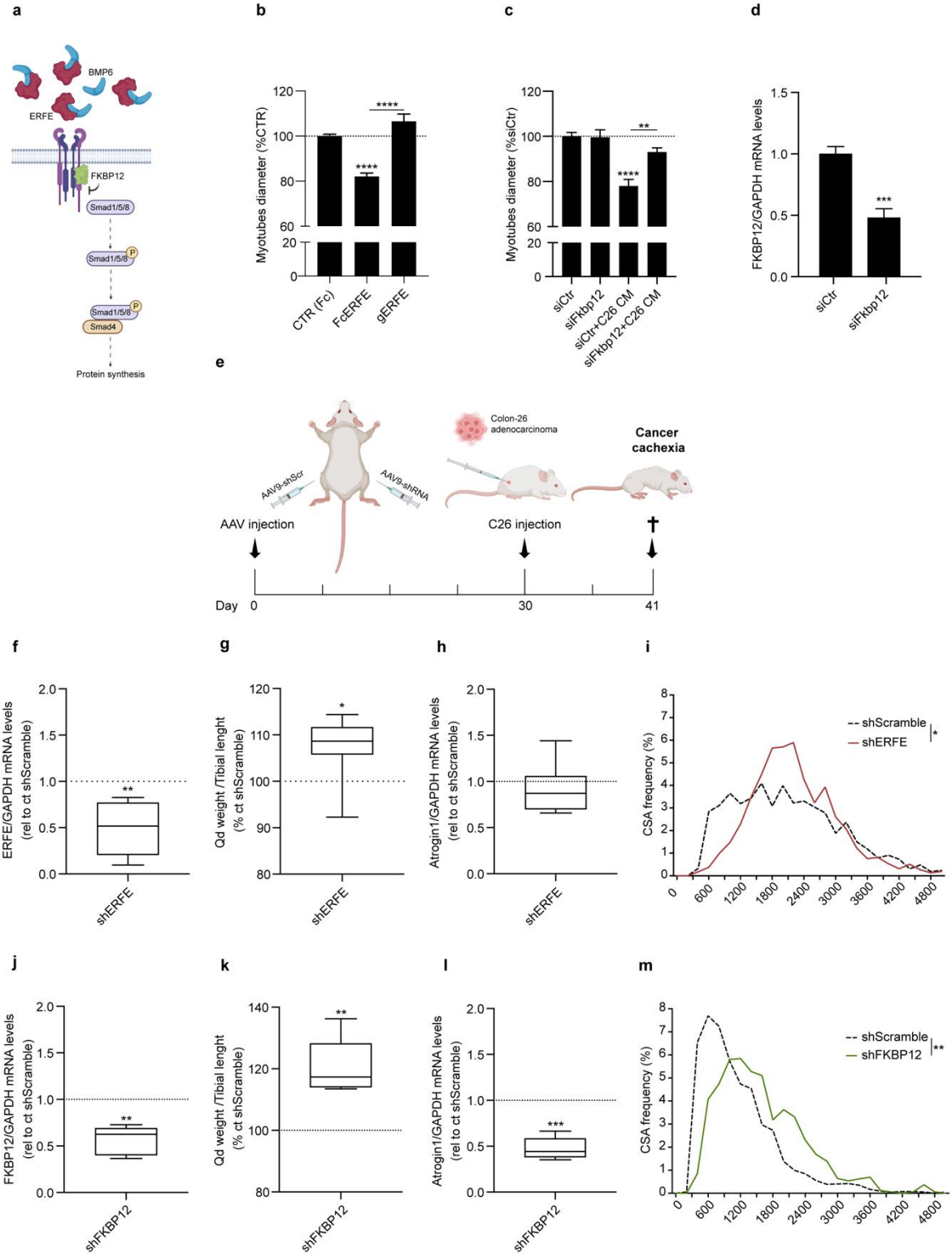
a
BMP6
ERFE
FKBP12
Smad1/5/8
Smad1/5/8
Smad1/5/8
Smad4
Protein synthesis
b
Myotubes diameter (%CTR)
CTR (Fc)
FcERFE
gERFE
c
Myotubes diameter (%siCtr)
siCtr
siFkbp12
siCtr+C26 CM
siFkbp12+C26 CM
d
FKBP12/GAPDH mRNA levels
siCtr
siFkbp12
e
AAV9-shScr
AAV9-shRNA
Colon-26 adenocarcinoma
Cancer cachexia
AAV injection
C26 injection
Day 0
30
41
f
ERFE/GAPDH mRNA levels (rel to ct shScramble)
shERFE
g
Qd weight /Tibial lenght (% ct shScramble)
shERFE
h
Atrogin1/GAPDH mRNA levels (rel to ct shScramble)
shERFE
i
CSA frequency (%)
shScramble
shERFE
j
FKBP12/GAPDH mRNA levels (rel to ct shScramble)
shFKBP12
k
Qd weight /Tibial lenght (% ct shScramble)
shFKBP12
l
Atrogin1/GAPDH mRNA levels (rel to ct shScramble)
shFKBP12
m
CSA frequency (%)
shScramble
shFKBP12

Figure 2. Muscle-specific knockdown of BMP inhibitors curbs muscle wasting in C26 tumor-bearing mice.

a) Schematic representation of the pathway. The BMP-scavenger ERFE is upregulated in cachexia and with the intracellular inhibitor FKBP12 contributes to the downregulation of pSmad1/5/8 in atrophic muscles. **b)** Quantification of myotubes diameters after 24h treatment with recombinant Fc-ERFE (1ug/mL), inactive globular Fc-gERFE (1ug/mL) and the relative Fc-CTR (1ug/mL). (n=3/4) **c)** Myotubes diameters transfected with siRNA for *Fkbp12* or scramble sequence (siCtr) for 48h and treated for 24h with 10% C26 CM. (n=3/4) **d)** Expression levels in C2C12 myotubes knocked-down for FKBP12 with siRNA. (n=4/6) **e)** Experimental design of muscle-specific AAV9 delivery in the skeletal muscle of C26 tumor-bearing mice. AAV9-shRNA (10^{11} vp) viral particles were injected in the skeletal muscles of BALB/c mice, using the contralateral limb as control (AAV9-shScr). One month after AAV injection, BALB/c mice were subcutaneously inoculated with 750.000 C26 cancer cells. The mice were euthanized 11 days after C26 injection. **f)** mRNA levels of ERFE in the quadriceps of AAV9-shERFE-injected mice, versus the contralateral AAV9-shScr limb. (n=7) **g)** Quadriceps weight normalized for tibial length compared to the contralateral limb. (n=7) **h)** Atrogin1 expression in the quadriceps analyzed in Fig. 2f, g. (n=7) **i)** Cross-sectional fiber area distribution of AAV9-shERFE-injected mice. (n=3) **j)** mRNA levels of FKBP12 in the quadriceps of AAV9-shFKBP12-injected mice, versus the contralateral AAV9-shScramble limb. (n=7) **k)** Quadriceps weight normalized for tibial length compared to the contralateral limb. (n=7) **l)** Atrogin1 expression in the quadriceps analyzed in Fig.2j, k. **m)** Cross-sectional fiber area distribution of AAV9-shFKBP12-injected mice. (n=3) See also Fig. S3.

Data information: Statistical significance was tested with unpaired two-tailed student's t-test in graph d; with one-way ANOVA followed by Sidak's multiple comparison test in graph b, c. One sample t-test was performed in graphs f-h and j-l, while two-way ANOVA followed by Sidak's multiple comparison test in graphs i and m.

Supplementary Figure 3

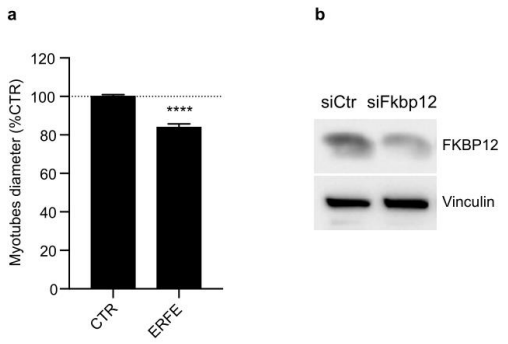

Figure S3: Muscle-specific knockdown of BMP inhibitors curbs muscle wasting in C26 tumor-bearing mice. Related to Fig. 2.

a) Quantification of C2C12 myotubes treated with murine recombinant ERFE (1ug/mL) for 24h. (n=5/7) **b)** Immunoblotting for *Fkbp12* knock-down in myotubes transfected with siRNA for *Fkbp12* or scramble sequence (siCtr) for 48h (n=2).

Data information: Statistical significance was tested with unpaired two-tailed student's t-test in graph a.

FK506 bypasses BMP-pathway inhibition by activating pSmad1/5/8 through FKBP12 binding.

Since *Fkbp12* knockdown protected from C26 cancer cells-induced muscle atrophy (Fig. 2c, j-m) and that BMP-signaling is decreased in cancer-related skeletal muscle atrophy [14] (Fig. 1b), we decided to bypass the inhibition of the BMP signaling using a pharmacological approach (Fig. 3a). Tacrolimus (FK506) is a drug clinically used as immunosuppressant that complexes with FKBP12 to inhibit calcineurin, thereby suppressing T cell proliferation [45,46]. Nevertheless, a non-immunosuppressive low-dose of FK506 increased BMP-Smad1/5/8 signaling in hepatocytes [34] and in mouse models of chronic kidney, cardiac and liver disease[47].

Therefore, we treated C2C12 myotubes with FK506 to assess its effect upon atrophic stimuli. FK506 treatment induced significant hypertrophy in myotubes and completely prevented the atrophy induced by C26 CM (Fig. 3b) and recombinant ERFE (Fig. 3c and Fig. S4a). Moreover, FK506 rescued the atrophy induced by Activin A (ACTA) (Fig. S4b), a TGFβ-receptor ligand that drives skeletal muscle atrophy in cachexia [23].

Next, we investigated whether the effect of FK506 on myotubes was due to its well-known activity on calcineurin activation. To this aim, we used cyclosporine A (CyA), another immunosuppressant drug which inhibits calcineurin in an FKBP12 independent manner [48]. C2C12 myotubes treated with cyclosporine A undergo atrophy (Fig. S4c), suggesting that FK506 effect on myotubes was independent of calcineurin inhibition.

In line with the increased myotube size in FK506-treated C2C12, FK506 alone strongly induced phosphorylation of Smad1/5 (Fig. 3d) and synergized with murine BMP6 (Fig. 3e and Fig. S4d). By performing BMP-Responsive Element (BRE)-Luciferase Reporter assay in C2C12, we confirmed that in cells treated with FK506 the luciferase signal was significantly higher than in controls (Fig. 3f). This transcriptional upregulation was synergic with concomitant administration of BMP6, in line with increased phosphorylation of Smad1/5 (Fig. 3e). These results

demonstrated that the increased levels of pSmad1/5 were functionally active to target gene expression.

As FKBP12 blocks uncontrolled activation of the BMP pathway by binding BMPR type I (BMPR-I) [49,50], we investigated which receptor accounted for BMP activation followed by FK506 treatment. We knocked-down with siRNA in C2C12 myotubes either ALK2 or ALK3, two BMPR-I family members expressed in skeletal muscle, and only ALK2 downregulation reduced pSmad1/5 triggered by FK506 (Fig. 3g, h). The relevance of ALK2 is furthermore proven when C2C12 myotubes were treated with Dorsomorphin Homolog 1 (DMH1), a BMPR-I inhibitor that primarily inhibits ALK2 [51]. The inhibition of Smad1/5 phosphorylation (Fig. S4e) by DMH1 supplementation was sufficient to hinder the rescue of C26 CM-induced atrophy by FK506 (Fig. 3i).

FK506 could activate the BMP-Smad axis by binding and displacing the intracellular inhibitor FKBP12 from BMPR-I family members [33,52]. To assess whether FKBP12 could interact with ALK2 or ALK3, we co-transfected HuH7 and 293T cells with MYC-tagged ALK2 or MYC-tagged ALK3 constructs with FLAG-tagged FKBP12 (Fig. S4f, g). In HuH7 cells the interaction of FKBP12-FLAG is limited to ALK2 (Fig. S3f) [33], however FKBP12-FLAG overexpression in 293T cells shows a minimal binding of FKBP12 to ALK3 (Fig. S4g). In both cases FK506 displaced FKBP12 from any BMPR-I analyzed (Fig. S4f, g).

As the activation of the BMP-Smad1/5/8 axis has been associated to increased protein synthesis [12,53], we performed a SuNSET assay to measure protein synthesis in our *in vitro* model of myotube atrophy. As expected, C2C12 treated C26 CM (Fig. 3j and Fig. S4i), recombinant ERFE (Fig. 3k and Fig. S4j) or Activin A (Fig. S4h, k) and co-treated with FK506, showed significant higher levels of newly synthetized proteins (Fig. 3j, k and Fig. S4h-k), in line with C2C12 myotubes diameters (Fig. 3b, c and Fig. S4b).

Moreover, mTOR inhibition by Torin 1 abolished the hypertrophy induced by FK506 (Fig. 3l), demonstrating that the increase in myotube size is due to increased protein synthesis and it is mediated by mTOR. Coherently with these findings, we found that the atrophic markers Atrogin1 and MuRF1 were decreased in C26 CM-treated myotubes supplemented with FK506 (Fig. 3m, n).

Overall, these results demonstrated that *in vitro,* FK506 rescues myotube atrophy by inducing FKBP12 displacement from ALK2, increasing Smad1/5/8 signaling, ultimately leading to increased protein synthesis and reduced atrogenes levels.

Figure 3

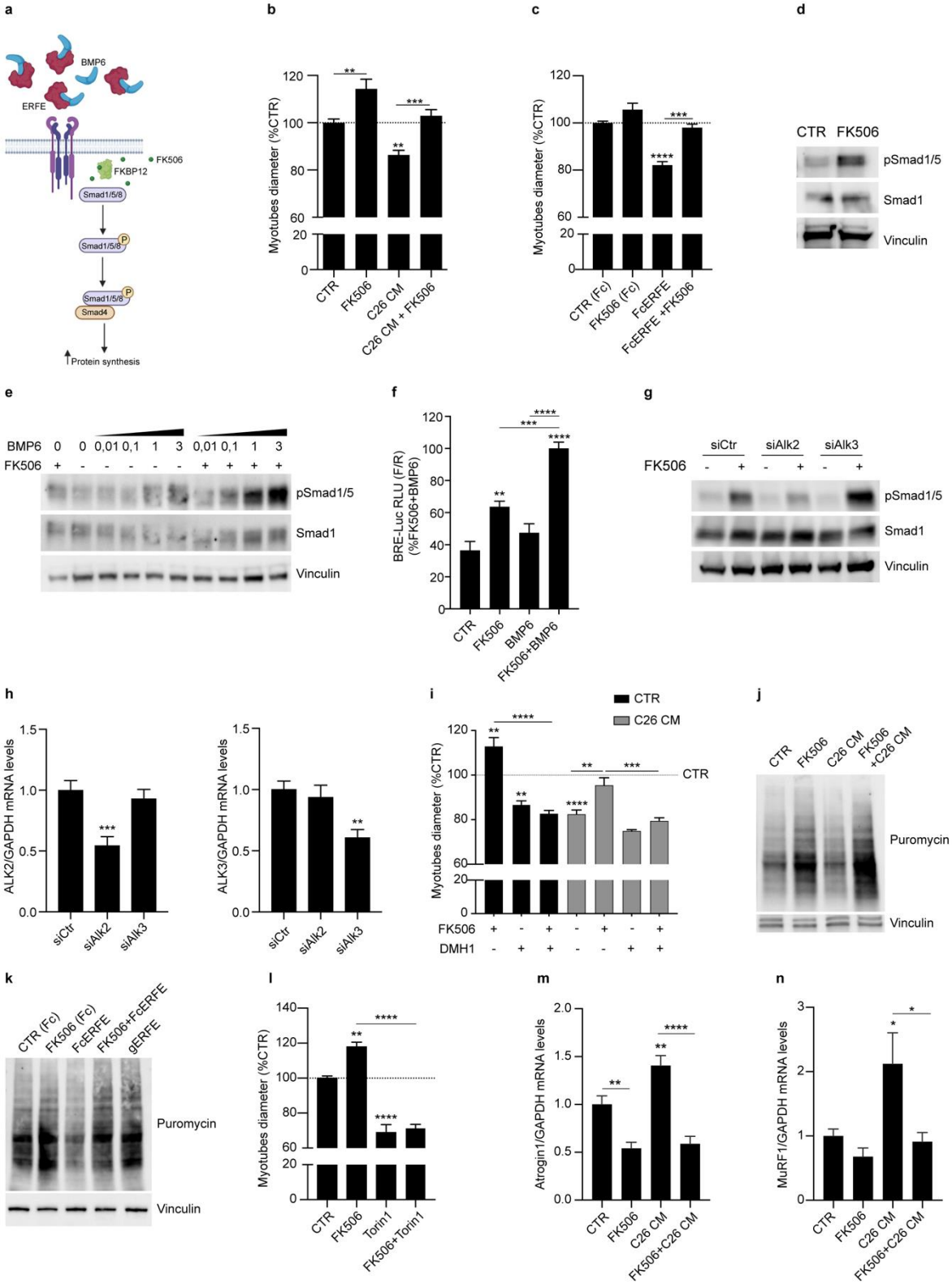
a
BMP6
ERFE
FK506
FKBP12
Smad1/5/8
Smad1/5/8
Smad1/5/8
Smad4
Protein synthesis
b
Myotubes diameter (%CTR)
CTR
FK506
C26 CM
C26 CM + FK506
c
Myotubes diameter (%CTR)
CTR (Fc)
FK506 (Fc)
FcERFE
FcERFE +FK506
d
CTR FK506
pSmad1/5
Smad1
Vinculin
e
BMP6 0 0 0,01 0,1 1 3 0,01 0,1 1 3
FK506 + - - - - - + + + +
pSmad1/5
Smad1
Vinculin
f
BRE-Luc RLU (F/R) (%FK506+BMP6)
CTR
FK506
BMP6
FK506+BMP6
g
siCtr siAlk2 siAlk3
FK506 - + - + - +
pSmad1/5
Smad1
Vinculin
h
ALK2/GAPDH mRNA levels
siCtr
siAlk2
siAlk3
ALK3/GAPDH mRNA levels
siCtr
siAlk2
siAlk3
i
CTR
C26 CM
Myotubes diameter (%CTR)
CTR
FK506 + - + - + - +
DMH1 - + + - - + +
j
CTR
FK506
C26 CM
FK506 +C26 CM
Puromycin
Vinculin
k
CTR (Fc)
FK506 (Fc)
FcERFE
FK506+FcERFE
gERFE
Puromycin
Vinculin
l
Myotubes diameter (%CTR)
CTR
FK506
Torin1
FK506+Torin1
m
Atrogin1/GAPDH mRNA levels
CTR
FK506
C26 CM
FK506+C26 CM
n
MuRF1/GAPDH mRNA levels
CTR
FK506
C26 CM
FK506+C26 CM

Figure 3. FK506 bypasses BMP-pathway inhibition by activating pSmad1/5/8 through FKBP12 binding.

a) Representation of the proposed approach to bypass the "BMP-resistance". FK506 binds FKBP12 displacing it from the type I BMP receptor (BMPR-I) and restoring pSmad1/5/8 signaling. **b-c)** Diameters quantification of C2C12 myotubes treated for 24h with FK506 (1ug/mL) and/or 10% C26 CM (**b**) (n=5); or treated with recombinant Fc-ERFE (1ug/mL) and FK506 in Fc-CTR (1ug/mL) (**c**). (n=4) **d)** Immunoblot of C2C12 myotubes serum starved for 2h and treated with FK506 (1ug/mL) for 1h. (n=4) **e)** Dose response and immunoblot of pSmad1/5/8 in C2C12 myotubes serum-starved for 2h and treated with increasing doses of murine BMP6 (from 0,01 to 3 ng/mL) with or without FK506 (1ug/mL) for 1h. (n=4) **f)** Luminescence signal detected in C2C12 transfected with pGL3-BMP responsive element (BRE)-Luciferase and TK-Renilla for 24h, switched to low-serum DMEM 2%FBS for 4h and treated with FK506 (10ug/mL) and BMP6 (30ng/mL) for 5h. (n=6) **g)** Immunoblot of pSmad1/5 and Smad1 of C2C12 myotubes knocked-down for ALK2 or ALK3 (siAlk2 or siAlk3) for 48h and treated with FK506 (1ug/mL) for 1h upon 2h of serum starvation. (n=2) **h)** mRNA levels of ALK2 and ALK3 in C2C12 myotubes knocked-down for ALK2 or ALK3 with siRNA. (n=2/3) **i)** Diameters of C2C12 myotubes treated with DMH1 (500nM) in combination with FK506 (1ug/mL) and/or 10% C26 CM for 24h in differentiation medium. (n=3/4) **j-k)** *In vitro* SuNSET assay and relative quantifications performed with C2C12 myotubes treated with FK506 (1ug/mL), 10% C26 CM (**j**) (n=4); or Fc-CTR (1ug/mL), Fc-ERFE (1ug/mL) and inactive globular gERFE (1ug/mL) (**k**) (n=3) for 24h in differentiation medium. For the last 4h of treatment, puromycin (1uM) was added to the cells. **l)** Myotubes diameters imaged at 24h post FK506 (1ug/mL) and/or Torin1 (100uM) treatment. (n=3) **m-n)** mRNA levels of Atrogin1 (**m**) (n=3/5) and MuRF1 (**n**) (n=3) in C2C12 myotubes treated f
or 48h with FK506 (1ug/mL) and/or 20% C26 CM. See also Fig. S4.

Data information: All graphs' statistical significance was tested with one-way ANOVA followed by Sidak's multiple comparison test.

Supplementary Figure 4

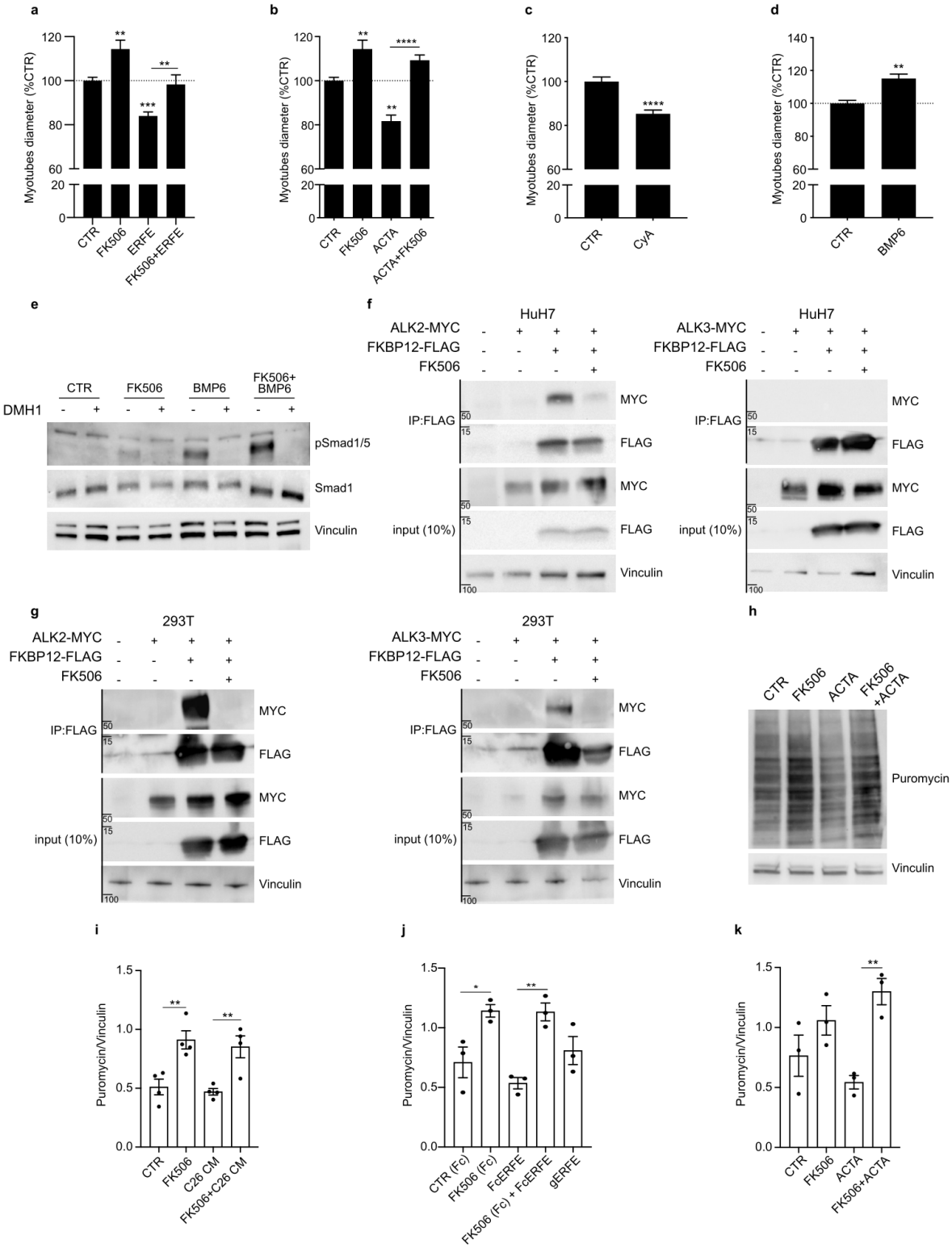

Figure S4: FK506 bypasses BMP-pathway inhibition by activating pSmad1/5/8 through FKBP12 binding. Related to Fig. 3.

a-d) Myotubes diameters quantified at 24h after treatment with FK506 (1ug/mL), ERFE (1ug/mL) (**a**), Activin A (ACTA) (1ng/mL) (**b**), cyclosporine A (CyA) (1uM) (**c**), or BMP6 (1ng/mL) (**d**) in differentiation medium. (n=3/5) **e)** Immunoblot for pSmad1/5/8 and Smad1 of C2C12 myotubes serum-starved for 2h and treated with FK506 (1ug/mL), BMP6 (30ng/mL) with or without DMH1 (500nM) for 1h in serum-free DMEM. (n=3) **f-g)** HuH7 (**f**) and HEK-293T (**g**) cells were transfected with FKBP12-FLAG and ALK2-MYC or ALK3-MYC constructs for 48h. Afterwards, cells were switched to low serum medium (DMEM 2%FBS) for 3h and treated for 1h with FK506 (10ug/mL for HEK-293T and 1ug/mL for HuH7). Protein lysates were then immunoprecipitated using FLAG-tagged resin and immunoblotting was performed to detect the interaction between FKBP12 and ALK2 or ALK3. (n=4) **h)** *In vitro* SuNSET assay performed in C2C12 myotubes treated with FK506 (1ug/mL) and Activin A (ACTA) (1ng/mL) for 24h in differentiation medium. For the last 4h of treatment, puromycin (1uM) was added to the cells. (n=3) **i-k)** Densiometric quantifications of *in vitro* SuNSET assays performed in C2C12 myotubes treated with FK506, C26 CM (**i**), FcERFE (**j**) or ACTA (**k**). (n=3/4)

Data information: Statistical significance was tested with one-way ANOVA followed by Sidak's multiple comparison test in graph a, b, i-k; with unpaired two-tailed student's t-test in graphs c, d.

FK506 effect on the immune system *in vivo*.

To address the effect of FK506 in an *in vivo* cancer cachexia model, BALB/c mice were injected with colon-26 (C26) adenocarcinoma cells, and daily treated for 11 days (Fig. 4a) with an oral low-dose of FK506 (0.02 mg/kg) known to be non-immunosuppressive [47]. First, we verified whether the chosen dose of FK506 was altering the immune landscape and consequently the tumor size: after 11 days of treatment, tumor (Fig. 4b) and spleen weights (Fig. S5a) were unchanged, indicating that our treatment with FK506 does not exert an antitumoral as well as an anti-inflammatory effect [54].

In addition, we performed an analysis of immune cell populations in tumors, blood, and spleens of treated and control mice. No significant differences were found, as the amount of the main lymphoid and myeloid populations, such as NK, NKT, CD4+ and CD8+ T cells, DC, macrophages, m-MDSC and g-MDSC, was similar in the tumors from control and FK506-treated mice (Fig. 4c, d). Moreover, FK506 treatment did not alter the expression of PD-1 on T lymphocytes (Fig. 4e) or that of PD-L1 on myeloid cells (Fig. 4f). As expected, tumor-bearing mice showed significant decrease of blood and splenic CD4+ and CD8+ T cells (Fig. 4g and Fig. S5b), increased splenic macrophages (Fig. S5c), as well as increased g-MDSC/neutrophils populations in the blood (Fig. 4h), independently of treatment with FK506. Furthermore, C26 tumor bearing mice displayed a significant decrease of PD-L1-positive macrophages and g-MDSC in the blood (Fig. 4i), and an increase of PD-1-expressing CD4+ and CD8+ T cells and of PD-L1+ mMDSC in the spleen (Fig. S5d, e), again regardless of FK506 administration.

Despite FK506 decreased PD-1-expressing CD4+ and CD8+ T cells in the blood of control mice, these alterations were not observed in C26-tumor bearing mice (Fig. 4j), suggesting that FK506 does not affect tumor immune escape. Nonetheless, we sought to further exclude whether chronic low-dose FK506 treatment could disturb adaptive immune responses in a tumor-free mice. We thus vaccinated with a non-self antigen (RhuT vaccine) [55] to induce a strong immune response. All mice were treated for 5 weeks with daily oral gavage of low-dose FK506 or vehicle until the end of the experiment (Fig. S5f). To test if FK506 affected specific lymphocyte functions

and activities, we evaluated whether long-term FK506 treatment modified antibody production or immune cell cytotoxic capacity. After 5 weeks of treatment, antibody titers against the antigen (Fig. S5g) as well as activation of CD8+ T cells (Fig. S5h) were not different in either F506-treated or untreated vaccinated mice. In agreement, this long chronic treatment with FK506 did not significantly alter the amount of blood lymphoid populations and the expression of the activation marker PD-1 (Fig. S5i, j).

These findings indicated that prolonged low-dose FK506 treatment does not significantly alter the amount and function of immune cells in a tumor-free mouse model, corroborating that low-dose FK506 does not impact adaptive immunity.

Figure 4

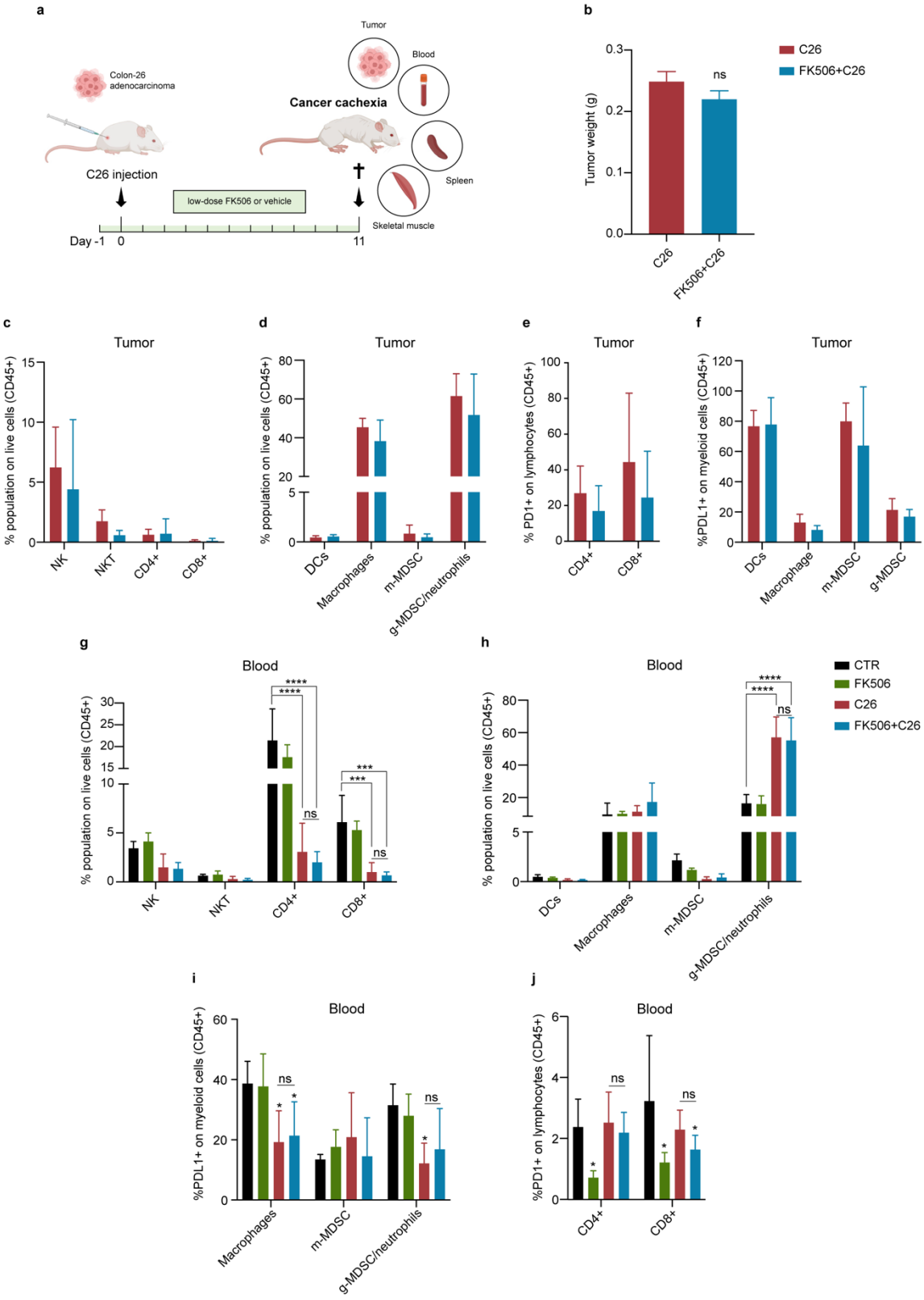
a
Tumor
Blood
Colon-26 adenocarcinoma
Cancer cachexia
Spleen
C26 injection
low-dose FK506 or vehicle
Skeletal muscle
Day -1
0
11
b
C26
FK506+C26
Tumor weight (g)
ns
c
Tumor
% population on live cells (CD45+)
NK
NKT
CD4+
CD8+
d
Tumor
% population on live cells (CD45+)
DCs
Macrophages
m-MDSC
g-MDSC/neutrophils
e
Tumor
% PD1+ on lymphocytes (CD45+)
CD4+
CD8+
f
Tumor
%PDL1+ on myeloid cells (CD45+)
DCs
Macrophage
m-MDSC
g-MDSC
g
Blood
% population on live cells (CD45+)
NK
NKT
CD4+
CD8+
h
Blood
% population on live cells (CD45+)
DCs
Macrophages
m-MDSC
g-MDSC/neutrophils
CTR
FK506
C26
FK506+C26
i
Blood
%PDL1+ on myeloid cells (CD45+)
Macrophages
m-MDSC
g-MDSC/neutrophils
j
Blood
%PD1+ on lymphocytes (CD45+)
CD4+
CD8+

Figure 4. FK506 effect on the immune system in vivo.

a) Experimental design of the *in vivo* C26 cancer cachexia model orally treated with low-dose FK506 (0,02mg/Kg) or vehicle for 11 days. When euthanized, tumors, blood, spleens, and skeletal muscles were analyzed. **b)** Tumor weight of FK506-treated and vehicle-treated C26 tumor-bearing mice 11 days post-C26 injection. (n=16) **c-d)** Percentages of lymphoid (**c**) and myeloid (**d**) populations on live cells (CD45+) in the tumors of FK506 or vehicle-treated C26 tumor-bearing mice. (n=6) **e-f)** Percentage of PD-1-expressing lymphocytes (**e**) and PD-L1+ myeloid cells (**f**) in C26 tumors of FK506 and vehicle-treated mice. (n=6) **g-h)** Amount of blood lymphoid (**g**) and myeloid (**h**) populations in FK506 and vehicle-treated tumor and non-tumor-bearing mice at day 11 post-C26 injection. (n=4/6) **i-j)** Percentage of PD-L1+ myeloid cells (**i**) and PD-1+ lymphocytes (**j**) in the blood of the experimental groups 11 days post-C26 inoculation. (n=4/6) See also Fig. S5.

Data information: Statistical significance was tested with unpaired two-tailed student's t-test in graph b; with two-way ANOVA followed by Sidak's multiple comparison test in graphs c-j.

Supplementary Figure 5

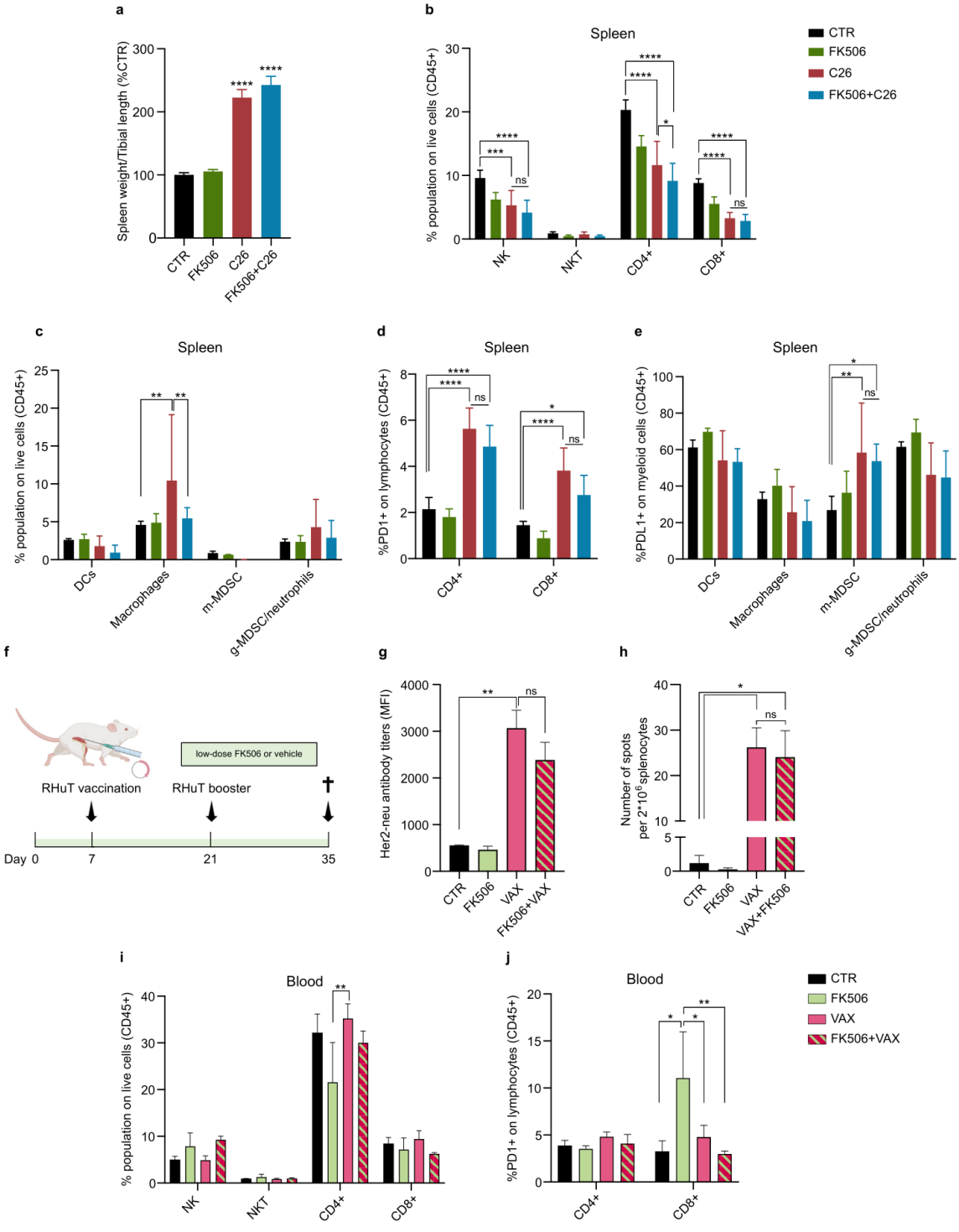

Figure S5: FK506 effect on the immune system in vivo. Related to Fig. 4.

a) Spleen weights normalized for tibial length in C26 tumor-bearing mice treated with FK506 and relative control groups. (n=11) **b-c)** Percentages of lymphoid (**b**) and myeloid (**c**) populations in the spleen of tumor and non-tumor bearing mice, treated or not with FK506. (n=4/6) **d-e)** Percentages of PD-1+ lymphocytes (**d**) and PD-L1+ myelocytes (**e**) in the spleens. (n=4/6) **f)** Experimental design of long-term low-dose FK506 in non-tumor bearing mice immunized with RHuT vaccine. BALB/c mice were pre-treated for 1 week with FK506 (0.02mg/Kg) before being vaccinated with RHuT plasmid or empty vector. Vaccination was repeated after 2 weeks, and mice were euthanized 35 days after the beginning of the experiment. All mice were daily treated with FK506 or vehicle through oral gavage. **g)** Titers of anti-Her2-neu antibodies (mean fluorescence intensity) in the sera of mice vaccinated (VAX) or not and treated with FK506 or vehicle. (n=3/5) **h)** ELISpot assay performed on splenocytes isolated from vaccinated and unvaccinated mice to measure IFN-γ-secreting cytotoxic T cells activated by the immunodominant peptide for ErbB2. (n=3/4) **i)** Amounts of lymphoid populations in the blood of vaccinated (VAX) or unvaccinated mice treated with chronic low-dose FK506 or vehicle. (n=3/5) **j)** Percentages of PD-1+ lymphocytes in the blood of the experimental groups of Fig. S5g. (n=3/5)

Data information: Statistical significance was tested with one-way ANOVA followed by Sidak's multiple comparison test in graph a, g, h; with two-way ANOVA in graphs b-e, i, j.

FK506 protects from cachexia in C26 tumor-bearing mice.

Since low-dose FK506 was found not to be immunosuppressive, we analyzed the effects of FK506 in cachexia. FK506-treated C26 tumor-bearing mice appeared healthier and less distressed than the untreated group (Video S1), as seen by the preservation of body weight (Fig. 5a) and fat tissue weight (Fig. 5b) at the endpoint of the experiment. Furthermore, the acute and severe skeletal muscle atrophy induced by C26 tumors was reverted upon FK506 treatment, as indicated by the increased muscle weights (Fig. 5c, d) and by the lower levels of atrogenes expression (Fig. 5e and Fig. S6a, b). In agreement with increased muscle weights, fibers cross-sectional areas (CSA) in the treated group were significantly higher than in controls (Fig. 5f, g). Since the tumor weight in FK506-treated and vehicle-treated mice was unchanged (Fig. 4b), protection against muscle wasting was not due to reduced tumor growth.

To assess whether the beneficial effect of FK506 was due also to increased protein synthesis, we performed the *in vivo* SuNSET assay. As shown in Fig. 5h, the reduced amount of newly synthetized proteins in atrophic muscles from tumor-bearing mice was fully rescued in FK506-treated samples (Fig. 5h and Fig. S6c), in further support to rescued CSA fiber size (Fig. 5f). Overall, these findings demonstrate that a low-dose of FK506 prevents skeletal muscle wasting and cancer cachexia *in vivo* (Fig. 5 and Fig. S6).

Figure 5

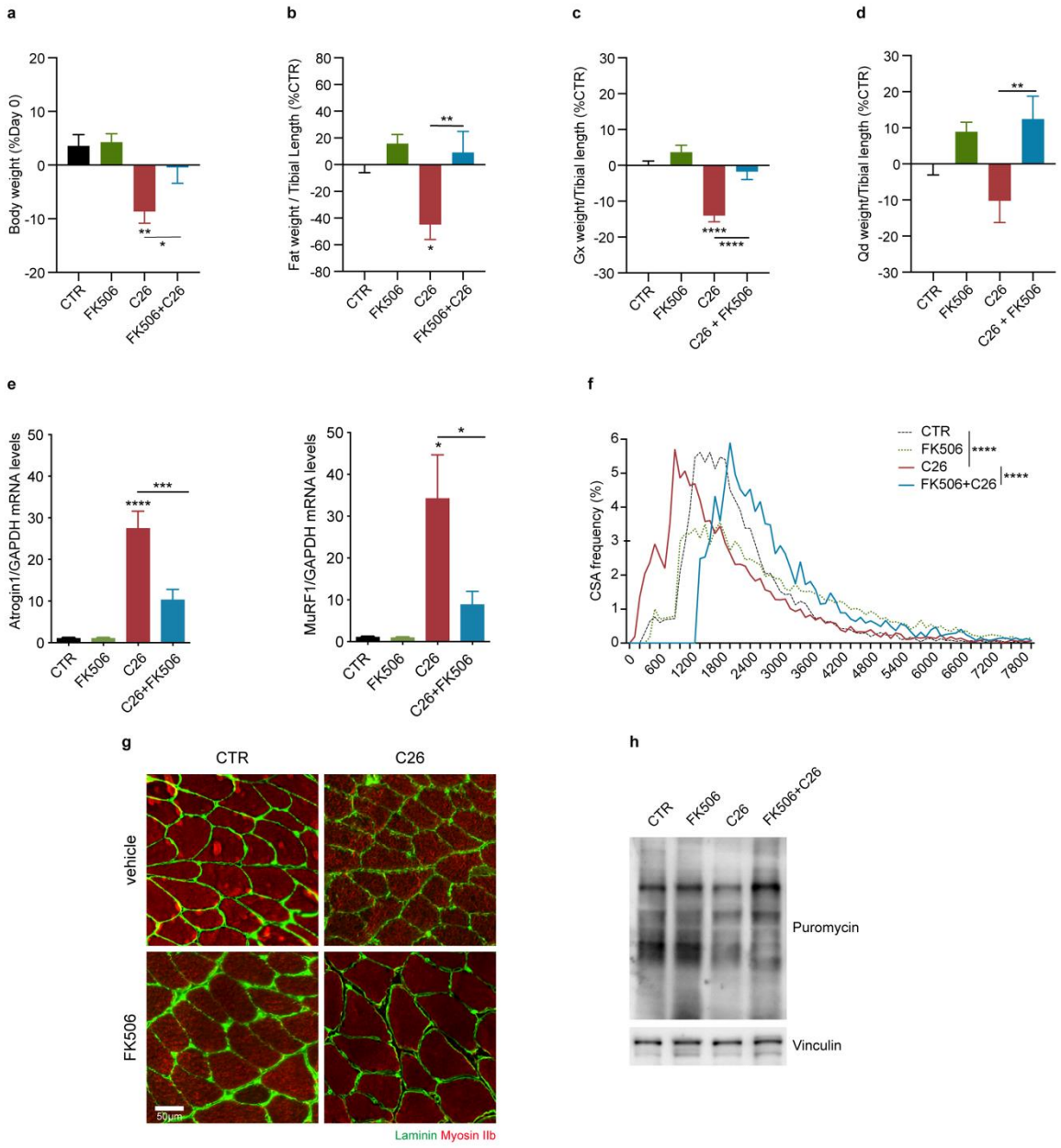
a
Body weight (%Day 0)
CTR
FK506
C26
FK506+C26
b
Fat weight / Tibial Length (%CTR)
c
Gx weight/Tibial length (%CTR)
C26 + FK506
d
Qd weight/Tibial length (%CTR)
e
Atrogin1/GAPDH mRNA levels
C26+FK506
MuRF1/GAPDH mRNA levels
f
CSA frequency (%)
g
vehicle
50µm
Laminin Myosin IIb
h
Puromycin
Vinculin

Figure 5. FK506 protects from cachexia in C26 tumor-bearing mice.

a) Body weight change as percentage of initial body weight in the experimental groups at day 11. (n=10/12) **b)** Fat weight normalized for the tibial length as percentage of non-tumor-bearing vehicle-treated mice at day 11. (n=6/7) **c-d)** Gastrocnemii (**c**) and quadriceps (**d**) weights normalized for tibial length as percentage of the control group 11 days post-C26 inoculation. (n=15/16 for gastrocnemii and n=11/12 for quadriceps) **e)** Expression levels of the atrogenes Atrogin1 and MuRF1 in the gastrocnemii of the experimental groups at day 12. (n=4/6) **f-g)** Frequencies distribution of the cross-sectional areas (CSA) of the fibers in the gastrocnemii of vehicle and FK506-treated control and C26 tumor-bearing mice and representative immunofluorescence pictures of gastrocnemii stained with Laminin (green) and Myosin IIb (red) (**g**). (n=4/5) **h)** *In vivo* SuNSET assay and immunoblot for puromycin performed with the gastrocnemii of the different groups. (n=3/4) See also Fig. S6.

Data information: Statistical significance was tested with one-way ANOVA followed by Sidak's multiple comparison test in graphs a-e, and with two-way ANOVA followed by Sidak's multiple comparison test in graph f.

FK506 prevents the degeneration of neuromuscular junction morphology and preserves muscle strength.

An important component of cachexia-induced skeletal muscle atrophy is the degeneration of the neuromuscular compartment [14]. Indeed, together with skeletal muscle atrophy, the decrease in muscle force in C26 tumor-bearing mice is prevented by FK506 treatment (Fig. 6a).

Coherently with the reduced muscle strength, cachectic mice showed smaller NMJs with a collapsed morphology (Fig. 6b, c) and downregulation of the adult nicotinic acetylcholine receptor subunit *Chrne* mRNA (Fig. 6d). On the contrary, FK506 treatment rescued NMJs volume, morphology and *Chrne* expression levels (Fig. 6b-d).

Considering the pre-synaptic compartment of the NMJs, we evaluated the denervation status in our C26 model, where we only found a trend in denervated NMJs (Fig. S6d). However, molecular alterations (*ie. Chrne* downregulation), and the reduction in NMJs volume, suggest an ongoing remodeling, but partially occurring, degenerative process, largely attributed to the rapid kinetics of the C26 cell suspension cachexia model.

Figure 6

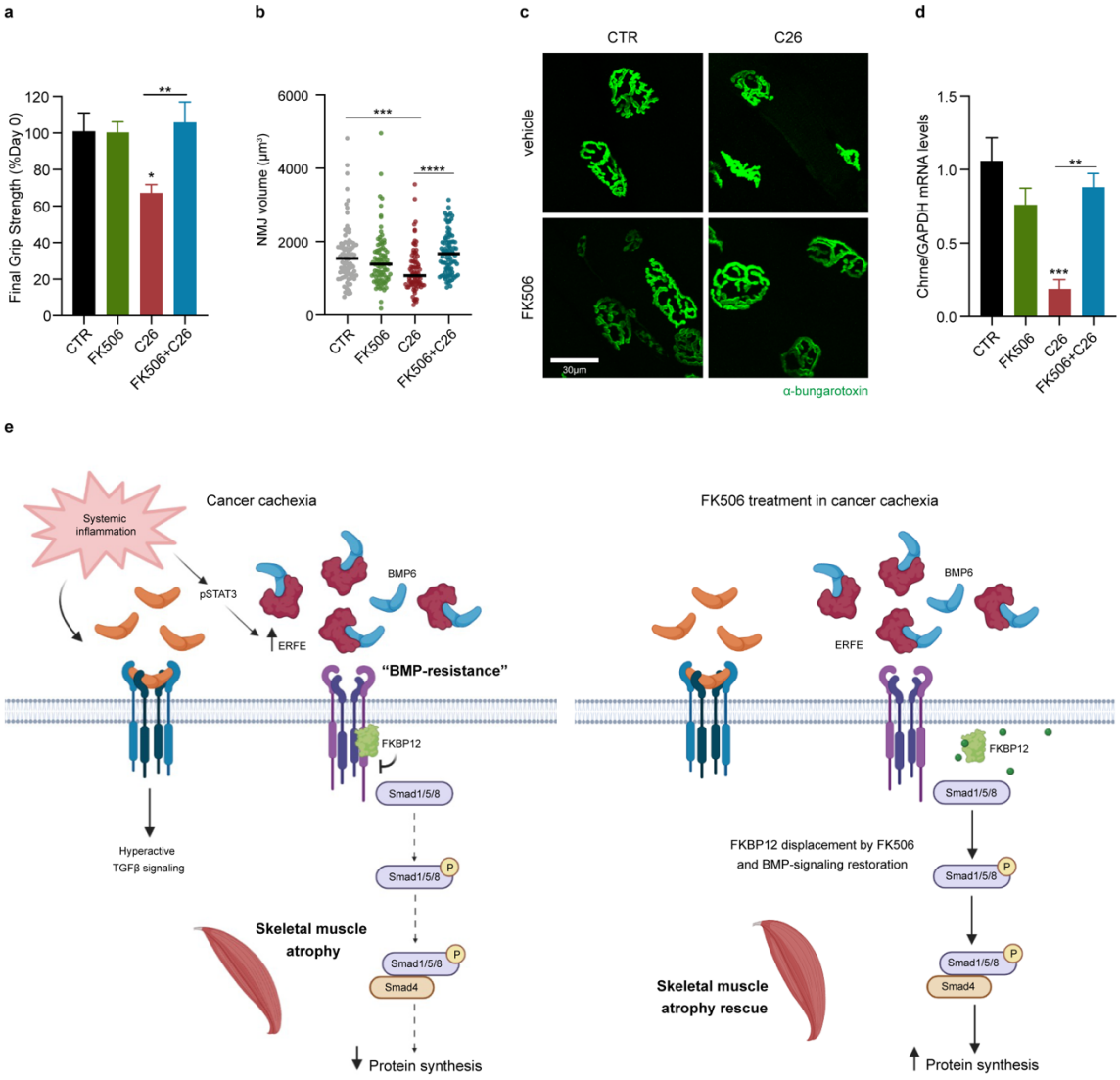
a
Final Grip Strength (%Day 0)
120
100
80
60
40
20
0
**
*
CTR
FK506
C26
FK506+C26
b
NMJ volume (µm³)
6000
4000
2000
0
***
****
CTR
FK506
C26
FK506+C26
c
CTR
C26
vehicle
FK506
30µm
α-bungarotoxin
d
Chrne/GAPDH mRNA levels
1.5
1.0
0.5
0.0
**
***
CTR
FK506
C26
FK506+C26
e
Systemic inflammation
Cancer cachexia
pSTAT3
BMP6
ERFE
"BMP-resistance"
FKBP12
Smad1/5/8
Smad1/5/8
P
Hyperactive TGFβ signaling
Skeletal muscle atrophy
Smad1/5/8
P
Smad4
Protein synthesis
FK506 treatment in cancer cachexia
BMP6
ERFE
FKBP12
Smad1/5/8
FKBP12 displacement by FK506 and BMP-signaling restoration
Smad1/5/8
P
Skeletal muscle atrophy rescue
Smad1/5/8
P
Smad4
Protein synthesis

Figure 6. FK506 prevents the degeneration of neuromuscular junction morphology and preserves muscle strength.

a) Final grip strength as percentage of initial grip strength at day 0 in FK506 or vehicle-treated C26 tumor-bearing and control mice at day 11 post-C26 injection. (n=5/7) **b-c)** Volume of the neuromuscular junctions quantified in the EDL muscle and stained with α-bungarotoxin - Alexa 488 (**b**) and relative representative picture of the experimental groups (**c**). (n=3, 28-30 NMJs quantified per mouse) **d)** Expression levels of *Chrne* gene in the gastrocnemii of FK506 or vehicle treated C26 and control mice at day 11 post-C26 injection. (n=3/4) **e)** Graphical representation of the molecular mechanism. In cancer cachexia, systemic inflammation induces catabolism by hyperactivating TGFb-Smad2/3 axis and by increasing the expression of BMP signaling inhibitors. Activated pSTAT3 induces the upregulation of the BMP-scavenger ERFE, which in combination with the intracellular inhibitor FKBP12, contributes to the downregulation of the BMP-pSmad1/5/8 axis and therefore reducing protein synthesis in atrophic muscles. Our therapeutical approach proposes the use of low-dose FK506, that by binding the immunophilin FKBP12 induces its displacement from the BMPR-I, rescuing pSmad1/5/8 signaling and protecting from muscle atrophy in cancer cachexia. See also Fig. S6.

Data information: Statistical significance was tested with one-way ANOVA followed by Sidak's multiple comparison test in all graphs.

Supplementary Figure 6

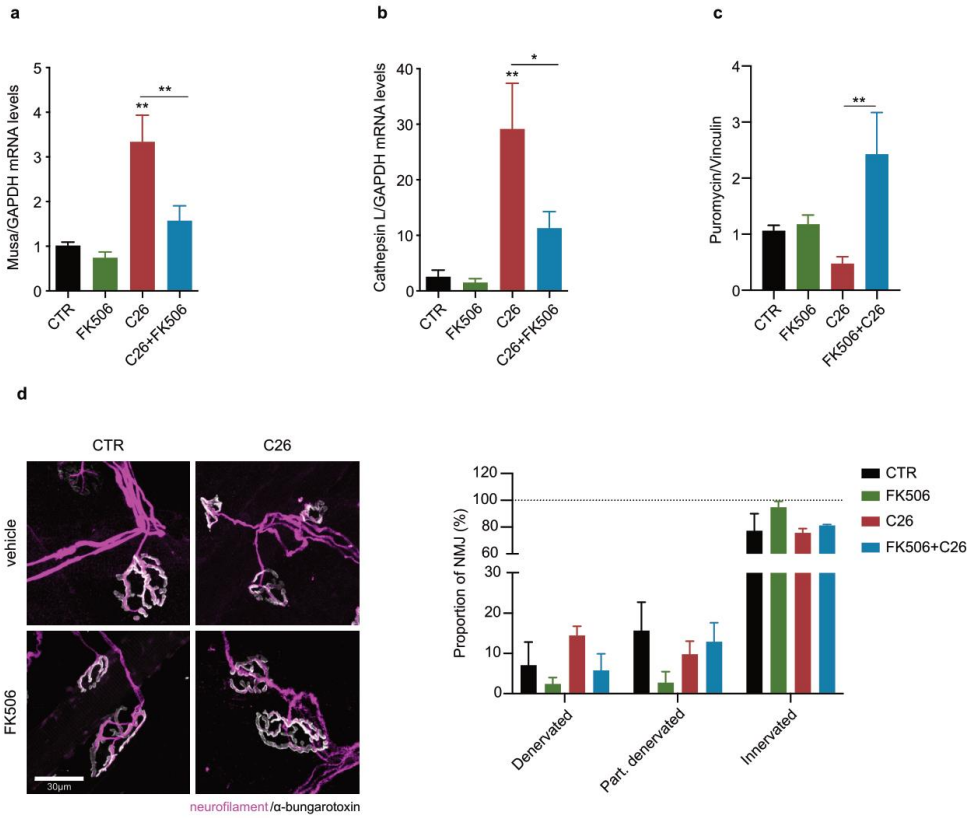

Figure S6: FK506 protects from cachexia, prevents the degeneration of neuromuscular junction morphology, and preserves muscle strength in C26 tumor-bearing mice. Related to Fig. 5 and Fig. 6.

a-b) Expression levels of the atrogenes Musa (**a**) and Cathepsin L (**b**) in the gastrocnemii of C26 and control mice treated with low-dose FK506 or vehicle. (n=4/6) **c)** Densitometric quantification of the *in vivo* SuNSET assay reported in Fig. 5h. (n=3/4). **d)** Representative immunofluorescence pictures and relative quantification of EDL muscles stained for α-bungarotoxin and anti-Neurofilament antibody to detect NMJs innervation. The quantification of denervated NMJs is expressed as percentage of the total number of NMJs quantified (60 to 90 NMJs per mouse, n=3 per group).

Data information: Statistical significance was tested with one-way ANOVA followed by Sidak's multiple comparison test in all graphs.

Video S1) FK506 protects from cachexia in C26 tumor-bearing mice. Related to Fig. 5. C26-tumor bearing mice treated with vehicle (left) or FK506 (right) at day 11 post-C26 injection. Related to Fig. 5, 6 and Fig. S6.

Discussion

Patients with cancer and chronic inflammatory diseases commonly develop cachexia, a multiorgan condition characterized by body weight loss, fat and skeletal muscle wasting [1]. Despite cachexia is related to anticancer treatments intolerance, worsening of prognosis and death of advanced cancer patients [3,4] it remains still uncurable and poorly characterized. From a physiological standpoint, one of the main signaling pathway having a role in controlling skeletal muscle mass is the TGFβ superfamily, where Activin/TGFβ-Smad2/3 signaling induces atrophy [21-25] and it is counteracted by the opposite BMP-Smad1/5/8 axis. The former indeed drives atrogenes expression and protein breakdown; while the latter induces protein synthesis [12,13].

Our results demonstrated that in cancer cachexia, a state of systemic inflammation contributes to the upregulation of the BMP-scavenger ERFE through STAT3 activation. This extracellular inhibition is combined with the activity of the immunophilin FKBP12, which acts as an intracellular brake for BMP-signaling activation. These two layers of inhibition contribute to decreased activation of pSmad1/5/8 in atrophic muscles and cachexia.
FK506 bypasses this state of "BMP-resistance" by displacing FKBP12 from the BMPR-I, restoring pSmad1/5/8 signaling *in vitro*, increasing protein synthesis, and preventing the degeneration of skeletal muscle functionality *in vivo* (Fig. 6e).

We thus identified two inhibitors of the BMP-signaling as mediators of muscle atrophy, previously characterized in the field of iron metabolism, *i.e.* the extracellular BMP ligand chelator erythroferrone (ERFE) and the intracellular inhibitor of the BMP receptor FKBP12. ERFE is a hormone produced by erythroid cells known to reduce Smad1/5/8 signaling in the liver by sequestering BMPs from their receptors [28,30,31]. Noteworthy, although ERFE is also expressed in the skeletal muscle (and named myonectin [32]), its biological function and mechanism of regulation in the muscle remains to be clarified. On the other hand, FKBP12 is a peptidyl-prolyl-cis-trans cytosolic isomerase that belongs to the immunophilin superfamily, known to form

various heterocomplexes, as its binding to the glycine-serine–rich domain of type I BMP receptors (BMPR-I) avoids their uncontrolled activation [49,50].

Our results demonstrated that in cachectic muscles, combined with the already known hyperactivation of the Smad2/3 axis [21-25], a "BMP-resistance" characterized by reduced BMP signaling is observed despite similar levels of BMP ligands. We found indeed that the BMP inhibitor ERFE is more expressed in models of cancer cachexia and in muscles of pre-cachectic and cachectic cancer patients. This indicates that some muscular alterations can precede the onset of cachexia, potentially contributing to its development. Of note, it has been even reported that conditions such as metabolic rewiring and muscle wasting, even predates the diagnosis of cancer [9,56,57].

We found that phosphorylated STAT3 (Tyr705) is recruited to putative STAT3 binding sites on the promoter of *Erfe* in cachectic muscles, and that its inhibition or knock-down is sufficient to prevent ERFE upregulation. STAT3 activation in the skeletal muscle is a key signaling pathway that drives wasting and cachexia [38], also due to the high levels of IL-6 in cachectic patients and mice [40,58-60].

We found that C26 conditioned medium, as well as IL-6, induced pSTAT3. The finding that stimulation with IL-6 was weaker than with conditioned medium could indicate that multiple cytokines can contribute to STAT3 activation in the C26 model. Indeed, while the tumor is undoubtedly a source of inflammatory cytokines and factors known to activate STAT3 [61], other compartments may also contribute to the chronic and systemic inflammation in cachexia. For instance, tumor-related dysbiosis [62] and altered gut permeability and endotoxemia [63,64] are known to promote STAT3 activation and cancer progression [65].

The functional relevance of the inhibitors ERFE and FKBP12 was subsequently characterized in *in vitro* and *in vivo* models of cachexia. ERFE supplementation significantly reduced myotube diameter, while *Fkbp12* knockdown protected from atrophy in C2C12 myotubes. Similarly, muscle-specific AAV-mediated delivery of shRNA against *Erfe* or *Fkbp12* was sufficient to reduce muscle atrophy induced by C26 tumor. These results are coherent with a previous study showing that Noggin, another BMP inhibitor, is upregulated and induces atrophy and denervation in

cachexia [14]. On the other hand, extracellular activators of the catabolic signaling exerted by pSmad2/3, as Myostatin and Activin A have been found to be highly expressed in cachectic patients and to induce muscle wasting in various murine models of cachexia [21,23,25,66,67]. However, the targeting of myostatin failed to be effective in cancer patients, leading to the suspension of the clinical study (LY2495655) [68] and pointing to the necessity of alternative targets.

A cause for this failure might be due to the redundancy of extracellular and intracellular TGFβ superfamily members. Therefore, targeting a single interactor might not be sufficient to generate a relevant biological effect. To bypass the redundancy and the extracellular ligands competition, we targeted the intracellular protein FKBP12 to restore BMP receptor signaling.

In absence of TGFβ superfamily ligands, FKBP12 binds BMPR-I [36,69] reducing their signaling [50,70], while high levels of BMP6 induce FKBP12 displacement from ALK2 receptor in hepatoma cells [33].

We found that FK506 fully rescues myotube atrophy, by activating pSmad1/5/8 axis and inducing protein synthesis *in vitro*. Interestingly, we observed the same effects in C26 tumor-bearing mice, where FK506-treatment reversed body weight loss and muscle atrophy by increasing fiber size and protein synthesis, and by preventing neuromuscular junction (NMJ) alterations.

Once upregulated, FKBP12 can bind several type I TGFβ superfamily receptors [49,52]. In 293T cells the supraphysiological expression of FKBP12 promotes moderate interaction with ALK3. However, in our study we found that FKBP12 preferentially binds ALK2, as in previous studies on hepatic Smad signaling regulation [33 34]. Hence, ALK2 knockdown in C2C12 myotubes reduces FK506-induced Smad1/5 phosphorylation, and its inhibition blunts the rescue of atrophy observed with FK506. Beyond its promiscuity to type I BMP receptors, FKBP12 has also been demonstrated to bind other proteins forming ternary structures as the rapamycin-FKBP12-mTOR complex. When FKBP12 is bound to rapamycin, the complex inhibits mTOR, with an immunosuppressive effect by blocking protein synthesis [71]. In our context we exclude any off-target effects on mTOR inhibition by FK506, as we observed increased protein synthesis upon FK506 treatment *in vitro* and *in vivo*, while mTOR inhibition by Torin1

blunts the hypertrophy induced by FK506 in C2C12 myotubes.
Given the immunosuppressive action of FK506 we tested the effect of low doses in order to maintain immune responses [47]. In agreement, no alterations in the immunological landscape were present in mice treated with neither long nor short term FK506 treatment. Further indications that FK506 effect is independent from immunosuppression are represented by the curb of atrophy observed by direct FKBP12 knocked-down in muscles. Moreover, cyclosporine A, an inhibitor of calcineurin independent from FKBP12, induces atrophy in C2C12 myotubes.

An emerging feature of muscle wasting in cancer is the progressive loss of NMJ integrity due to reduced Smad1/5/8 signaling [14]. This pathway has indeed been shown to be involved in NMJ fitness and functionality [14,26,27], suggesting that FK506 might contribute to maintain the cross-talk between the skeletal muscle and the NMJ through the BMP-Smad1/5/8 signaling. In agreement, we found that FK506 preserved the volume and morphology of the NMJ in C26 tumor-bearing mice and reverted the downregulation of the adult epsilon subunit of the nicotinic acetylcholine receptor, a known marker of functional adult NMJ [72].

The use of a potentially immunosuppressive drug in cancer patients might be counterintuitive and would require fine dose-optimization in humans to avoid undesired immunosuppression. Despite these limitations, the off-label use of an approved drug significantly reduces the costs of development of a new molecule, as its safety and toxicity are already known. Moreover, further studies in a slower-paced cachexia will be important to move closer to human physiology. As previously described, cachexia affects patients with chronic inflammatory diseases like cancer, COPD, AIDS, or sepsis, and it still represents an unmet medical need [2,73]. Our results on improved muscle functionality and protection from neuromuscular junction alterations, can expand this therapeutical approach to neuromuscular diseases independent of cachexia.

Limitations of the Study

We acknowledge some limitations to our study. The study has been performed mostly with a specific murine cancer model, *i.e*. the C26, which is an injectable tumor cells suspension characterized by a rapid development of cachexia. Hence, to understand the global impact of FK506 treatment on cancer cachexia, it would be important the use of models with slower kinetic, such as GEMMs, or in combination with clinically relevant treatments such as chemotherapy. It would also be interesting to determine whether our characterization is specific to the C26 model, or the features are also shared in other tumor models.

Considering the translatability in the clinic, the use of an immunosuppressive drug as FK506 could be critical in cancer patients. Therefore, the identification and optimization of the effective dose of FK506 to trigger Smad1/5/8 pathway without providing immunosuppression in humans would be required.

Finally, even though we found that the hormone ERFE is upregulated in human pre-cachectic and cachectic muscle biopsies, longitudinal studies in cancer patients are required to determine causality and the identification of ERFE as potential prognostic marker.

Acknowledgements

The research leading to these results has received funding from AIRC under MFAG 2018 - ID. 21564 project – P.I. Porporato Paolo Ettore; PoC Instrument 2021 and AIRC under MFAG 2022 ID. 25908 project – P.I. Alessio Menga. European Research Council (ERC) under the European Union's Horizon 2020 research and innovation program (grant agreement no. 715491) to P.I. Léon Kautz and Project Age-it, PE0000015, PNRR MUR – M4C2 1.3 funded by Next-Generation EU to P.I. Andrea Graziani.

The authors are thankful to Alessandro Bertero, Matteo Biolatti, Fabio Penna for helpful discussion and to Alessandra Ghigo, Lidia Avalle, Natalia Cortez-Penso and Chiara Ambrogio for technical support.

Author Contributions

Conceptualization: E.M., P.E.P.

Formal analysis: E.M., R.S, A.M., P.E.P.

Investigation: E.M., E.W., R.S., L.C., V.R., M.M., E.A.

Resources: A.P., L.S., A.G., L.K., S.O., E.H., M.H., A.F., C.S., M.S.

Data curation: E.M.

Writing-Original Draft: E.M., P.E.P.

Supervision: P.E.P.

Declaration of interests

The authors E.M., V.R, L.S, P.E.P. declare to be inventors of the patent PCTIB2022050175 (WO2022/149113).

Table S1

Gene	Species	Forward	Reverse
Atrogin1	Mouse	ATGCACACTGGTGCAGAGAG	TGTAAGCACACAGGCAGGTC
Murf1	Mouse	GTGTGAGGTGCCTACTTGCTC	GCTCAGTCTTCTGTCCTTGGA
Musa1	Mouse	TCGTGGAATGGTAATCTTGC	CCTCCCGTTTCTCTATCACG
Cathepsin L	Mouse	GTGGACTGTTCTCACGCTC	TCCGTCCTTCGCTTCATAGG
FKBP12	Mouse	ATGGGAGTGCAGGTGGAG	TCTTTCCATCTTCAAGCATCC
ERFE	Mouse	TGCTTGGATGCTGTTCGTCAA	CAGATGGGATAAAGGGGCCTG
GAPDH	Mouse	AGGTCGGTGTGAACGGATTTG	TGTAGACCATGTAGTTGAGGTCA
BMP6	Mouse	GGGATGGCAGGACTGGATCA	ATGGTTTGGGGACGTACTCG
BMP2	Mouse	CATCACGAAGAAGCCGTGGA	TGAGAAACTCGTCACTGGGG
BMP4	Mouse	TTCCTGGTAACCGAATGCTGA	CCTGAATCTCGGCGACTTTTT
Chrne	Mouse	GTGTCTGGATTGGCATTGACT	ACACCTGCAAAATCGTCCTTG
ERFE	Human	GGCCAAGAAGCTGAAGTTCGG	CTGCCGCACCGCACCTTTC
Beta Actin	Human	GGGAAATCGTGCGTGACA	GGACTCCATGCCCAGGA
ChIP-qPCR Erfe promoter	Mouse	GGGTGGATTGGTAGCCTTCA	TGCCTTGCAGAGGGAGGTAT
ChIP-qPCR Fkbp12 promoter	Mouse	ATTCGTGGAAGAGTGGGCTT	TGCCCTGTAAGGACGATAGC
ChIP-qPCR Negative Ctr	Mouse	TGGCCCCATAGGCTCATCTA	GGCCTGGCATGAGAGACTTT

Table S1: RT-qPCR SYBR primers and ChIP-qPCR primers. Related to STAR Methods.

Star methods

RESOURCE AVAILABILITY

Lead Contact

Requests for resources and reagents, or any additional information should be directed to the lead contact, Dr. Paolo Ettore Porporato (paolo.porporato@unito.it).

Materials Availability

Plasmids generated in this study will be available on request through completion of a Material Transfer Agreement.

Data and Code Availability

Any additional information required to reanalyze the data reported in this paper, or any sharing of data of this study is available from the lead contact upon request. This paper does not report original code.

EXPERIMENTAL MODEL AND SUBJECT DETAILS

Human skeletal muscles biopsies

The study enrolled patients (age > 18 years) with colon or pancreatic cancer surgically treated at the General Surgery 1, Padova University Hospital (Padova, Italy) from 2016 to 2021. Cancer patients were classified as cachectic in cases of >5% weight loss in the 6 months preceding surgery, >2% weight loss with either body mass index (BMI) <20 or low muscle mass defined by the skeletal muscle index (SMI) cut-offs [74]. SMI values were quantified using the preoperative CT scans as previously described ([14]. The study also enrolled control, healthy donors undergoing elective surgery for non-neoplastic and non-inflammatory diseases. Patients with presence of active inflammatory or infective diseases, known myopathies, or viral infections were excluded. All patients joined the protocol according to the guidelines of the Declaration of Helsinki and the research project has been approved by Ethical Committee for Clinical Experimentation of Provincia di Padova (protocol number

3674/AO/15). Written informed consent was obtained from participants. The biopsies were collected during elective surgery within 30 min of the start of the surgery by cold section of a rectus abdominal fragment of about 0.5–1 cm. The fragment was immediately frozen and conserved in liquid nitrogen for gene expression analysis.

Animals

All animal experiments were authorized by the Italian Ministry of Health and carried out according to the European Community guiding principles in the care and use of animals.

All mice were 6 to 8 weeks old female BALB/c, purchased from Charles River Laboratories and housed in a pathogen-free environment and kept food and water ad libitum.

Cell lines

C2C12 myoblasts (CRL-1772), NIH/3T3 (CRL-1658), HEK-293T (CRL-3216), cells were purchased from ATCC, while HuH7 cells were provided by Dr. Laura Silvestri and C26 cells were kindly gifted by Dr. Nicoletta Filigheddu (Università del Piemonte Orientale). All cells were cultured in DMEM/10% FBS. For C2C12 myoblasts differentiation into myotubes, when full confluency is reached, the medium is switched to 2% horse serum (HS) DMEM for 4 days.

Method details

Cell Culture

Conditioned medium (CM) was prepared as previously described. [10] Briefly, cancer cells were grown to high confluency, then conditioned in serum-free DMEM for 24h, medium was harvested and centrifuged at 500g for 10min. Supernatant was subsequently used as conditioned medium.

Myotubes were treated with Activin A (R&D #338-AC), BMP6 (Novus Biologicals #6325-BM), cyclosporine A (Tocris Biosciences #1101), DMH1 (Sigma #D8946) and b-cyclodextrin (Sigma #C4767), Erythroferrone (Aviva Systems Biology

OPCA03036), FK506 (Cayman Chemical 10007965), Fc hIgG2/FLAG (CTR Fc), Fc hIgG2/FLAG-ERFE and ERFE globular domain (gERFE) were kindly provided by Prof. Leon Kautz (IRSD, Toulouse), IL-6 (Peprotech #216-16), puromycin (Santa Cruz Biotechnology sc-108071), stattic (Abcam #120952), Torin-1(Tocris Biosciences #4247).

For *in vitro* immunofluorescence, C2C12 myoblasts were seeded in a 96-well plate (Ibidi) and differentiated into myotubes. Once treated, cells were fixed in 4% PFA at room temperature and then permeabilized with 0.1 % Triton X-100. Nonspecific binding was blocked by incubation of permeabilized cells in 1% BSA for 1h at room temperature. Cells were then incubated overnight at 4°C with a primary antibody against myoglobin (Abcam # 77232) diluted 1:400 in 1% BSA. A secondary antibody conjugated with Alexa Fluor 488 (Thermo Fisher) was applied for 1H at room temperature. Pictures were acquired with a confocal microscope (Leica SP8).

Myotube diameter measurement

For Myotube diameter quantification, pictures of myotubes were taken 24h after treatment with phase contrast microscopy (Zeiss) at 20x magnification, and myotube diameter was measured using the software ImageJ as previously described. 75

siRNA-induced knockdown

C2C12 myotubes were transfected with siRNAs at day three of differentiation using Lipofectamine RNAiMAX reagent (Thermo Fisher Scientific, #13778). Briefly, in a 12-well plate, the medium was replaced with 200µl fresh medium, transfection mix was prepared (2x 25µl Opti-MEM, Thermo Fisher Scientific, #1985047; 2µl RNAiMAX; 50pmol siRNA) and carefully added. After 4-6hours 1ml of medium was added and myotubes were analyzed 72h post-transfection. siRNA sequences are reported in the Key Resources Table.

NIH/3T3 were knocked-down with siSTAT3 or with siCTR (1ug/mL) for 72h, as previously described 76.

Luciferase assay

For Erfe promoter-Luciferase reporter assay, Erfe promoter (sequence in Supplementary Table 1) was cloned in a luciferase vector and purchased on Vector Builder. NIH/3T3 cells were co-transfected with 1ug of DNA (ratio 1:6 Renilla:Firefly) using Lipofectamine2000 (Thermo Fisher Scientific, #11668019). After 16h, the transfection mix is aspired and substituted with siSTAT3 or siCTR mix to induce STAT3 knock-down. 50% C26 CM or IL-6 (100ng/mL) were then added to the cells 72h post plasmid transfection, for 16h. Dual-Luciferase® Reporter Assay System (Promega) was then performed following the manufacturer's instructions.

C2C12 myoblasts were seeded into a 48-well plate and co-transfected with pGL3-BMP responsive element (BRE)-Luc plasmid and TK Renilla. Co-transfection was performed with 800ng of DNA/well at a 1:6 ratio of Renilla:Firefly using Lipofectamine2000. Transfection mix was added to each well containing 100µl of fresh medium. 4-6h post-transfection 500µl of fresh medium was added into each well. The next day, cells were serum starved for 4h and subsequently treated with 30ng/ml BMP6 and 10µg/ml FK506 in 2% FBS medium. Luminescence was measured using Dual-Luciferase® Reporter Assay System (Promega) after 5h of treatment.

Western Blotting

Crushed skeletal muscle samples or C2C12 myotubes were lysed in RIPA lysis buffer (150mM NaCl, 50mM Tris-HCl, 0.5% sodium deoxycholate, 1.0% Triton X-100, 0.1% SDS, and 1mM EDTA) supplemented with protease and phosphatase inhibitor cocktail (Roche). Protein concentration was determined using BCA assay (Thermo Fisher Scientific). 15 to 30µg of proteins from cell lysates were loaded for SDS-PAGE and then transferred to PVDF membrane prior to immunoblotting analysis. Blots were probed with the following primary antibodies: FKBP12 (Invitrogen, PA1-026A), FLAG-Tag (Cell Signaling, #8146), GAPDH (Millipore, MAB374), Myc-Tag (Cell Signaling, #2278), Smad1 (Cell Signaling, #9743), P-Smad1/5 (Cell Signaling, #13820T), pSmad1/5/9 (Cell Signaling, #13820), STAT3 (Cell Signaling, #4904),

pSTAT3 (Cell Signaling, #9145), vinculin (Cell Signaling, #4650), puromycin (Millipore, MABE343).

***In vitro* co-Immunoprecipitation (Co-IP)**

The pCMV6-ALK2-MYC, the pCMV6-ALK3-MYC and the pCMV6-FKBP12-FLAG expressing vectors were kindly provided by Prof. Laura Silvestri (San Raffaele Scientific Institute, Milan).

HuH7 cells were lipofected with FKBP12-FLAG and ALK2-MYC or ALK3-MYC using Lipofectamine 2000 (Thermo Fisher Scientific, #11668019) according to manufacturer's instructions. Briefly, HuH7 cells were transfected with 20ug DNA with 1:1 ratio (ALK:FKBP12 or ALK:pCMV6 empty vector) in antibiotic-free medium. 16h after lipofection, the medium is changed with fresh DMEM/10%FBS.

HEK-293T cells were transfected in HEPES and CaCl2 with 5ug DNA with 1:1 ratio (ALK:FKBP12 or ALK:pCMV6 empty vector) and 16h later, the medium is refreshed with DMEM/10%FBS.

The next day, HuH7 or 293T cells are starved in DMEM/2%FBS for 3h and treated with FK506 for 1h. Cells are subsequently washed and pelleted in ice-cold PBS. Pellets are lysed in NET buffer (50mM NaCl, 5 mM EDTA, 10 mM Tris pH 7,4, 1% Triton X-100) and protease inhibitors. 500ug of proteins are incubated with the anti-FLAG M2 affinity gel (Sigma Aldrich) at 4°C for 2 hrs. After gel washing, samples were eluted with 18µl of Laemmli sample buffer (without β-mercaptoethanol) and incubated at 95°C for 5 minutes. After centrifugation, β-mercaptoethanol was added to supernatants and SDS-PAGE was performed.

Animal experimentation

Adeno-associated virus (AAV) AAV9-shRNA delivery was performed in 8 weeks old female BALB/c mice under inhalation of isoflurane in medical oxygen. 10^{11} AAV9-shRNA or AAV9-shCTR viral particles were resuspended in PBS for a final volume of 50uL. Using the Hamilton (PB600-1) Repeating Dispensers (1uL), 10 injections of 5uL were performed in the gastrocnemii of the mice. AAV9-shCTR injections were executed in the contralateral gastrocnemius, and the two constructs were equally

side-exchanged within the experimental groups.

Four weeks after AAV9 delivery, colon-26 (C26) murine adenocarcinoma cell suspension (750.000 cells per mouse) was inoculated subcutaneously into the flank and euthanized after 11 days.

Concerning all FK506 (Cayman Chemical 10007965) *in vivo* administration, FK506 was dissolved in DMSO (5mg/mL) and further diluted in glucose-water (5%) to daily administer 0.02mg/Kg in 100uL of volume, through oral gavage. All mice were daily treated either with vehicle DMSO buffer glucose (5%) or with FK506.

For RHuT immunization, 6-8 weeks old male or female BALB/c mice were pre-treated for 1 week with FK506 or vehicle before the first dose of vaccination.

In colon-26 (C26) experiments, all mice underwent one day of pre-conditioning before C26 inoculation. The body weight of the mice was measured every 3 days, while the maximal grip strength was measured every 4 days with BIOSEB (BIO-GS3) instrument. All mice were anesthetized and sacrificed at day 11 post-inoculation. Fresh blood was collected through intracardiac puncture and serum was extracted by centrifuging clotted blood at 2,000g for 15 min at 4°C. All gastrocnemii (Gx), quadriceps (Qd), tibialis anterior (TA), extensor digitorum longus (EDL), white fat deposits, livers, spleens and tumors were freshly isolated, weighted and normalized to the respective tibial length, measured with a caliper.

Eythroferrone enzyme-linked immunosorbent assay (ELISA)

Serum protein levels of erythroferrone were measured with Intrinsic Lifesciences mouse ERFE ELISA kit (ERF-200) according to manufacturer's instructions.

Protein synthesis measurement with SuNSET assay

To assess protein synthesis in skeletal muscles *in vitro* and *in vivo*, SuNSET assay was performed as previously described [77,78].

Concisely, C2C12 myotubes were treated with C26 CM or Activin A in DMEM/2%HS for 24h. For the last 4h of treatment, cells were supplemented with puromycin (1uM) and subsequently lysed in RIPA with protease and phosphatase inhibitors. Any kD SDS-PAGE was then performed prior to immunoblotting with puromycin antibody.

For the *in vivo* measurements of protein synthesis (IV-SuNSET), all mice received an intraperitoneal injection of 0.040μmol/g of puromycin dissolved in 100 μl of PBS. Subsequently, they were anesthetized and sacrificed in order to snap-freeze in liquid N2 all muscles exactly at 30 min after puromycin injection. Whole protein lysates in RIPA with protease and phosphatase inhibitors were then processed for SDS-PAGE and immunoblotting as described before.

C2C12 myotubes and skeletal muscles chromatin immunoprecipitation (ChIP-qPCR)

Three fully confluent 10cm dishes of C2C12 myotubes per condition (untreated and pure C26 CM for pSTAT3, STAT3, H3K27ac, IgG) were crosslinked with 1% formaldehyde for 10 min at RT. Formaldehyde was quenched by 0.125mM glycine for 5 min at RT. Crosslinked cells were quickly washed with cold PBS and collected in cold PBS.

Nuclear extracts were prepared by using isotonic buffer. Briefly, C2C12 myotubes were lysed in isotonic buffer containing 20 mM HEPES pH 7.5, 100 mM NaCl, 250 mM Sucrose, 5 mM MgCl2, 5mM ZnCl2 supplemented with 1% NP40. Cell pellets were resuspended in SDS ChIP lysis buffer containing 50mM Tris-HCl pH 8.0, 10 mM EDTA, 0.5% SDS and protease inhibitors. Chromatin was sheared to an average DNA fragment length of 200-500 bp using Picoruptor sonicator (Diagenode) (12 cycles, 30s on/ off). Cell lysates were diluted five times with the ChIP dilution buffer lacking SDS and composed by 17 mM Tris-HCl pH 8, 1%TRITONx100, 1.2 mM EDTA, 170 mM NaCl to a final concentration of 0.1% SDS and used for immunoprecipitation with 4 μg of anti-Stat3 (phospho Y705) antibody (Cell Signaling, #9145), anti-H3K27ac antibody (Abcam, ab4729), and an unspecific normal rabbit IgG as a control. After overnight incubation of the chromatin with the antibodies at 4°C, the immunocomplexeswere captured with 10μl of Protein G-Dynabeads (Life technologies) for further 2h at 4°C.

For Stat3 ChIP, the protein G-bound immunocomplexes were washed four times with buffer containing 50mM HEPES pH 7.6, 500mM LiCl, 1 mM EDTA, 1% NP-40, 0.7% Sodium Deoxycholate and protease inhibitors, while for H3K27ac ChIP were washed with the following buffers: low salt wash buffer containing 20 mM Tris-HCl

pH8.0, 0.1% SDS, 1% TRITONx100, 2 mM EDTA, 150 mM NaCl; high salt wash buffer containing 20 mM Tris-HCl pH8.0, 0.1% SDS, 1% TRITONx100, 2 mM EDTA, 500 mM NaCl; LiCl wash buffer containing 10 mM Tris-HCl pH8.0, 1% Sodium Deoxycholate, 250 mM LiCl, 1 mM EDTA, 1% NP40 and protease inhibitors. Immunocomplexes were eluted from the beads and crosslinking was reversed by incubation for overnight at 65 °C with TE buffer containing 1% SDS. DNA from immunoprecipitated samples as well as DNA from 10% input was purified by using QIAquick PCR Purification Kit (Qiagen), according to the manufacturer's instruction.The Stat3 ChIP and the H3K27ac ChIP were analyzed by ChIP-qPCR using SYBR GreenER kit (Invitrogen) on target genomic regions (Table S1). qPCR reactions were performed on a Rotor-Gene Q 2plex HRM Platform (Qiagen, 9001560). The data are expressed as a percentage of the DNA Input.

For *in vivo* chromatin immunoprecipitation, two entire frozen quadriceps per condition (CTR and C26 for pSTAT3, H3K27ac, IgG) were homogenized with a dounce homogenizer in 1200uL nuclear extraction buffer composed by 10mM Tris HCl, 10mM NaCl, 3mM $MgCl_2$, 10mg/mL BSA, 0.1% IGEPAL, 0.5mM DTT and protease inhibitors. Afterwards, 37% formaldehyde was added to the lysates to reach a final concentration of 1%, and incubated at room temperature for 10 min, tapping occasionally to mix. The crosslinking reaction was interrupted by adding 75uL of 1.25M glycine on ice for 5 min. Samples were centrifuged at 1000 X *g*, 4°C for 10 min.

Cell pellets were resuspended in SDS ChIP lysis buffer containing 50mM Tris-HCl pH 8.0, 10 mM EDTA, 0.3% SDS and protease inhibitors. Chromatin was sheared to an average DNA fragment length of 500 bp using Picoruptor sonicator (Diagenode) (15 cycles, 30s on/ off). After sonication, the samples were processed as *in vitro* ChIP-qPCR.

Histology

Extracted gastrocnemii were immediately frozen in isopentane cooled in liquid nitrogen and stored at -80°C. Transversal sections of 10µm were cut at the midbelly with a cryostat. Cross sectional area was determined by sections fixation for 10 minutes in PFA 4% PBS, then blocking with Triton X-100 0.1%, BSA 3% in PBS before

incubating with primary antibodies against laminin (Santa Cruz Biotechnology sc-59854), followed by incubation with corresponding secondary antibodies (Alexa Fluor 488) and DAPI (Abcam 228549). Pictures were taken as mosaic of the full section with a confocal microscope (Leica SP5) and fiber areas were measured with MorphoLibJ plugin for Image J [79].

Neuromuscular junction analysis

Extensor digitorum longus (EDL) muscles were immediately fixed in PFA 4% PBS for 10 minutes and placed in cold PBS. The full muscles were stained with fluorescently tagged α-bungarotoxin - Alexa 488 (Thermo Fisher B13422) for 90 min 1:500 in PBS at RT. The whole muscles were mounted and pictured with fluorescence confocal microscopy (Leica SP5).

Each post-synaptic NMJ has been acquired through 1 µm thick Z-stack, and voxel were automatically quantified with ImageJ software.

For denervation quantification, fixed EDL muscles were permeabilized for 2h at RT in 2% TritonX-100 in PBS, then blocked in 4% BSA - 1% TritonX-100 in PBS. The primary antibody anti-neurofilament-H (heavy) (Abcam #Ab4680) was incubated 1:1000 in blocking buffer at 4°C overnight. 3 x 20' PBS washes were followed by secondary antibody and fluorescently tagged α-bungarotoxin - Alexa 488 (Thermo Fisher B13422) incubation and whole mount. Pictures were acquired with fluorescence confocal microscopy (Leica SP8). Denervation was measured evaluating 60 to 90 NMJs per mouse (with a total of three mice per treatment group). Our scoring system, ranged from 0 to 2: 0 for complete denervation, 1 for partial denervation, and 2 for full innervation.

RNA isolation and quantitative PCR (qPCR)

Total RNA was isolated from snap-frozen tissue samples using TRIzol reagent (Invitrogen) according to the manufacturer's guidelines. 0.5µg of total RNA was reverse transcribed using the High Capacity cDNA Reverse Transcriptase kit (Applied Biosystems) following the manufacturer's instructions. cDNA was analyzed by Real Time Quantitative PCR (ABI PRISM 7900HT FAST or Quant Studio

6 Real-Time PCR system, Applied Biosystems) using the PowerUp SYBR Green master mix (Applied Biosystems #A25742) and primers were designed according to Harvard validated PrimerBank. Relative mRNA levels were calculated using the 2-ΔΔCT method and normalized to GAPDH mRNA. For human muscle biopsies, total RNA was extracted from approximately 20 mg of rectus abdominal muscle using TRIzol (Invitrogen). 1 ug of RNA was reverse transcribed using the SuperScript IV Reverse Transcriptase (Thermo Fisher Scientific). Gene expression was analyzed by qRT-PCR (Quant Studio 5 Real-Time PCR system, Applied Biosystems) using the PowerUp SYBR Green Master Mix (Applied Biosystems #A25742). Data were normalized to ACTB gene expression. All RT- qPCR primers are listed in Table S1.

Adeno-associated virus (AAV) shRNA cloning

For the in vivo adeno-associated virus (AAV9-shRNA) delivery, short hairpin sequences targeting ERFE (shERFE - TRCN0000178969), FKBP12 (shFKBP12 - TRCN0000012492) or scramble sequence (shCTR) were cloned in the AAV plasmid and assembled in viral particles as previously described [78,80]

FACS

Fresh primary C26 tumor specimens of 8–10 mm mean diameter were finely minced with blades and digested by incubation with 1 mg/mL collagenase IV (Sigma Aldrich) in RPMI-1640 at 37°C for 1 h in an orbital shaker. After washing in RPMI-1640 with 10% FBS, the cell suspension was passed through a 70 µm pore cell strainer, centrifuged at 1400 rpm for 10 min and incubated in erythrocyte lysing buffer (155 mM NH_4Cl, 15.8 mM Na_2CO_3, 1 mM EDTA, pH 7.3) for 10 minutes at room temperature. After washing in RPMI-1640 with 10% FBS, 1 * 10^6 cells were collected, re-suspended in PBS, and treated with Fc-receptor blocker (anti-CD16/CD32 antibody, #101302, Biolegend). Splenocytes were collected by smashing spleens from vaccinated mice on a 40 µm pore cell strainer, centrifuging the resulting cells at 1400 rpm for 10 min and incubating them in erythrocyte lysing buffer, followed by treatment with Fc-receptor blocker. 50 uL heparinized blood collected by intracardiac injection were incubated with erythrocyte lysing buffer, washed and incubated with Fc-receptor blocker. After Fc-receptor blocking, all samples were

stained for 30 min at 4 °C with the following antibodies, as reported previously [81]: anti-CD45-VioGreen (#130-123-900), anti-CD3-FITC (#130-119-135), anti-CD4-APC/Vio770 (#130-119-134), anti-CD8-VioBlue (#130-123-865), anti-CD49b-PE (#130-102-337), anti-PD1-APC (#130-102-263), anti-CD11b-FITC (#130-113-234), anti-F4/80-PE/Vio770 (#130-118-459), anti-Ly6C-APC/Vio770 (#130-111-917), anti-Ly6G-VioBlue (#130-119-986), anti-MHCII-APC (#130-112-388), anti-CD11b-FITC (#130-113-234), anti-CD11c APC (#130-110-839) (all from Miltenyi Biotec) anti-CD69-PE/Vio770 (#104512, Biolegend), anti-CD206-PE (#141706, Biolegend) and anti-PDL1-PE (# 558091, BD Bioscience). Samples were acquired on BD-FACSVerse and cell populations (NK: $CD3^-$ $CD49b^+$; NKT: $CD3^+$ $CD49b^+$; $CD4^+$ T cells: $CD3^+$ $CD49b^-$ $CD4^+$; $CD8^+$ T cells: $CD3^+$ $CD49b^-$ $CD8^+$; DC: CD11b- CD11c+; macrophages: $CD11b^+$ $F4/80^+$; m-MDSC: $CD11b^+$ $F4/80^-$ $Ly6G^-$ $Ly6C^{high}$; gMDSC: $CD11b^+$ $F4/80^-$ $Ly6G^+$ $Ly6C^{dim/neg}$) analyzed with FlowJO10.5.3 and reported as percentage on the CD45+ leucocyte population, following doublets and dead cells elimination.

Vaccine preparation and mouse immunization

A plasmid coding for chimeric rat and human ErbB2 extracellular and transmembrane domains (RHuT) [82] and the corresponding control empty plasmid pVAX1 (Invitrogen, Monza, Italy) were amplified and then purified using the Endofree Qiagen Plasmid-Giga (Qiagen Inc., Cjatsworth, CA) following manufacturer's instructions. Vaccination was performed by injecting 50 µg of DNA diluted in 20 µl of 0.9% NaCl into the quadriceps muscle of anesthetized mice. Immediately after the vaccine injection, the muscle was electroporated by using an array needle electrode connected to an electroporator (Cliniporator™, IGEA, Carpi, Italy). Two 25-ms trans-cutaneous low voltage electric pulses with an amplitude of 150 V spaced by a 300-ms interval were applied [83]. Vaccination was repeated 14 days later. Two weeks after, mice were culled and sera and spleens were collected.

Antibody response

Blood samples were collected 14 days after the last vaccination and serum obtained by centrifugation. The concentration of anti-rat Her2 antibodies was determined by flow cytometry as the ability of diluted sera (1:200) to bind 3T3/NKB

cells (BALB/c 3T3 NKB, expressing the rat ErbB2, H-2K^{d}, and B7.1 molecules) [84], which were a generous gift from Dr. Wei-ZenWei (Karmanos Cancer Institute, Detroit, MI, USA). A FITC-conjugated rabbit anti-mouse IgG antibody (F313, Dako, Milano, Italy) was used to detect the bound primary antibodies. Flow cytometry was performed with a BD-FACSVerse and samples were analyzed with FlowJO10.5.3, and antibody titers reported as mean fluorescence intensity (MFI).

IFN-γ enzyme-linked immunospot (ELISpot) assay

Splenocytes from vaccinated mice were plated at 1 × 10^{6}/well into 96-well HTS IP plates (Millipore) precoated with 5 µg/mL of rat anti-mouse IFN-γ (clone R4-6A2, BD Biosciences). Cells were then stimulated with 15 µg/mL of rat ErbB2 immunodominant peptide (TYVPANASL) peptide for 16 hours in the incubator, or with concanavalin A (2 ug/ml) or medium alone as positive and negative controls, respectively. Images of the wells were acquired, and IFN-γ spots enumerated, with a microplate reader, along with a computer-assisted image analysis system (Immunospot; CTL Europe, Bonn, Germany), as previously described [82].

Quantification and statistical analysis

All graphs show mean ± SEM and were analyzed with GraphPad Prism (version 6.0, GraphPad Software). Detailed statistical tests are reported in figure legends, where n represents the total number of independent experiments. For *in vivo* data, n is referred to the number of mice per group.

Statistical significance was tested with unpaired t-test when two groups of data were compared, with one-way ANOVA followed by Sidak's multiple comparison test when more than two groups were analyzed. Two-way ANOVA followed by Sidak's multiple comparison test was performed when two variables were analyzed. When relevant, one sample t-test was performed. For human biopsies analysis non-parametric Krustal-Wallis test followed by Benjamini, Krieger and Yekutieli multiple comparison test was performed. Significance was defined as *P < 0.05, **P < 0.01, and ***P < 0.001. The illustrations were created on Biorender.com and all figures were assembled using Adobe Illustrator (AI, 2022).

References

1. Fearon, K., Strasser, F., Anker, S.D., Bosaeus, I., Bruera, E., Fainsinger, R.L., Jatoi, A., Loprinzi, C., MacDonald, N., Mantovani, G., et al. (2011). Definition and classification of cancer cachexia: an international consensus. Lancet Oncol *12*, 489-495. 10.1016/S1470-2045(10)70218-7.

2. von Haehling, S., and Anker, S.D. (2010). Cachexia as a major underestimated and unmet medical need: facts and numbers. J Cachexia Sarcopenia Muscle *1*, 1-5. 10.1007/s13539-010-0002-6.

3. Fearon, K.C. (2011). Cancer cachexia and fat-muscle physiology. N Engl J Med *365*, 565-567. 10.1056/NEJMcibr1106880.

4. Rausch, V., Sala, V., Penna, F., Porporato, P.E., and Ghigo, A. (2021). Understanding the common mechanisms of heart and skeletal muscle wasting in cancer cachexia. Oncogenesis *10*, 1. 10.1038/s41389-020-00288-6.

5. Zhou, X., Wang, J.L., Lu, J., Song, Y., Kwak, K.S., Jiao, Q., Rosenfeld, R., Chen, Q., Boone, T., Simonet, W.S., et al. (2010). Reversal of cancer cachexia and muscle wasting by ActRIIB antagonism leads to prolonged survival. Cell *142*, 531-543. 10.1016/j.cell.2010.07.011.

6. Ballaro, R., Beltra, M., De Lucia, S., Pin, F., Ranjbar, K., Hulmi, J.J., Costelli, P., and Penna, F. (2019). Moderate exercise in mice improves cancer plus chemotherapy-induced muscle wasting and mitochondrial alterations. FASEB J *33*, 5482-5494. 10.1096/fj.201801862R.

7. Wyart, E., Hsu, M.Y., Sartori, R., Mina, E., Rausch, V., Pierobon, E.S., Mezzanotte, M., Pezzini, C., Bindels, L.B., Lauria, A., et al. (2022). Iron supplementation is sufficient to rescue skeletal muscle mass and function in cancer cachexia. EMBO Rep, e53746. 10.15252/embr.202153746.

8. Wang, G., Biswas, A.K., Ma, W., Kandpal, M., Coker, C., Grandgenett, P.M., Hollingsworth, M.A., Jain, R., Tanji, K., Lomicronpez-Pintado, S., et al. (2018). Metastatic cancers promote cachexia through ZIP14 upregulation in skeletal muscle. Nat Med *24*, 770-781. 10.1038/s41591-018-0054-2.

9. Brown, J.L., Rosa-Caldwell, M.E., Lee, D.E., Blackwell, T.A., Brown, L.A., Perry, R.A., Haynie, W.S., Hardee, J.P., Carson, J.A., Wiggs, M.P., et al. (2017). Mitochondrial degeneration precedes the development of muscle atrophy in progression of cancer cachexia in tumour-bearing mice. J Cachexia Sarcopenia Muscle *8*, 926-938. 10.1002/jcsm.12232.

10. Wyart, E., Reano, S., Hsu, M.Y., Longo, D.L., Li, M., Hirsch, E., Filigheddu, N., Ghigo, A., Riganti, C., and Porporato, P.E. (2018). Metabolic Alterations in a Slow-Paced Model of Pancreatic Cancer-Induced Wasting. Oxid Med Cell Longev *2018*, 6419805. 10.1155/2018/6419805.

11. Sartori, R., Milan, G., Patron, M., Mammucari, C., Blaauw, B., Abraham, R., and Sandri, M. (2009). Smad2 and 3 transcription factors control muscle mass in adulthood. Am J Physiol Cell Physiol *296*, C1248-1257. 10.1152/ajpcell.00104.2009.

12. Winbanks, C.E., Chen, J.L., Qian, H., Liu, Y., Bernardo, B.C., Beyer, C., Watt, K.I., Thomson, R.E., Connor, T., Turner, B.J., et al. (2013). The bone morphogenetic protein axis is a positive regulator of skeletal muscle mass. J Cell Biol *203*, 345-357. 10.1083/jcb.201211134.

13. Sartori, R., Schirwis, E., Blaauw, B., Bortolanza, S., Zhao, J., Enzo, E., Stantzou, A., Mouisel, E., Toniolo, L., Ferry, A., et al. (2013). BMP signaling controls muscle mass. Nat Genet *45*, 1309-1318. 10.1038/ng.2772.

14. Sartori, R., Hagg, A., Zampieri, S., Armani, A., Winbanks, C.E., Viana, L.R., Haidar, M., Watt, K.I., Qian, H., Pezzini, C., et al. (2021). Perturbed BMP signaling and denervation promote muscle wasting in cancer cachexia. Sci Transl Med *13*. 10.1126/scitranslmed.aay9592.

15. Winbanks, C.E., Murphy, K.T., Bernardo, B.C., Qian, H., Liu, Y., Sepulveda, P.V., Beyer, C., Hagg, A., Thomson, R.E., Chen, J.L., et al. (2016). Smad7 gene delivery prevents muscle wasting associated with cancer cachexia in mice. Sci Transl Med *8*, 348ra398. 10.1126/scitranslmed.aac4976.

16. Sandri, M., Sandri, C., Gilbert, A., Skurk, C., Calabria, E., Picard, A., Walsh, K., Schiaffino, S., Lecker, S.H., and Goldberg, A.L. (2004). Foxo transcription factors induce the atrophy-related ubiquitin ligase atrogin-1 and cause skeletal muscle atrophy. Cell *117*, 399-412. 10.1016/s0092-8674(04)00400-3.

17. Schiaffino, S., Dyar, K.A., Ciciliot, S., Blaauw, B., and Sandri, M. (2013). Mechanisms regulating skeletal muscle growth and atrophy. FEBS J *280*, 4294-4314. 10.1111/febs.12253.

18. Lecker, S.H., Jagoe, R.T., Gilbert, A., Gomes, M., Baracos, V., Bailey, J., Price, S.R., Mitch, W.E., and Goldberg, A.L. (2004). Multiple types of skeletal muscle atrophy involve a common program of changes in gene expression. FASEB J *18*, 39-51. 10.1096/fj.03-0610com.

19. Huang, J., and Zhu, X. (2016). The molecular mechanisms of calpains action on skeletal muscle atrophy. Physiol Res *65*, 547-560. 10.33549/physiolres.933087.

20. Mammucari, C., Milan, G., Romanello, V., Masiero, E., Rudolf, R., Del Piccolo, P., Burden, S.J., Di Lisi, R., Sandri, C., Zhao, J., et al. (2007). FoxO3 controls autophagy in skeletal muscle in vivo. Cell Metab *6*, 458-471. 10.1016/j.cmet.2007.11.001.

21. Loumaye, A., de Barsy, M., Nachit, M., Lause, P., Frateur, L., van Maanen, A., Trefois, P., Gruson, D., and Thissen, J.P. (2015). Role of Activin A and myostatin in human cancer cachexia. J Clin Endocrinol Metab *100*, 2030-2038. 10.1210/jc.2014-4318.

22. Loumaye, A., de Barsy, M., Nachit, M., Lause, P., van Maanen, A., Trefois, P., Gruson, D., and Thissen, J.P. (2017). Circulating Activin A predicts survival in cancer patients. J Cachexia Sarcopenia Muscle *8*, 768-777. 10.1002/jcsm.12209.

23. Chen, J.L., Walton, K.L., Winbanks, C.E., Murphy, K.T., Thomson, R.E., Makanji, Y., Qian, H., Lynch, G.S., Harrison, C.A., and Gregorevic, P. (2014). Elevated expression of activins promotes muscle wasting and cachexia. FASEB J *28*, 1711-1723. 10.1096/fj.13-245894.

24. Lee, S.J., and McPherron, A.C. (1999). Myostatin and the control of skeletal muscle mass. Curr Opin Genet Dev *9*, 604-607. 10.1016/s0959-437x(99)00004-0.

25. Zimmers, T.A., Davies, M.V., Koniaris, L.G., Haynes, P., Esquela, A.F., Tomkinson, K.N., McPherron, A.C., Wolfman, N.M., and Lee, S.J. (2002). Induction of cachexia in mice by systemically administered myostatin. Science *296*, 1486-1488. 10.1126/science.1069525.

26. Ball, R.W., Warren-Paquin, M., Tsurudome, K., Liao, E.H., Elazzouzi, F., Cavanagh, C., An, B.S., Wang, T.T., White, J.H., and Haghighi, A.P. (2010). Retrograde BMP signaling controls synaptic growth at the NMJ by regulating trio expression in motor neurons. Neuron *66*, 536-549. 10.1016/j.neuron.2010.04.011.

27. Lee, S.H., Kim, Y.J., and Choi, S.Y. (2016). BMP signaling modulates the probability of neurotransmitter release and readily releasable pools in Drosophila neuromuscular junction synapses. Biochem Biophys Res Commun *479*, 440-446. 10.1016/j.bbrc.2016.09.072.

28. Kautz, L., Jung, G., Valore, E.V., Rivella, S., Nemeth, E., and Ganz, T. (2014). Identification of erythroferrone as an erythroid regulator of iron metabolism. Nat Genet *46*, 678-684. 10.1038/ng.2996.

29. Arezes, J., Foy, N., McHugh, K., Sawant, A., Quinkert, D., Terraube, V., Brinth, A., Tam, M., LaVallie, E.R., Taylor, S., et al. (2018). Erythroferrone inhibits the induction of hepcidin by BMP6. Blood *132*, 1473-1477. 10.1182/blood-2018-06-857995.

30. Wang, C.Y., Xu, Y., Traeger, L., Dogan, D.Y., Xiao, X., Steinbicker, A.U., and Babitt, J.L. (2020). Erythroferrone lowers hepcidin by sequestering BMP2/6 heterodimer from binding to the BMP type I receptor ALK3. Blood *135*, 453-456. 10.1182/blood.2019002620.

31. Kautz, L., Jung, G., Du, X., Gabayan, V., Chapman, J., Nasoff, M., Nemeth, E., and Ganz, T. (2015). Erythroferrone contributes to hepcidin suppression and iron overload in a mouse model of beta-thalassemia. Blood *126*, 2031-2037. 10.1182/blood-2015-07-658419.

32. Seldin, M.M., Peterson, J.M., Byerly, M.S., Wei, Z., and Wong, G.W. (2012). Myonectin (CTRP15), a novel myokine that links skeletal muscle to systemic lipid homeostasis. J Biol Chem *287*, 11968-11980. 10.1074/jbc.M111.336834.

33. Colucci, S., Pagani, A., Pettinato, M., Artuso, I., Nai, A., Camaschella, C., and Silvestri, L. (2017). The immunophilin FKBP12 inhibits hepcidin expression by binding the BMP type I receptor ALK2 in hepatocytes. Blood *130*, 2111-2120. 10.1182/blood-2017-04-780692.

34. Pettinato, M., Dulja, A., Colucci, S., Furiosi, V., Fette, F., Steinbicker, A.U., Muckenthaler, M.U., Nai, A., Pagani, A., and Silvestri, L. (2023). FKBP12 inhibits hepcidin expression by modulating BMP receptors interaction and ligand responsiveness in hepatocytes. Am J Hematol *98*, 1223-1235. 10.1002/ajh.26961.

35. Song, G.A., Kim, H.J., Woo, K.M., Baek, J.H., Kim, G.S., Choi, J.Y., and Ryoo, H.M. (2010). Molecular consequences of the ACVR1(R206H) mutation of fibrodysplasia ossificans progressiva. J Biol Chem *285*, 22542-22553. 10.1074/jbc.M109.094557.

36. Wang, T., Li, B.Y., Danielson, P.D., Shah, P.C., Rockwell, S., Lechleider, R.J., Martin, J., Manganaro, T., and Donahoe, P.K. (1996). The immunophilin FKBP12 functions as a common inhibitor of the TGF beta family type I receptors. Cell *86*, 435-444. 10.1016/s0092-8674(00)80116-6.

37. Mathelier, A., Fornes, O., Arenillas, D.J., Chen, C.Y., Denay, G., Lee, J., Shi, W., Shyr, C., Tan, G., Worsley-Hunt, R., et al. (2016). JASPAR 2016: a major expansion and update of the open-access database of transcription factor binding profiles. Nucleic Acids Res *44*, D110-115. 10.1093/nar/gkv1176.

38. Bonetto, A., Aydogdu, T., Kunzevitzky, N., Guttridge, D.C., Khuri, S., Koniaris, L.G., and Zimmers, T.A. (2011). STAT3 activation in skeletal muscle links muscle wasting and the acute phase response in cancer cachexia. PLoS One *6*, e22538. 10.1371/journal.pone.0022538.

39. Narsale, A.A., and Carson, J.A. (2014). Role of interleukin-6 in cachexia: therapeutic implications. Curr Opin Support Palliat Care *8*, 321-327. 10.1097/SPC.0000000000000091.

40. Strassmann, G., Fong, M., Kenney, J.S., and Jacob, C.O. (1992). Evidence for the involvement of interleukin 6 in experimental cancer cachexia. J Clin Invest *89*, 1681-1684. 10.1172/JCI115767.

41. Zimmers, T.A., Fishel, M.L., and Bonetto, A. (2016). STAT3 in the systemic inflammation of cancer cachexia. Semin Cell Dev Biol *54*, 28-41. 10.1016/j.semcdb.2016.02.009.

42. Zhang, T., Zhang, Z., Dong, Q., Xiong, J., and Zhu, B. (2020). Histone H3K27 acetylation is dispensable for enhancer activity in mouse embryonic stem cells. Genome Biol *21*, 45. 10.1186/s13059-020-01957-w.

43. Schust, J., Sperl, B., Hollis, A., Mayer, T.U., and Berg, T. (2006). Stattic: a small-molecule inhibitor of STAT3 activation and dimerization. Chem Biol *13*, 1235-1242. 10.1016/j.chembiol.2006.09.018.

44. Arezes, J., Foy, N., McHugh, K., Quinkert, D., Benard, S., Sawant, A., Frost, J.N., Armitage, A.E., Pasricha, S.R., Lim, P.J., et al. (2020). Antibodies against the erythroferrone N-terminal domain prevent hepcidin suppression and ameliorate murine thalassemia. Blood *135*, 547-557. 10.1182/blood.2019003140.

45. Sato, Y., Fu, Y., Liu, H., Lee, M.Y., and Shaw, M.H. (2021). Tumor-immune profiling of CT-26 and Colon 26 syngeneic mouse models reveals mechanism of anti-PD-1 response. BMC Cancer *21*, 1222. 10.1186/s12885-021-08974-3.

46. Hogan, P.G., Chen, L., Nardone, J., and Rao, A. (2003). Transcriptional regulation by calcium, calcineurin, and NFAT. Genes Dev *17*, 2205-2232. 10.1101/gad.1102703.

47. Tampe, B., Tampe, D., Nyamsuren, G., Klopper, F., Rapp, G., Kauffels, A., Lorf, T., Zeisberg, E.M., Muller, G.A., Kalluri, R., et al. (2018). Pharmacological induction of hypoxia-inducible transcription factor ARNT attenuates chronic kidney failure. J Clin Invest *128*, 3053-3070. 10.1172/JCI89632.

48. Ho, S., Clipstone, N., Timmermann, L., Northrop, J., Graef, I., Fiorentino, D., Nourse, J., and Crabtree, G.R. (1996). The mechanism of action of cyclosporin A and FK506. Clin Immunol Immunopathol *80*, S40-45. 10.1006/clin.1996.0140.

49. Spiekerkoetter, E., Tian, X., Cai, J., Hopper, R.K., Sudheendra, D., Li, C.G., El-Bizri, N., Sawada, H., Haghighat, R., Chan, R., et al. (2013). FK506 activates BMPR2, rescues endothelial dysfunction, and reverses pulmonary hypertension. J Clin Invest *123*, 3600-3613. 10.1172/JCI65592.

50. Chaikuad, A., Alfano, I., Kerr, G., Sanvitale, C.E., Boergermann, J.H., Triffitt, J.T., von Delft, F., Knapp, S., Knaus, P., and Bullock, A.N. (2012). Structure of the bone morphogenetic protein receptor ALK2 and implications for fibrodysplasia ossificans progressiva. J Biol Chem *287*, 36990-36998. 10.1074/jbc.M112.365932.

51. Hao, J., Ho, J.N., Lewis, J.A., Karim, K.A., Daniels, R.N., Gentry, P.R., Hopkins, C.R., Lindsley, C.W., and Hong, C.C. (2010). In vivo structure-activity relationship study of dorsomorphin analogues identifies selective VEGF and BMP inhibitors. ACS Chem Biol *5*, 245-253. 10.1021/cb9002865.

52. Peiffer, B.J., Qi, L., Ahmadi, A.R., Wang, Y., Guo, Z., Peng, H., Sun, Z., and Liu, J.O. (2019). Activation of BMP Signaling by FKBP12 Ligands Synergizes with Inhibition of CXCR4 to Accelerate Wound Healing. Cell Chem Biol *26*, 652-661 e654. 10.1016/j.chembiol.2019.01.011.

53. Winbanks, C.E., Weeks, K.L., Thomson, R.E., Sepulveda, P.V., Beyer, C., Qian, H., Chen, J.L., Allen, J.M., Lancaster, G.I., Febbraio, M.A., et al. (2012). Follistatin-mediated skeletal muscle hypertrophy is regulated by Smad3 and mTOR independently of myostatin. J Cell Biol *197*, 997-1008. 10.1083/jcb.201109091.

54. Pedroso, F.E., Spalding, P.B., Cheung, M.C., Yang, R., Gutierrez, J.C., Bonetto, A., Zhan, R., Chan, H.L., Namias, N., Koniaris, L.G., and Zimmers, T.A. (2012). Inflammation, organomegaly, and muscle wasting despite hyperphagia in a mouse model of burn cachexia. J Cachexia Sarcopenia Muscle *3*, 199-211. 10.1007/s13539-012-0062-x.

55. Occhipinti, S., Sponton, L., Rolla, S., Caorsi, C., Novarino, A., Donadio, M., Bustreo, S., Satolli, M.A., Pecchioni, C., Marchini, C., et al. (2014). Chimeric rat/human HER2 efficiently circumvents HER2 tolerance in cancer patients. Clin Cancer Res *20*, 2910-2921. 10.1158/1078-0432.CCR-13-2663.

56. Babic, A., Rosenthal, M.H., Sundaresan, T.K., Khalaf, N., Lee, V., Brais, L.K., Loftus, M., Caplan, L., Denning, S., Gurung, A., et al. (2023). Adipose tissue and skeletal muscle wasting precede clinical diagnosis of pancreatic cancer. Nat Commun *14*, 4317. 10.1038/s41467-023-40024-3.

57. Mayers, J.R., Wu, C., Clish, C.B., Kraft, P., Torrence, M.E., Fiske, B.P., Yuan, C., Bao, Y., Townsend, M.K., Tworoger, S.S., et al. (2014). Elevation of circulating branched-chain amino acids is an early event in human pancreatic adenocarcinoma development. Nat Med *20*, 1193-1198. 10.1038/nm.3686.

58. Argiles, J.M., Busquets, S., and Lopez-Soriano, F.J. (2003). Cytokines in the pathogenesis of cancer cachexia. Curr Opin Clin Nutr Metab Care *6*, 401-406. 10.1097/01.mco.0000078983.18774.cc.

59. Rupert, J.E., Narasimhan, A., Jengelley, D.H.A., Jiang, Y., Liu, J., Au, E., Silverman, L.M., Sandusky, G., Bonetto, A., Cao, S., et al. (2021). Tumor-derived IL-6 and trans-signaling among tumor, fat, and muscle mediate pancreatic cancer cachexia. J Exp Med *218*. 10.1084/jem.20190450.

60. Chen, J.L., Walton, K.L., Qian, H., Colgan, T.D., Hagg, A., Watt, M.J., Harrison, C.A., and Gregorevic, P. (2016). Differential Effects of IL6 and Activin A in the Development of Cancer-Associated Cachexia. Cancer Res *76*, 5372-5382. 10.1158/0008-5472.CAN-15-3152.

61. Mantovani, A., Allavena, P., Sica, A., and Balkwill, F. (2008). Cancer-related inflammation. Nature *454*, 436-444. 10.1038/nature07205.

62. Zhong, W., Wu, K., Long, Z., Zhou, X., Zhong, C., Wang, S., Lai, H., Guo, Y., Lv, D., Lu, J., and Mao, X. (2022). Gut dysbiosis promotes prostate cancer progression and docetaxel resistance via activating NF-kappaB-IL6-STAT3 axis. Microbiome *10*, 94. 10.1186/s40168-022-01289-w.

63. Shi, M., Zong, X., Hur, J., Birmann, B.M., Martinez-Maza, O., Epeldegui, M., Chan, A.T., Giovannucci, E.L., and Cao, Y. (2023). Circulating markers of microbial translocation and host response to bacteria with risk of colorectal cancer: a prospective, nested case-control study in men. EBioMedicine *91*, 104566. 10.1016/j.ebiom.2023.104566.

64. Kwong, T.N.Y., Wang, X., Nakatsu, G., Chow, T.C., Tipoe, T., Dai, R.Z.W., Tsoi, K.K.K., Wong, M.C.S., Tse, G., Chan, M.T.V., et al. (2018). Association Between Bacteremia From Specific Microbes and Subsequent Diagnosis of Colorectal Cancer. Gastroenterology *155*, 383-390 e388. 10.1053/j.gastro.2018.04.028.

65. Jarnicki, A., Putoczki, T., and Ernst, M. (2010). Stat3: linking inflammation to epithelial cancer - more than a "gut" feeling? Cell Div *5*, 14. 10.1186/1747-1028-5-14.

66. Togashi, Y., Kogita, A., Sakamoto, H., Hayashi, H., Terashima, M., de Velasco, M.A., Sakai, K., Fujita, Y., Tomida, S., Kitano, M., et al. (2015). Activin signal promotes cancer progression and is involved in cachexia in a subset of pancreatic cancer. Cancer Lett *356*, 819-827. 10.1016/j.canlet.2014.10.037.

67. Thissen, J.P., and Loumaye, A. (2013). [Role of Activin A and Myostatin in cancer cachexia]. Ann Endocrinol (Paris) *74*, 79-81. 10.1016/j.ando.2013.03.004.

68. Golan, T., Geva, R., Richards, D., Madhusudan, S., Lin, B.K., Wang, H.T., Walgren, R.A., and Stemmer, S.M. (2018). LY2495655, an antimyostatin antibody, in pancreatic cancer: a randomized, phase 2 trial. J Cachexia Sarcopenia Muscle *9*, 871-879. 10.1002/jcsm.12331.

69. Huse, M., Muir, T.W., Xu, L., Chen, Y.G., Kuriyan, J., and Massague, J. (2001). The TGF beta receptor activation process: an inhibitor- to substrate-binding switch. Mol Cell *8*, 671-682. 10.1016/s1097-2765(01)00332-x.

70. Shore, E.M., Xu, M., Feldman, G.J., Fenstermacher, D.A., Cho, T.J., Choi, I.H., Connor, J.M., Delai, P., Glaser, D.L., LeMerrer, M., et al. (2006). A recurrent mutation in the BMP type I receptor ACVR1 causes inherited and sporadic fibrodysplasia ossificans progressiva. Nat Genet *38*, 525-527. 10.1038/ng1783.

71. Dumont, F.J., and Su, Q. (1996). Mechanism of action of the immunosuppressant rapamycin. Life Sci *58*, 373-395. 10.1016/0024-3205(95)02233-3.

72. Cetin, H., Beeson, D., Vincent, A., and Webster, R. (2020). The Structure, Function, and Physiology of the Fetal and Adult Acetylcholine Receptor in Muscle. Front Mol Neurosci *13*, 581097. 10.3389/fnmol.2020.581097.

73. Wyart, E., Bindels, L.B., Mina, E., Menga, A., Stanga, S., and Porporato, P.E. (2020). Cachexia, a Systemic Disease beyond Muscle Atrophy. Int J Mol Sci *21*. 10.3390/ijms21228592.

74. Caan, B.J., Meyerhardt, J.A., Kroenke, C.H., Alexeeff, S., Xiao, J., Weltzien, E., Feliciano, E.C., Castillo, A.L., Quesenberry, C.P., Kwan, M.L., and Prado, C.M. (2017). Explaining the Obesity Paradox: The Association between Body Composition and Colorectal Cancer Survival (C-SCANS Study). Cancer Epidemiol Biomarkers Prev *26*, 1008-1015. 10.1158/1055-9965.EPI-17-0200.

75. Murata, A., Amaya, K., Mochizuki, K., Sotokawa, M., Otaka, S., Tani, K., Nakagaki, S., and Ueda, T. (2018). Superior Mesenteric Artery-Pancreaticoduodenal Arcade Bypass Grafting for Repair of Inferior Pancreaticoduodenal Artery Aneurysm with Celiac Axis Occlusion. Ann Vasc Dis *11*, 153-157. 10.3400/avd.cr.17-00113.

76. Avalle, L., Marino, F., Camporeale, A., Guglielmi, C., Viavattene, D., Bandini, S., Conti, L., Cimino, J., Forni, M., Zanini, C., et al. (2020). Liver-Specific siRNA-Mediated Stat3 or C3 Knockdown Improves the Outcome of Experimental Autoimmune Myocarditis. Mol Ther Methods Clin Dev *18*, 62-72. 10.1016/j.omtm.2020.05.023.

77. Ballaro, R., Lopalco, P., Audrito, V., Beltra, M., Pin, F., Angelini, R., Costelli, P., Corcelli, A., Bonetto, A., Szeto, H.H., et al. (2021). Targeting Mitochondria by SS-31 Ameliorates the Whole Body Energy Status in Cancer- and Chemotherapy-Induced Cachexia. Cancers (Basel) *13*. 10.3390/cancers13040850.

78. Goodman, C.A., Mabrey, D.M., Frey, J.W., Miu, M.H., Schmidt, E.K., Pierre, P., and Hornberger, T.A. (2011). Novel insights into the regulation of skeletal muscle protein synthesis as revealed by a new nonradioactive in vivo technique. FASEB J *25*, 1028-1039. 10.1096/fj.10-168799.

79. Legland, D., Arganda-Carreras, I., and Andrey, P. (2016). MorphoLibJ: integrated library and plugins for mathematical morphology with ImageJ. Bioinformatics *32*, 3532-3534. 10.1093/bioinformatics/btw413.

80. Shang, M., Cappellesso, F., Amorim, R., Serneels, J., Virga, F., Eelen, G., Carobbio, S., Rincon, M.Y., Maechler, P., De Bock, K., et al. (2020). Macrophage-derived glutamine boosts satellite cells and muscle regeneration. Nature *587*, 626-631. 10.1038/s41586-020-2857-9.

81. Conti, L., Bolli, E., Di Lorenzo, A., Franceschi, V., Macchi, F., Riccardo, F., Ruiu, R., Russo, L., Quaglino, E., Donofrio, G., and Cavallo, F. (2020). Immunotargeting of the xCT Cystine/Glutamate Antiporter Potentiates the Efficacy of HER2-Targeted Immunotherapies in Breast Cancer. Cancer Immunol Res *8*, 1039-1053. 10.1158/2326-6066.CIR-20-0082.

82. Quaglino, E., Mastini, C., Amici, A., Marchini, C., Iezzi, M., Lanzardo, S., De Giovanni, C., Montani, M., Lollini, P.L., Masucci, G., et al. (2010). A better immune reaction to Erbb-2 tumors is elicited in mice by DNA vaccines encoding rat/human chimeric proteins. Cancer Res *70*, 2604-2612. 10.1158/0008-5472.CAN-09-2548.

83. Macagno, M., Bandini, S., Bolli, E., Bello, A., Riccardo, F., Barutello, G., Merighi, I.F., Forni, G., Lamolinara, A., Del Pizzo, F., et al. (2022). Role of ADCC, CDC, and CDCC in Vaccine-Mediated Protection against Her2 Mammary Carcinogenesis. Biomedicines *10*. 10.3390/biomedicines10020230.

84. Jacob, J., Radkevich, O., Forni, G., Zielinski, J., Shim, D., Jones, R.F., and Wei, W.Z. (2006). Activity of DNA vaccines encoding self or heterologous Her-2/neu in Her-2 or neu transgenic mice. Cell Immunol *240*, 96-106. 10.1016/j.cellimm.2006.07.002.

General conclusion

Skeletal muscle atrophy is a prevalent and impactful condition affecting elderly people and patients with various diseases. In patients with chronic diseases the prevalence of muscle atrophy is even more pronounced than in aged individuals, reaching 20-50% in case of chronic heart failure (CHF), chronic obstructive pulmonary disease (COPD) and chronic kidney disease (CKD). In oncologic patients it further extends, where 30-80% of cancer patients suffer from muscle atrophy and cachexia, depending on the cancer type and stage.

Skeletal muscle atrophy significantly impairs patients' quality of life, their overall health and their response to therapies, as muscle mass and function are essential for vital activities. Despite its prevalence and clinical implications, effective treatments for muscle atrophy remain elusive, largely due to the incomplete understanding of its molecular mechanisms.

In the present work, we explored three different aspects of skeletal muscle atrophy. The first part, performed during SARS-CoV-2 pandemic, investigated the effects of severe inflammatory diseases like COVID-19, sepsis, and pneumonia on skeletal muscle health. With the rapid saturation of Intensive Care Units (ICUs) and the use of invasive mechanical ventilation (IMV), our study aimed to determine whether these patients were more susceptible to skeletal muscle atrophy compared to ICU patients without systemic inflammation. We conducted *in vitro* experiments to assess the impact of inflammatory mediators present in patients' plasma on muscle atrophy and mitochondrial dysfunction, and we found that extracellular vesicles (EVs) derived from adipose-derived stromal stem cells (ASC) had a potent antioxidant effect with therapeutic potential.

The common thread that links the first and the second part is mitochondrial dysfunction, a feature caused by systemic inflammation in the skeletal muscle. In a context of cancer cachexia, this chapter explored the alterations in systemic iron metabolism commonly seen in cancer patients, given iron's crucial role in mitochondrial function and energy production. Our research aimed to elucidate whether these iron alterations directly contribute to muscle atrophy and whether iron supplementation could mitigate muscle wasting and loss of muscle force in

anemic cancer patients.

The iron is then the linking element with the third part of this work, that focuses on erythroferrone (ERFE), an iron-related gene significantly upregulated in cancer cachexia, that we found to be involved in skeletal muscle mass regulation. We examined its mechanism, particularly its inhibition of BMP-Smad1/5/8 signaling and investigated the use of FK506 (tacrolimus) as a pharmacological intervention to counteract ERFE effects and prevent muscle atrophy. Additionally, we characterized FKBP12, the target of FK506, demonstrating its novel involvement in skeletal muscle mass regulation, and contributing to expand the knowledge on the interactors of cancer cachexia.

Overall, our findings unveiled novel interactors involved in the development and progression of skeletal muscle atrophy in contexts of systemic inflammation, offering valuable insights and potential therapeutic strategies. Despite the progress made, significant gaps remain, necessitating further research to uncover other potential mechanisms behind this complex disease.

Acknowledgment

These acknowledgments mark the close of a significant chapter in my life, extending beyond the four years of my Ph.D. journey.

I am grateful to the professors who enabled me to begin and complete the Ph.D. Program in Biomedical Sciences and Oncology: Prof. Emilio Hirsch, Prof. Andrea Graziani, Prof. Chiara Ambrogio, Prof. Alessandro Bertero and Prof. Isaia Barbieri.
To my supervisor, Prof. Paolo Porporato, I extend my sincere thanks for fostering my scientific creativity, encouraging my critical thinking, and providing me with unique career growth opportunities.

I would like to express special gratitude to my close colleagues and friends, Elisabeth and Myriam, who made my years in the lab filled with true friendship, trust, and sincerity. To Myriam, who embodies scientific rigor, thank you for sharing your passions for cooking and soap-making, and for unforgettable memories in Kyoto. Your commitment to keeping in touch across the globe has been significant. Elisabeth, I am grateful for the deep friendship we built together, made of mutual trust, emotional safety, and unwavering support. I will always treasure our memories of visiting the countryside of Toulouse, hiking and cycling in the mountains, swimming after-lab on summer afternoons, that now became our late-night pizzas.
I am also thankful to all the members of the lab who, through their expertise and companionship, helped me grow both scientifically and personally, creating valuable memories that I will carry with me. I thank especially Giovanna, Valentina, Ivan, Francesca, Elia, Sophie, Camilla, Rita, Roberta, Alessio, Alfonso, Giada, and Chiara.
To my friends beyond the lab, thank you for countless unforgettable memories that enriched my life outside of work and for experiences that have undoubtedly shaped my personal growth and soft skills. I thank Dario, Matteo, Carlotta, Pietro, and my friends of the climbing and swinging groups.
My deepest gratitude goes to my family for their unconditional support, trust in my decisions, and unfailing support whenever I needed them.

Lastly, to Max—thank you for teaching me the importance of a healthy work-life balance, for your constant love, emotional and practical support, and for building with me foundational experiences that continue to shape who I am.

ALLEGATO B

AREA 05 - SCIENZE BIOLOGICHE TABELLA DI CORRISPONDENZA					
Cod. GSD	Denominazione GSD	Cod. SSD	Denominazione SSD	CORRISPONDENZA: Settore Concorsuale *ex* D.M. 855/2015	CORRISPONDENZA: Settore scientifico-disciplinare
05/BIOS-01	BOTANICA	BIOS-01/A	Botanica generale	05/A1 – BOTANICA	BIO/01-BOTANICA GENERALE
		BIOS-01/B	Botanica sistematica		BIO/02 - BOTANICA SISTEMATICA
		BIOS-01/C	Botanica ambientale e applicata		BIO/03 - BOTANICA AMBIENTALE E APPLICATA
		BIOS-01/D	Biologia farmaceutica		BIO/15 - BIOLOGIA FARMACEUTICA
05/BIOS-02	FISIOLOGIA VEGETALE	BIOS-02/A	Fisiologia vegetale	05/A2 – FISIOLOGIA VEGETALE	BIO/04 - FISIOLOGIA VEGETALE
05/BIOS-03	ZOOLOGIA E ANTROPOLOGIA	BIOS-03/A	Zoologia	05/B1 - ZOOLOGIA E ANTROPOLOGIA	BIO/05 - ZOOLOGIA
		BIOS-03/B	Antropologia		BIO/08 - ANTROPOLOGIA
05/BIOS-04	ANATOMIA, BIOLOGIA CELLULARE E BIOLOGIA DELLO SVILUPPO COMPARATE	BIOS-04/A	Anatomia, biologia cellulare e biologia dello sviluppo comparate	05/B2 - ANATOMIA COMPARATA E CITOLOGIA	BIO/06 - ANATOMIA COMPARATA E CITOLOGIA
05/BIOS-05	ECOLOGIA	BIOS-05/A	Ecologia	05/C1 - ECOLOGIA	BIO/07 - ECOLOGIA
05/BIOS-06	FISIOLOGIA	BIOS-06/A	Fisiologia	05/D1 – FISIOLOGIA	BIO/09 – FISIOLOGIA
05/BIOS-07	BIOCHIMICA	BIOS-07/A	Biochimica	05/E1- BIOCHIMICA GENERALE	BIO/10 – BIOCHIMICA
05/BIOS-08	BIOLOGIA MOLECOLARE	BIOS-08/A	Biologia molecolare	05/E2 - BIOLOGIA MOLECOLARE	BIO/11 - BIOLOGIA MOLECOLARE
05/BIOS-09	BIOCHIMICA CLINICA E BIOLOGIA MOLECOLARE CLINICA	BIOS-09/A	Biochimica clinica e biologia molecolare clinica	05/E3 BIOCHIMICA CLINICA E BIOLOGIA MOLECOLARE CLINICA	BIO/12 - BIOCHIMICA CLINICA E BIOLOGIA MOLECOLARE CLINICA
05/BIOS-10	BIOLOGIA CELLULARE E APPLICATA	BIOS-10/A	Biologia cellulare e applicata	05/F1- BIOLOGIA APPLICATA	BIO/13 - BIOLOGIA APPLICATA
05/BIOS-11	FARMACOLOGIA	BIOS-11/A	Farmacologia	05/G1 – FARMACOLOGIA, FARMACOLOGIA CLINICA E FARMACOGNOSIA	BIO/14 – FARMACOLOGIA
05/BIOS-12	ANATOMIA UMANA	BIOS-12/A	Anatomia umana	05/H1 – ANATOMIA UMANA	BIO/16 – ANATOMIA UMANA
05/BIOS-13	ISTOLOGIA ED EMBRIOLOGIA UMANA	BIOS-13/A	Istologia ed embriologia umana	05/H2 – ISTOLOGIA	BIO/17 – ISTOLOGIA
05/BIOS-14	GENETICA	BIOS-14/A	Genetica	05/I1- GENETICA	BIO/18 – GENETICA
05/BIOS-15	MICROBIOLOGIA	BIOS-15/A	Microbiologia	05/I2 – MICROBIOLOGIA	BIO/19 – MICROBIOLOGIA